# Radio Spectral Studies of Sunyaev-Zel'dovich-Detected Galaxy Clusters

by

**Mikaela Webber**

Thesis submitted in fulfilment
of the requirements for the degree of
Master of Science
at Rhodes University

Department of Physics and Electronics

**Supervisors:** Dr. K. Knowles, Prof. O.M. Smirnov

Makhanda, South Africa
May 8, 2025

# Declaration of Authorship

I, Mikaela Webber, declare that the content of this thesis, *Radio Spectral Studies of Sunyaev-Zel'dovich-Detected Galaxy Clusters*, in its entirety is my own work and that it has not been submitted, in whole or in part, for any degree at any other University. I have indicated by reference and acknowledgment the areas that are not my own work.

Signed:

_____

Date:

_____

# Abstract

Galaxy clusters are the largest gravitationally bound structures in the universe, thought to form through hierarchical mergers and the accretion of smaller systems. When these massive entities collide, immense amounts of energy are released that heat the intra-cluster medium (ICM) and generate turbulence. This turbulence leads to non-thermal synchrotron radiation from hot ICM regions. Giant radio halos, found near cluster centers, arise from synchrotron radiation by re-accelerated electrons in the cluster's magnetic field due to merger-driven turbulence. On the other hand, radio relics, typically located in cluster outskirts, trace merger shock waves. These emissions are crucial indicators of cluster mergers, offering valuable insights into their dynamic processes.

In this thesis, the radio environments of three Sunyaev-Zel'dovich detected galaxy clusters (ACT-CL J0034+0225, ACT-CL J0137-0827, and ACT-CL J0330-5228) from the MeerKAT Exploration of Relics, Giant Halos, and Extragalactic Radio Sources survey were investigated, with particular focus on diffuse radio emission. We utilised data from the MeerKAT (1.2 GHz and 0.8 GHz) and JVLA (1.5 GHz) telescopes, calibrated using the CARACal and VLA Calibration and Imaging pipelines, respectively. The final self calibrated images have noise values ranging from $8-24$ μJy/beam for the MeerKAT data and $10-30$ μJy/beam for the JVLA.

Four methods of compact source subtraction were tested on the calibrated MeerKAT images, revealing that image-plane subtraction methods yield satisfactory results when compared to visibility-plane subtraction procedures. From the source subtracted images, we measured integrated flux densities for the halos in ACT-CL J0034+0225 and ACT-CL J0137-0827 to be $2.38 \pm 0.63$ mJ/beam and $0.85 \pm 0.70$ mJy/beam, respectively. The

integrated spectral indices of these halos were measured using complementary GMRT images and were found to be $\alpha^{1.16\,\mathrm{GHz}}_{0.32\,\mathrm{GHz}} = -1.34 \pm 0.14$ and $\alpha^{1.16\,\mathrm{GHz}}_{0.32\,\mathrm{GHz}} = -1.33 \pm 0.10$ respectively which are in line with those reported in the literature. The emission in ACT-CL J0330-5228 was found to have an integrated flux density of $3.31 \pm 1.14$ mJy/beam. The emission in ACT-CL J0330-5228 was proposed to be as a result of multiple sources, not solely a radio halo. Archival optical and X-ray data were used to investigate the dynamic state of the clusters and search for cluster members, revealing ongoing activity indicative of merger events in recent or early stages.

Additionally, we investigated serendipitous diffuse radio emission in the ACT-CL J0330-5228 field using archival multiwavelength data along with newly observed MeerKAT data. The integrated spectral indices of the emission were measured as $\alpha^{944\,\mathrm{MHz}}_{802\,\mathrm{MHz}} = -1.4 \pm 0.2$ for the eastern emission and $\alpha^{944\,\mathrm{MHz}}_{802\,\mathrm{MHz}} = -1.1 \pm 0.1$ for the western emission. The wideband spectral index maps indicate a spectral gradient in the eastern structure, typical of a cluster radio relic, while results for the western structure were more in line with (re-accelerated) active galactic nuclei (AGN) driven emission. We identified potential optical sources of the emission and proposed that the western emission arises from the interaction between a nearby disturbed cluster and AGN emission. The eastern structure lacks an optical counterpart at its peak and was propsed to be a radio relic viewed along its length or AGN emission shaped by turbulent interactions with a nearby cluster.

# Acknowledgements

This work is undertaken at Rhodes University, with financial support from the National Research Foundation (NRF) and /or the South African Radio Astronomy Observatory (SARAO). I acknowledge that opinions, findings and conclusions or recommendations expressed here are those of mine alone and that none of the above mentioned sponsors accept liability whatsoever in this regard.

In this thesis we make use of data from the MeerKAT and Karl G. Jansky Very Large Array (JVLA). The MeerKAT telescope is operated by the South African Radio Astronomy Observatory, which is a facility of the National Research Foundation, an agency of the Department of Science and Innovation. The JVLA is an instrument run by the National Radio Astronomy Observatory. The National Radio Astronomy Observatory is a facility of the National Science Foundation operated under cooperative agreement by Associated Universities, Inc.

I would like to thank the Evolutionary Map of the Universe collaboration for sharing images of the structures investigated in Chapter 4. I would also like to thank the students, supervisors and postdocs of RATT who provided the ideal environment for learning, collaboration and research.

# Contents

# List of Figures

# List of Tables

# Abbreviations

The list of acronyms used in this thesis is given below.

| | |
|---|---|
| **1GC** | First Generation Calibration |
| **2GC** | Second Generation Calibration |
| **3GC** | Third Generation Calibration |
| **ACT** | Atacama Cosmology Telescope |
| **AGN** | Active Galactic Nuclei |
| **ASKAP** | Australian SKA Pathfinder |
| **BP** | Bandpass |
| **CASA** | Common Astronomy Software Applications |
| **CLASH** | Cluster Lensing And Supernova survey with Hubble |
| **CMB** | Cosmic Microwave Background |
| **DECaLS** | Dark Energy Camera Legacy Survey |
| **DES** | Dark Energy Survey |
| **EMU** | Evolutionary Map of the Universe |
| **FR I** | Fanaroff-Riley Type I |
| **FR II** | Fanaroff-Riley Type II |
| **FR** | Full Resolution |
| **GMRT** | Giant Metrewave Radio Telescope |
| **GUI** | Graphical User Interface |
| **HR** | High Resolution |
| **ICM** | Intracluster Medium |
| **JVLA** | Karl G. Jansky Very Large Array |

| | |
|---|---|
| **KE** | Kinetic Energy |
| **ΛCDM** | Lambda Cold Dark Matter |
| **LAS** | Largest Angular Size |
| **LLS** | Largest Linear Size |
| **LR** | Low Resolution |
| **MERGHERS** | MeerKAT Exploration of Relics, Giant Halos, and Extragalactic Radio Sources |
| **MGCLS** | MeerKAT Galaxy Cluster Legacy Survey |
| **MS** | Measurement Set |
| **NRAO** | National Radio Astronomy Observatory |
| **Pan-STARRS** | Panoramic Survey Telescope and Rapid Response System |
| **PSF** | Point Spread Function |
| **RFI** | Radio Frequency Interference |
| **RIME** | Radio Interferometer Measurement Equation |
| **RMS** | Root Mean Square |
| **SDSS** | Sloan Digital Sky Survey |
| **SKA** | Square Kilometer Array |
| **SNR** | Signal to Noise Ratio |
| **SZ** | Sunyaev-Zel'dovich |
| **2MASS** | Two Micron All Sky Survey |
| **VLA** | Very Large Array |

# Chapter 1

# Introduction

Galaxy clusters are massive groups of gravitationally bound galaxies. Clusters can contain up to several thousands of galaxies and have masses up to the order of $10^{15}$ $M_{\odot}$. A large portion of this mass is dark matter ($\sim$80%), a small portion is star matter ($\sim 3-5\%$), and the remainder is the intra-cluster medium (ICM; $\sim 15-17\%$) (Blumenthal *et al.*, 1984, Clarke *et al.*, 2014). The ICM is a dilute, magnetised plasma found between the galaxies in a cluster and is held together by the clusters' gravitational pull (Clarke *et al.*, 2014). The bulk of a cluster's baryonic matter is found in the ICM, studies of the which can be used to probe various properties of a cluster (Kravtsov and Borgani, 2012).

## 1.1 Galaxy cluster formation and evolution

Galaxy clusters are thought to form by a hierarchical sequence of merger events and by the accretion of nearby smaller systems. Galaxy clusters are part of an even larger, unbound structure known as the cosmic web. Clusters are found at the nodes of this web and are connected by filaments composed of galaxies. During a merger, two or more (sub-)clusters or groups coalesce forming a larger structure (Kravtsov and Borgani, 2012). As the majority of a cluster's mass budget is taken up by the dark matter component, merger activity is driven by the dark matter hosted within the clusters. Most cluster

formation models are approximated as dark matter-driven dissipation-less collapse from cosmological initial conditions (Kravtsov and Borgani, 2012).

The most widely used model for hierarchical structure formation is the Lambda Cold Dark Matter Model (ΛCDM; Blumenthal *et al.*, 1984). This model is an extension of the Cold Dark Matter (CDM) model which assumes that the Universe is composed primarily of cold dark matter and baryonic matter (Bond *et al.*, 1982). The ΛCDM model includes the cosmological constant, Λ, which accounts for dark energy. The model proposes that large structures, such as clusters, form from smaller structures as a result of the gravitational collapse of peaks in the density field described by the overdensity field:

$$\delta(\mathbf{x}) = \frac{\rho(\mathbf{x}) - \bar{\rho_m}}{\bar{\rho_m}} \tag{1.1}$$

where $\delta(\mathbf{x})$ represents the deviations from the mean density at each point, $\mathbf{x}$, and $\bar{\rho_m}$ is the mean mass density of the Universe (Kravtsov and Borgani, 2012). A common assumption made by most models is that $\delta(\mathbf{x})$ is a homogeneous and isotropic Gaussian random field, which means that $\delta(\mathbf{x})$ has the same statistical properties everywhere in the Universe. The model also assumes that the theory of general relativity is the correct theory of gravity on cosmological scales (Kravtsov and Borgani, 2012).

The ΛCDM model successfully predicts the formation of cosmic structures, the expansion of the Universe, the existence and structure of the cosmic microwave background (CMB), and the observed abundances of hydrogen, helium, and lithium in the Universe (Persic and Salucci, 1992, Ferramacho *et al.*, 2009, Kravtsov and Borgani, 2012). However, despite accurately predicting certain cosmological phenomena, the model is not complete in that it does not accurately predict small scale phenomena. For example, there is an under abundance of dwarf galaxies predicted compared to observational data (Turner, 2022).

Using large statistical selections of galaxy clusters with varied masses and at various redshifts, we can improve current large-scale structure formation models. Merging clusters in particular are good candidates to observe phenomena related to large-scale structure formation and the aftermath thereof. This makes merging and relaxed clusters critical

objects of study, as they represent contrasting stages of cluster evolution and provide complementary insights into the physical processes shaping large-scale structures.

### 1.1.1 Merging clusters

Clusters undergoing merger activity are highly dynamic or disturbed. During merger events, massive amounts of energy are released and shocks are driven into the ICM, heating it up and causing turbulence (Sarazin, 2002). These hot regions of the ICM emit electromagnetic radiation which can be used to study the geometry and kinematics of the merger. The shocks are believed to accelerate or re-accelerate relativistic electrons (cosmic rays) and ions, causing them to emit synchrotron radiation and enabling astronomers to detect and study the disturbances (Blandford and Eichler, 1987, Sarazin, 2002).

The diagram in Figure 1.1 shows the three main stages of a merger event. Initially, the clusters are attracted by their mutual gravitational pull. As the clusters make contact, shock waves are driven into the surroundings and the clusters become one over millions of years. The constituent galaxies of each cluster mix together and and the new cluster begins to cool as the turbulence dissipates. Cluster mergers occur over hundreds of millions of years, and due to the size and immense amounts of energy released during the event, the cooling stage of the merger can take millions of years (Kravtsov and Borgani, 2012).

Merging clusters often exhibit asymmetrical shapes due to the coalescence of two or more substructures. Many observational identifiers at various wavelengths can be used to classify whether a cluster is undergoing or has undergone a merger. Common methods include X-ray morphological analyses (e.g. Cassano *et al.*, 2010), optical analyses (e.g. the Asymmetry parameter; Conselice *et al.*, 2000, Pillay *et al.*, 2021) and offsets between different features of the cluster (e.g. the Centre Shift parameter; Pandge *et al.*, 2018, Pillay *et al.*, 2021). The Centre Shift parameter makes use of an optical density map as well as millimetre data (Sunyaev-Zel'dovich (SZ; Sunyaev and Zeldovich, 1972) detections) to determine the offset between the peak in the SZ detection and the optical density peak in the cluster. A large offset would indicate that the cluster environment is still highly

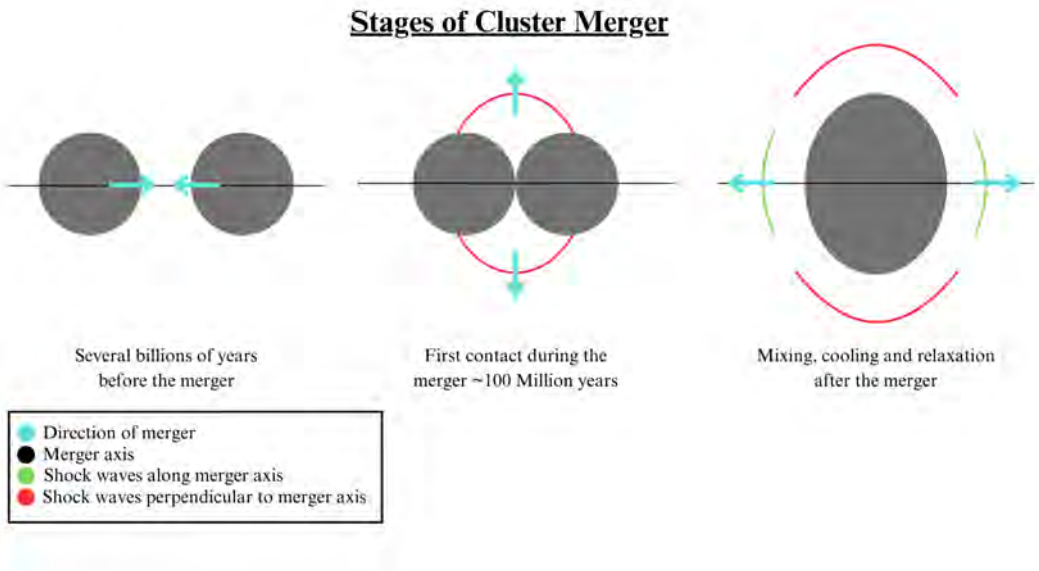


**Figure 1.1:** Main stages during a cluster merger.

disturbed and likely a recent merger. A smaller offset would be indicative of a merger event in its early or very late stages (Pandge *et al.*, 2018).

### 1.1.2 Cool-core clusters

In early observations of galaxy clusters, it was evident that the mass within clusters was insufficient to bind them together (McNamara and Nulsen, 2012). The velocities of the constituent galaxies were large enough that the clusters should have broken apart in less than the Hubble time. The Hubble time is the period required for the Universe to expand to its present size. It is defined as the reciprocal of the Hubble constant, $1/H_0$. For a Hubble constant of 71 km/s/Mpc, the Hubble time is approximately 14 billion years (Freedman and Madore, 2010).

Early X-ray observations found that the cooling time of the gas of the ICM in the centres of many clusters was much shorter than the Hubble time (Fabian and Nulsen, 1977, Mathews and Bregman, 1978). This led to the development of the cooling flow model to explain the additional mass in the clusters and the mechanism by which the gas is compressed. The ICM at the centres of clusters with dense cores is hydrostatically cooled so that the cool gas is compressed by the weight of the overlying gas. Hot gas from the

outer regions of the ICM flows in to replace the compressed gas, generating a cooling flow (Peterson *et al.*, 2003, McNamara and Nulsen, 2012). The mass distributions of these clusters is typically symmetric, often appearing relaxed and undisturbed. Due to the lack of large-scale turbulence, these clusters are unlikely to host certain diffuse cluster emission discussed in Section 1.2. A comparison of a merging and relaxed cluster can be seen in Figure 1.2. The central radio emission (seen in red) in the disturbed cluster, Abell 2744, is much larger and less symmetric than the emission seen at the centre of the relaxed Perseus cluster.

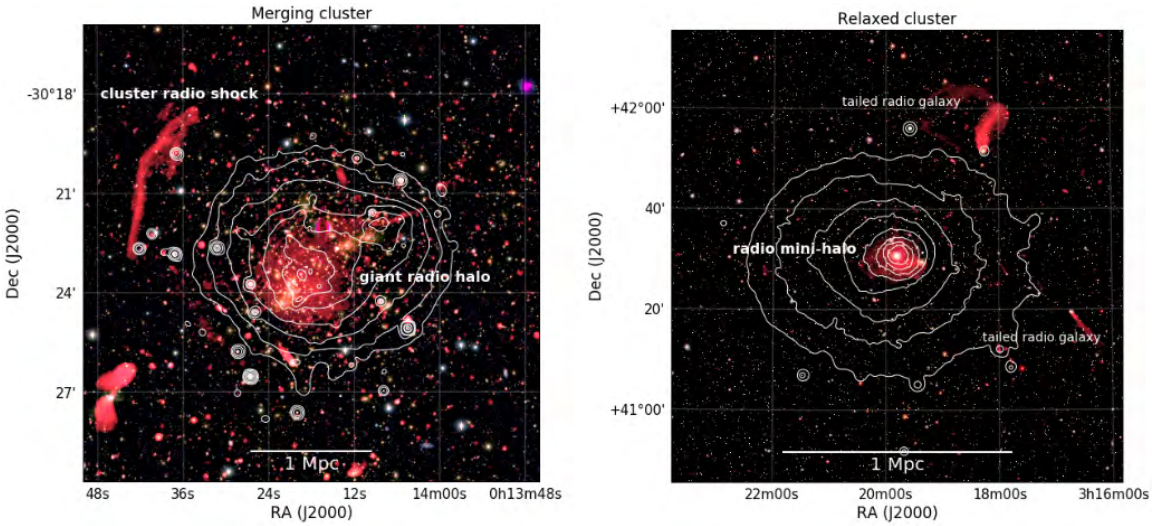


**Figure 1.2:** *Left:* Radio image of the merging cluster Abell 2744. The cluster hosts a giant radio halo and radio shock (both seen in red; Pearce *et al.*, 2017). *Right:* Radio image of the relaxed, cool-core Perseus cluster (Gendron-Marsolais *et al.*, 2017). XMM-Newton X-ray contours in the 0.4–1.3 keV band are overlaid in white on both images. Source: van Weeren *et al.*, 2019.

## 1.2 Diffuse cluster radio emission

All charged particles emit electromagnetic radiation over a wide range of frequencies when accelerated by electromagnetic forces. When particles are accelerated by a magnetic field the radiation is called magneto-bremsstrahlung or synchrotron radiation (Condon and Ransom, 2016). Lighter particles such as electrons and positrons are accelerated more than heavier particles, such as protons and ions. Ultra-relativistic particles have kinetic energy (KE) much greater than their rest mass (KE $\gg mc^2$) and emit non-thermal radiation

that is detectable in the radio regime (Rybicki and Lightman, 1991). These emissions are a hallmark of synchrotron radiation and are strongly dependent on the properties of the magnetic field, such as its strength and orientation. The magnetic fields of a cluster or those of the ICM and interactions between them can be probed through observations of diffuse radio emission (Wiedemann, 2003).

Diffuse cluster radio emission from synchrotron sources can be broadly classified into four categories: radio halos, radio mini-halos, radio relics or shocks, and revived active galactic nuclei (AGN) fossil plasma sources and phoenices (Feretti, 2000, Ferrari *et al.*, 2008, van Weeren *et al.*, 2019). Observational and theoretical evidence suggest that diffuse radio emissions, that are associated with the ICM, such as radio halos and relics, are produced during mergers of two or more galaxy clusters (Cassano *et al.*, 2010, Cuciti *et al.*, 2015). In contrast, revived AGN fossil plasma sources and phoenices originate from AGN activity but can evolve through merger-driven motions (Ferrari *et al.*, 2008).

### 1.2.1 Radio halos

Radio halos are diffuse, extended sources typically found near the centre of massive dynamically disturbed (merging) systems (Cassano *et al.*, 2010, van Weeren *et al.*, 2019). Their sizes range from ∼500 kpc to 2 Mpc (Lindner *et al.*, 2014, Xie *et al.*, 2020). Halos were once believed to have smooth brightness distributions but have recently been found to display discontinuities indicating substructure that is shaped by dynamical motions in the ICM (Botteon *et al.*, 2023). Halos are closely related to cluster merger events. Merging clusters tend to host radio halos due to the merger activity accelerating particles and generating turbulence that re-energises cosmic-ray electrons (Buote, 2001, Cuciti *et al.*, 2015, Cuciti *et al.*, 2021).

#### 1.2.1.1 Origin

In order to sustain their emission over extended periods, the electrons responsible for a radio halo's emission must undergo a continuous process of re-energisation. These emitting electrons typically have short lifespans due to radiative energy losses, far shorter than the

diffusion time required to traverse Mpc-scale regions where emission is observed. This necessitates ongoing re-acceleration within the halo region. Without such re-acceleration, the radio halo's emission would rapidly decline (Cassano and Brunetti, 2005).

Historically, two main models describing the origin of radio halos have been debated, the hadronic model (Enßlin *et al.*, 2011) and the turbulent re-acceleration model (Brunetti *et al.*, 2001). The hadronic model makes use of the hadronic interactions between cosmic ray protons and ICM protons to explain the origin of radio emitting electrons. In the re-acceleration model, a population of seed electrons is thought to be re-accelerated during powerful, merger-induced ICM turbulence (Cassano *et al.*, 2009, Enßlin *et al.*, 2011). Hybrid models, which combine aspects of both hadronic and re-acceleration processes, have also been proposed to address observational challenges faced by the individual models (Zandanel *et al.*, 2013, Keshet, 2023).

Arguments against the hadronic model were indirectly drawn from the integrated radio spectra and spatial characteristics of halos as well as from radio-X-ray scaling relations (Brunetti *et al.*, 2008). Direct arguments against the hadronic model arose from gamma-ray observations of the Coma cluster, revealing that radio halos cannot be of hadronic origin (Reimer and Sreekumar, 2004, Ackermann *et al.*, 2016, Adam *et al.*, 2021).

The turbulent re-acceleration model is thought to be the primary mechanism responsible for generating radio halos, however, the source of the seed electrons is currently debated. Several mechanisms have been proposed, with the possibility that seed electrons are secondary electrons from proton-proton interactions (Brunetti and Blasi, 2005, Brunetti and Lazarian, 2011), previously accelerated particles from merger events or particles resulting from galaxy outflows and AGN activity (de Gasperin *et al.*, 2017, Shimwell *et al.*, 2016).

#### 1.2.1.2 Morphology

Prominent examples of radio halos include the Coma cluster and the Bullet cluster (see Figure 1.3). Each of these clusters host a giant radio halo, a sub-category of radio halos that have Mpc-scale sizes (∼1 to 2 Mpc; Brown and Rudnick, 2011, Shimwell *et al.*, 2015, Andrade-Santos *et al.*, 2017, Sikhosana *et al.*, 2022). The spectral index of a radio halo

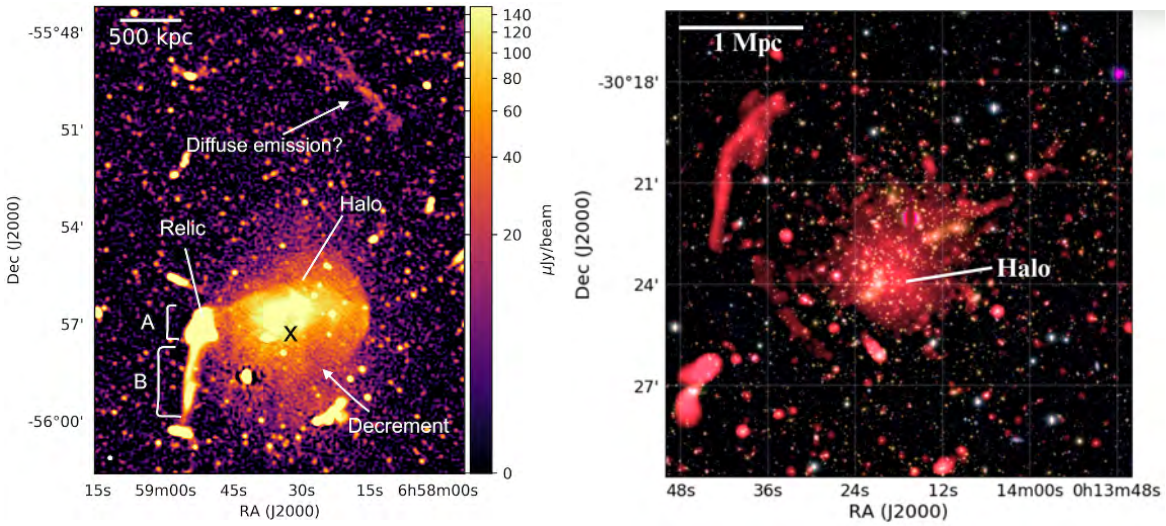


**Figure 1.3:** *Left:* Full resolution MeerKAT 1.3 GHz radio image of the Bullet cluster (Sikhosana *et al.*, 2022). *Right:* Composite image of the Coma cluster (radio emission shown in red; Brown and Rudnick, 2011).

quantifies how its radio emission intensity varies with frequency. In the case of synchrotron emission, the flux density of the emission is related to the frequency by a power law,

$$S_\nu = \nu^\alpha \tag{1.2}$$

where $\nu$ is the frequency and $\alpha$ is the spectral index (Condon and Ransom, 2016). The integrated spectral index of a source can be calculated using Equation 1.3:

$$\alpha = \frac{\log(S_{\nu 2}/S_{\nu 1})}{\log(\nu_2/\nu_1)} \tag{1.3}$$

where the subscripts 1 and 2 are two different frequencies.

Some of the earliest studies to perform spectral index calculations of a radio halo were performed on the Coma cluster aiming to understand the physical processes responsible for the emission and to uncover the underlying mechanisms powering the extended source (Jaffe and Rudnick, 1979, Henning, 1989, Giovannini *et al.*, 1991, 1993). Since then, the spectral index has become a valuable parameter for classifying diffuse radio sources.

Radio halos have integrated spectral indices ranging from $-1.0$ to $-1.4$ (van Weeren *et al.*, 2019). The spectral profile of a typical radio halo steepens toward the outskirts of the halo

due to the combined effects of declining turbulence, weaker magnetic fields, and energy losses of relativistic electrons (Bonafede *et al.*, 2022). There are cases where large scale fluctuations in the spectral index distribution have been observed (Rajpurohit *et al.*, 2021). This behaviour is expected for the turbulent re-acceleration model and provides insight into the balance of acceleration processes as well as synchrotron and inverse Compton losses occurring radially from the cluster centre (Rajpurohit *et al.*, 2021). A popular

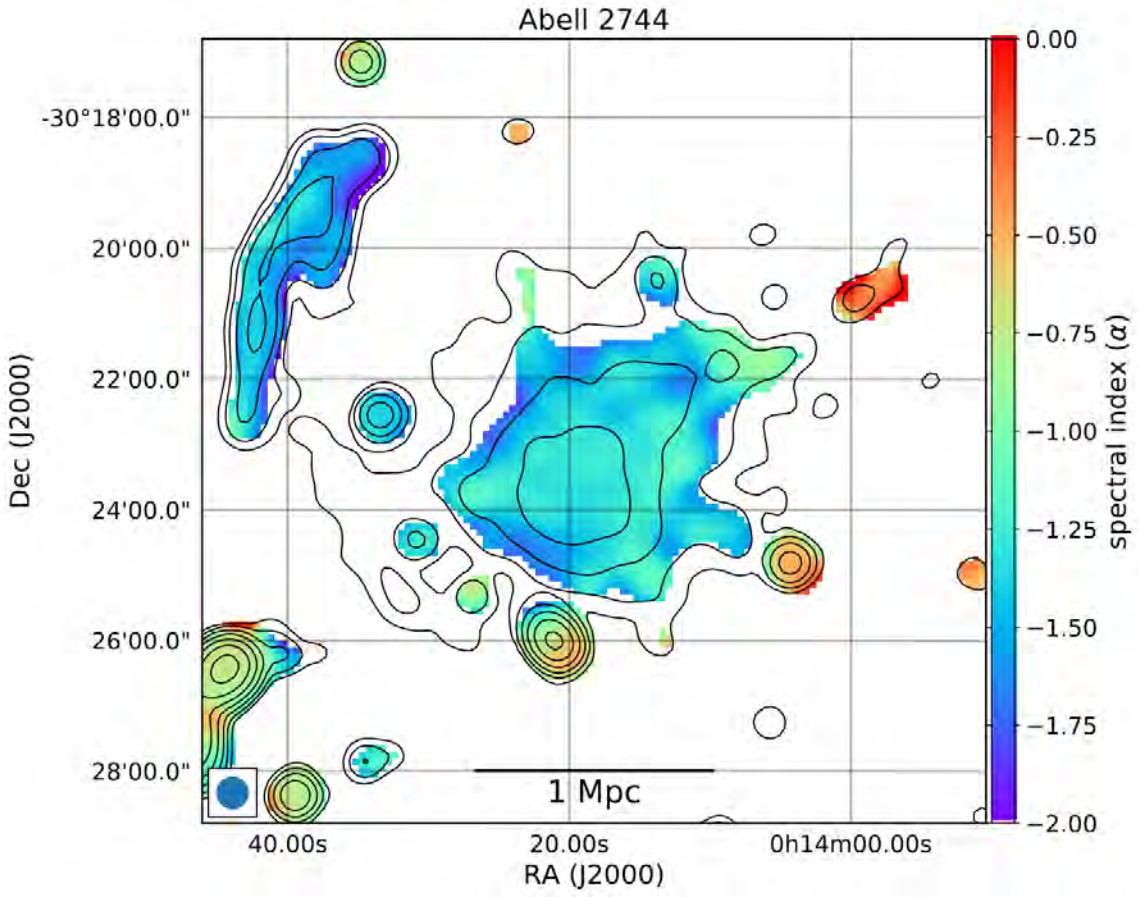


**Figure 1.4:** Spectral index map of the radio halo in Abell 2744 between 1.5 and 3.0 GHz. Source: van Weeren *et al.*, 2019.

method used to study the spectral index variation of a source is to create a spectral index map by calculating the spectral index on a pixel-by-pixel basis between two or more radio images at different frequencies. These maps can be used to probe the 2D spatial spectral structure of a radio source; making it easier to spot trends related to the spectral index (Rajpurohit *et al.*, 2021). An example of such a map can be seen in Figure 1.4.

Halos with spectral indices steeper than $\sim -1.6$ have been observed and are classified as

ultra-steep spectrum radio halos (e.g. Rajpurohit *et al.*, 2022a, Santra *et al.*, 2024). Ultra-steep spectra are expected when the spectral index is measured close to the frequency at which the radio emission becomes significantly weaker (cut-off frequency). Radio halos can appear ultra-steep when observed close to or beyond this frequency (Cassano *et al.*, 2009). Only the most luminous radio halos in clusters undergoing highly energetic merger events are expected to have cut-off frequencies of $\gtrsim 1$ GHz (van Weeren *et al.*, 2019). The cut-off frequency, $\nu_b$, is related to the mass of a cluster, $M$, by:

$$\nu_b \propto M^{\frac{4}{3}} \tag{1.4}$$

For merging clusters, this relation can be written as:

$$\nu_b \propto \left(1 + \frac{\Delta M}{M}\right)^3 \tag{1.5}$$

where $M$ is the mass of the main cluster and $\Delta M$ is the mass of the merging subcluster (Cassano *et al.*, 2009).

### 1.2.2 Mini-halos

Mini-halos are much smaller than their giant counterparts, with sizes ranging from 100 to 500 kpc (see Figure 1.2 for a size comparison). Examples of mini-halos in RX J1720.1+2638 and the Perseus cluster are presented in Figure 1.5. Mini-halos are typically found in relaxed cool-core clusters with the radio emission surrounding the brightest cluster galaxy (Ferrari *et al.*, 2008, van Weeren *et al.*, 2019). However, exceptions to the norm have been observed. A giant radio halo has been discovered in a cool-core cluster (see Bonafede *et al.*, 2014) but in this case the diffuse emission is thought to be caused by a merger in its earlier stages, before the cool core has been disrupted, or by a minor merger. There are also cases where sub-merger activity has influenced the morphology of radio mini-halos (e.g. Gitti *et al.*, 2007).

The synchrotron emissivity of mini-halos is generally higher than that of giant halos (Cassano *et al.*, 2008). This is due to the different environments hosting mini versus

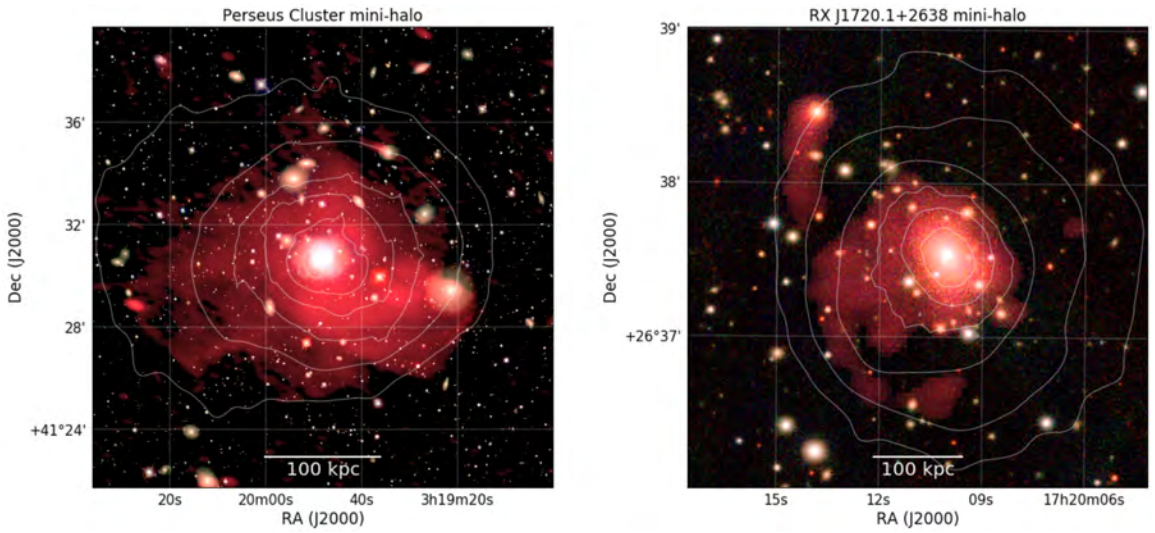


**Figure 1.5:** Composite radio-optical images of the mini-halos in the Perseus cluster (*left*) and RX J1720.1+2638 (*right*). Source: van Weeren *et al.*, 2019.

giant halos. Cool-core clusters often have high gas densities and strong magnetic fields, a combination that can lead to more efficient synchrotron emission over a small volume (Gitti *et al.*, 2015).

The turbulent re-acceleration model has also been used to explain the origin of mini-halos but, unlike giant halos, the turbulence in cool core clusters is generated by gas sloshing rather than major cluster mergers (ZuHone *et al.*, 2012). The re-accelerated electrons likely come from the central AGN (Gitti *et al.*, 2015). Mini-halos are confined by cold fronts which supports the theory that turbulence is induced by gas sloshing motions which then re-accelerate particles (Gitti *et al.*, 2015). Additionally, hadronic models —where hadronic interactions between protons and the thermal ICM are the source of the synchrotron-emitting electrons —have also been proposed to play a role in the formation of mini-halos (ZuHone *et al.*, 2015).

### 1.2.3 Radio relics

Radio relics are diffuse radio emissions found in systems with a wide range of masses. Relics are found mostly on the periphery of galaxy clusters and tend to have elongated shapes (Giovannini *et al.*, 1991, van Weeren *et al.*, 2011, Molnar and Broadhurst, 2017,

Di Gennaro *et al.*, 2018). They are believed to trace the shocks generated by merger-driven turbulence (van Weeren *et al.*, 2019). Due to the compression of magnetic fields at the shock front, relics are strongly polarised at frequencies $\gtrsim 1$ GHz with polarisation fractions $\gtrsim 20\%$ (Torsten A. Enßlin and Peter L. Biermann and Ulrich Klein and others, 1998). Examples of radio relics in Abell 3667 are shown in Figure 1.6.

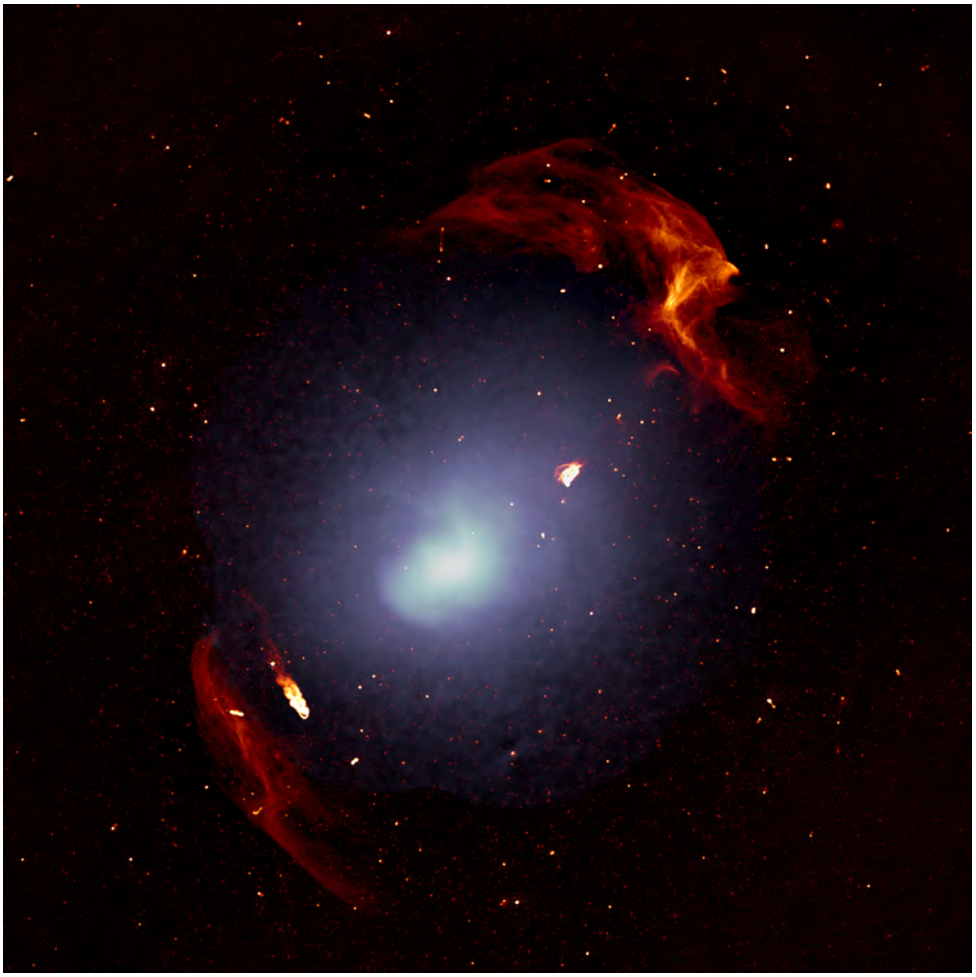

**Figure 1.6:** High resolution composite image of the double radio relics found in Abell 3667. The radio emission is seen in orange while the X-ray emission at the cluster centre is seen in white (de Gasperin, F. *et al.*, 2022).

#### 1.2.3.1 Origin

Relics form during merger events: the shock waves generated by the merger accelerate particles to relativistic speeds causing them to emit in the radio regime (Torsten A. Enßlin and Peter L. Biermann and Ulrich Klein and others, 1998). In an idealised binary merger,

as the two clusters merge, shocks are sent out into the ICM perpendicular to the direction of the merger (van Weeren *et al.*, 2011). These shocks are known as equatorial shocks and are shown in black in Figure 1.7. After the dark matter cores of the merging clusters pass through one another, two shocks are generated in opposite directions along the merger axis. These shocks are indicated in red and blue in Figure 1.7 and are known as merger shocks (van Weeren *et al.*, 2019). This model of shock generation explains why many merging systems host two radio relics along the merger axis (van Weeren *et al.*, 2011, de Gasperin *et al.*, 2014). The shock ahead of the lighter dark matter core typically has the higher kinetic energy and becomes the brighter radio shock (Molnar and Broadhurst, 2017).

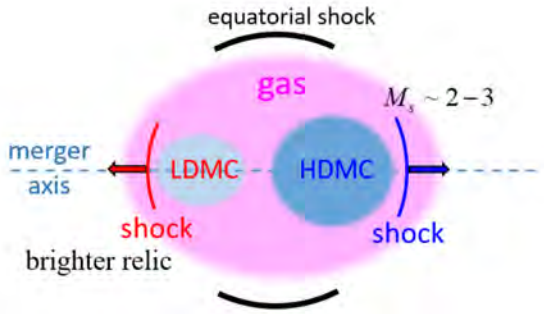


**Figure 1.7:** Schematic diagram of an idealised binary cluster merger $\sim 1$ Gyr after the dark matter core passage. Equatorial shocks are generated perpendicular to the merger axis, while merger shocks are sent out in the opposite directions along the merger axis. Source: van Weeren *et al.*, 2019.

When studying radio relics, the Mach number can be used to gain insight into the kinetic energy and energy dissipation of radio relics (Gasperin *et al.*, 2015, Akamatsu *et al.*, 2015, Labidi, 2019). The Mach number, $\mathcal{M}$, is a dimensionless quantity that describes the speed of an object relative to the speed of sound in a fluid medium (Rott, 1985). The Mach number of a shock can be derived from the ratio of the temperatures across the shock front observed in the X-ray (e.g. Akamatsu *et al.*, 2015, Kale *et al.*, 2017, Rajpurohit *et al.*, 2020b). Typical Mach numbers for radio relics range from $\sim 2$ to 4, where a Mach number of 2 indicates a weaker shock wave and $3 \sim 4$ a stronger shock wave, likely generated in highly dynamic merging clusters (Gasperin *et al.*, 2015, Rajpurohit *et al.*, 2020b). This parameter is essential for probing the energetics of the merger and the strength of the shock waves generated by the collision.

#### 1.2.3.2 Morphology

Relics are typically elongated with asymmetric brightness profiles, a sharp edge on the side furthest from the cluster and a hazy edge closer to the cluster (van Weeren *et al.*, 2019). These structures are usually seen close to edge-on, as shown in Figure 1.6. Relics with rounder or less elongated shapes have, however, been observed (see Clarke and Ensslin, 2006). Relic sizes can vary between 0.5 to 2 Mpc (van Weeren *et al.*, 2019 for a review). Some of the most notable giant, Mpc-scale relics are believed to be associated with merger events where the ratio of cluster masses is relatively small (3:2; e.g. Okabe *et al.*, 2015), while clusters with double radio shocks have larger mass ratios (e.g. Golovich *et al.*, 2017, Finner *et al.*, 2017).

The morphology of the merging clusters significantly influences the shape and size of the relics produced (Kravtsov and Borgani, 2012). Another critical factor is the collision angle. Figures 1.1 and 1.7 depict an idealised binary merger, where a head-on collision simplifies much of the underlying physics. However, in reality, perfect binary mergers are rare and the collision angle can affect the turbulence generated and, consequently, the formation of radio relics (van Weeren *et al.*, 2010, van Weeren *et al.*, 2011).

Radio relics studied with good signal to noise ratio (SNR) and high resolution often have visible substructure, fine filaments that possibly trace the changes in the magnetic fields or the complex shape of the shock surface (Ferrari *et al.*, 2008, Feretti *et al.*, 2012, van Weeren *et al.*, 2019). The substructure of relics is not yet fully understood but have been observed in numerous relics. Examples of relics with visible substructure include Abell 2256 (Clarke and Ensslin, 2006), the Toothbrush cluster (Rajpurohit *et al.*, 2018), Abell 3667 (Rottgering *et al.*, 1997) and MACS J0717.5+3745 (van Weeren *et al.*, 2017). A close-up of the filaments in the Toothbrush relic can be seen in Figure 1.8.

Radio relics often display a spectral index gradient across their width (van Weeren *et al.*, 2010, van Weeren *et al.*, 2019). The shock front usually has a flatter spectral index, while closer to the cluster centre, the spectral index steepens. This steepening is thought to result from synchrotron and inverse Compton losses downstream of the shock (Bonafede

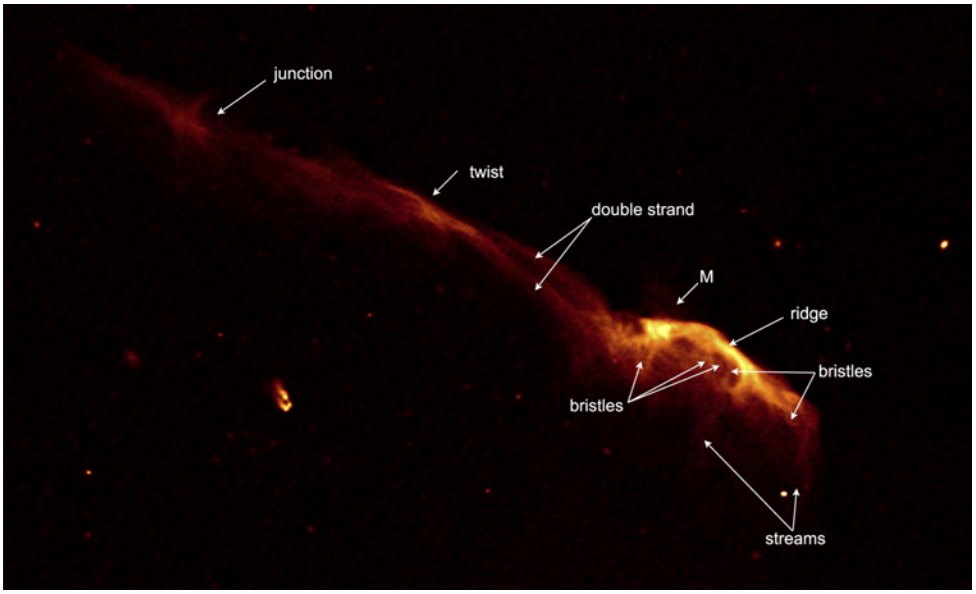


**Figure 1.8:** High resolution radio image of the Toothbrush relic showing the complex, filamentary structures. Source: Rajpurohit *et al.*, 2020a.

*et al.*, 2012). Typical integrated spectral indices for relics range from $-1.0$ to $-1.5$ (e.g Bonafede *et al.*, 2012, de Gasperin *et al.*, 2014). An example of this feature can be seen in Figure 1.9: the left edge of the relic has a spectral index of $\alpha \approx -1.0$ which steepens to $\approx -2.5$ toward the right side of the relic. This distinctive feature can aid in classifying diffuse emission as radio relics (e.g. Clarke and Ensslin, 2006, Rajpurohit *et al.*, 2022b).

Radio relics are also typically highly polarised due to the compression and alignment of magnetic fields by the merger-driven shock waves (Torsten A. Enßlin and Peter L. Biermann and Ulrich Klein and others, 1998, van Weeren *et al.*, 2010, Bonafede *et al.*, 2012, Di Gennaro *et al.*, 2018). The polarisation fraction is the ratio of the polarised intensity to the total intensity. The polarisation angle gives the orientation of the magnetic field in the plane of the sky (Condon and Ransom, 2016). In regions where the magnetic field is well-ordered or aligned, the radiation emitted is more strongly polarised. As radio relics are most commonly found on the outskirts of a cluster, regions where the ICM has relatively low density, there is a lesser degree of Faraday rotation compared to the cluster core (Torsten A. Enßlin and Peter L. Biermann and Ulrich Klein and others, 1998, van Weeren *et al.*, 2010). The lower level of Faraday rotation allows the high degree of polarisation to be preserved (Vazza *et al.*, 2012). More elongated relics usually show

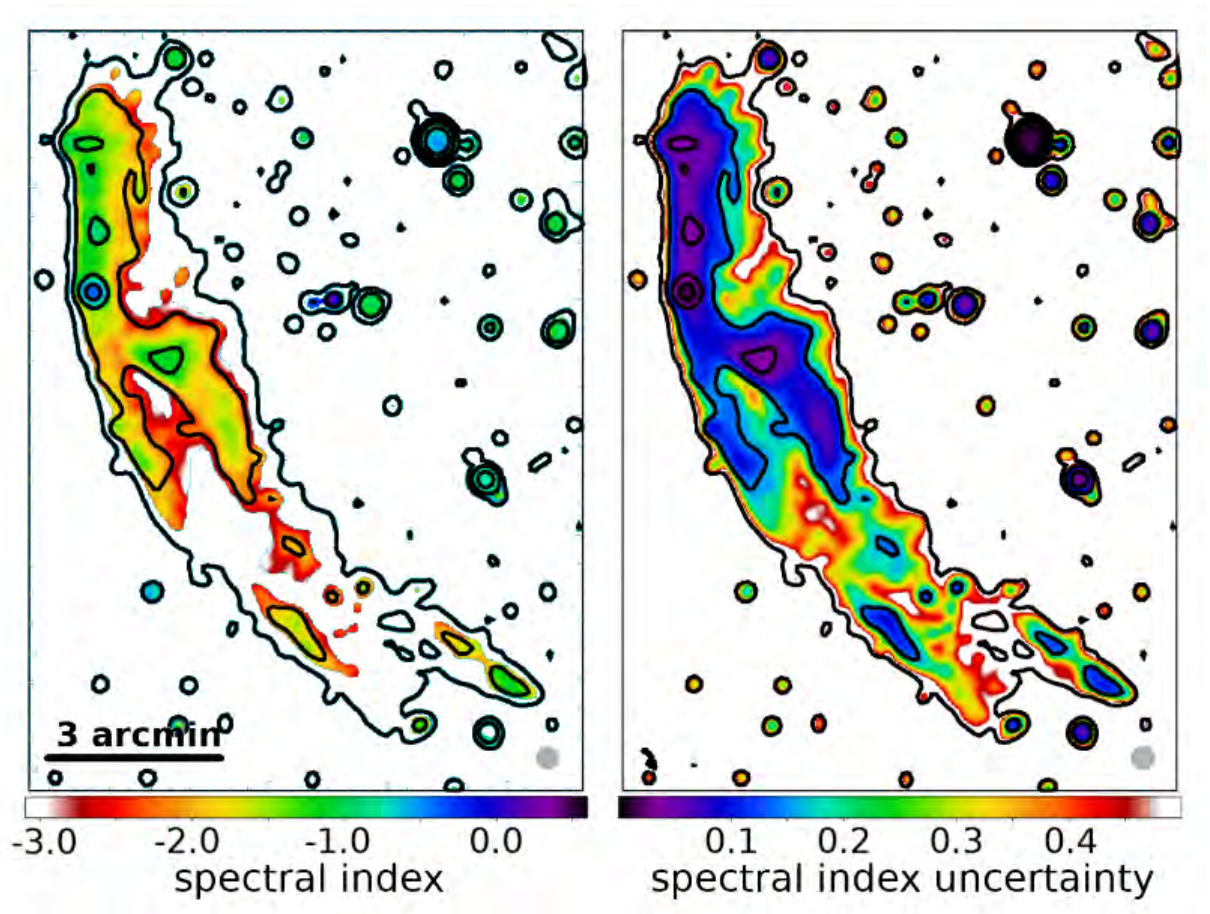


**Figure 1.9:** Spectral index map of a radio relic in MCXC J0352.4-7401. Source: Knowles *et al.*, 2022.

the highest degree of polarisation as the shock front stretches over a larger area leading to a more extensive and uniform alignment of magnetic fields (Di Gennaro *et al.*, 2018, Knowles *et al.*, 2022).

The Faraday rotation measure quantifies the rotation of the polarisation plane as radio waves move through a magnetised plasma (Carilli and Taylor, 2002). From the Faraday rotation measure, properties of the magnetic fields in the line of sight of the telescope as well as the electron density in the ICM can be inferred (Carilli and Taylor, 2002). Rotation measure synthesis is a technique used to decompose complex polarisation signals into their constituent Faraday depths, providing a more detailed picture of the magnetic field structure, distribution of ionised gas within and around the source as well as its 3-dimensional geometry (e.g. (Pizzo *et al.*, 2010, Bonafede *et al.*, 2013, Kierdorf *et al.*, 2016)).

Similar to the spectral index, the rotation measure can be displayed as a colour map over the region of interest. The left hand side of Figure 1.10 shows a rotation measure map of a relic in the Abell 3667 cluster from the MeerKAT Galaxy Cluster Legacy Survey (MGCLS; Knowles *et al.*, 2022). The colour indicates the rotation measure in radians per square meter. This map is used to find the inferred magnetic field angles across the structure which are plotted in the map on the right hand side of Figure 1.10 in order to find trends in the magnetic field of the emission.

#### 1.2.3.3 Double radio relics

Some clusters exhibit two radio relics at opposite ends of the merger axis. These are referred to as double relic systems, however, a pair of relics can only be classified as double relics if they were generated during the same merger event (van Weeren *et al.*, 2019). Double relics are proposed to be found in systems where binary merger events have occurred making them particularly valuable cases for study as they allow for more precise constraints on the cluster merger dynamics. Systems hosting double relics that

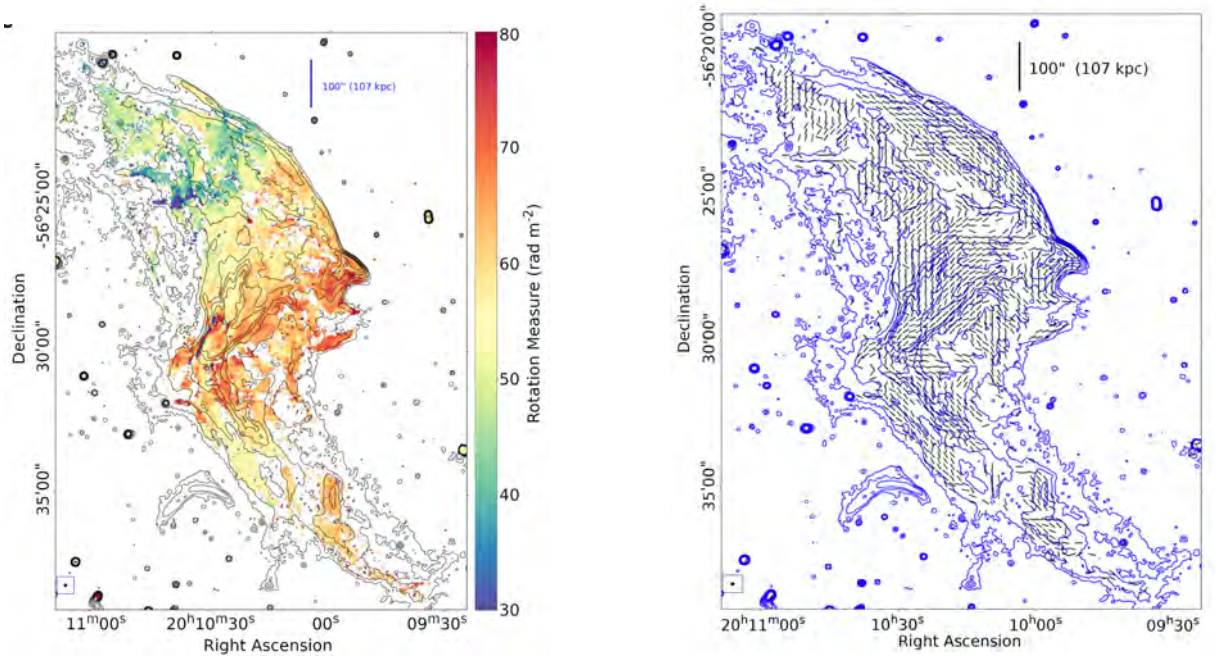


**Figure 1.10:** *Left:* Example of a rotation measure map of a relic in the Abell 3667 field. *Right:* The inferred magnetic field angles for the relic (Knowles *et al.*, 2022). The magnetic field is highly ordered along the northwestern edge of the relic indicating a high degree of polarisation.

are viewed edge-on or close to, provide an optimal viewing angle of the system (Golovich *et al.*, 2019). This perspective makes radio relics appear more prominent and elongated while enhancing the observed degree of polarisation (van Weeren *et al.*, 2011, Gasperin *et al.*, 2015, Hurley-Walker *et al.*, 2017a).

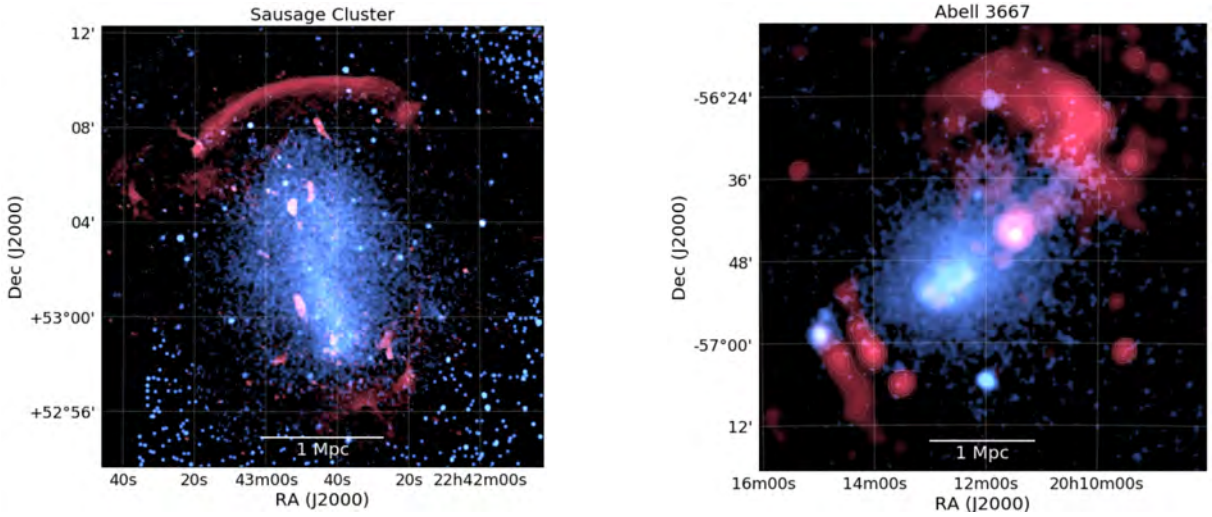


**Figure 1.11:** Examples of double radio relics. The radio emission in both images is visible in red. *Left:* Sausage cluster (van Weeren *et al.*, 2011). *Right:* Abell 3667 (Hurley-Walker *et al.*, 2017a). Source: van Weeren *et al.*, 2019.

### 1.2.4 Revived AGN fossil plasma sources and phoenices

AGN are the highly energetic regions surrounding supermassive black holes at the centres of some galaxies. These regions are powered by the accretion of matter into the black hole, a process that releases vast amounts of energy across the electromagnetic spectrum. AGN emission can manifest as intense radiation from the accretion disk and, in many cases, as jets and lobes of plasma that extend far beyond the host galaxy (Kempner *et al.*, 2004, Ferrari *et al.*, 2008).

Revived AGN fossil plasma sources and phoenices are regions of old, inactive plasma that were originally emitted by an AGN but have since faded and cooled. These sources can be re-energised by external processes, such as cluster merger shocks, turbulence or interactions with the ICM. This re-energisation can cause the fossil plasma to re-emit synchrotron radiation, resulting in diffuse and complex morphologies (Enßlin and Gopal-Krishna, 2001, Shimwell *et al.*, 2016, Wilber *et al.*, 2018, Vazza *et al.*, 2023). These

structures can take on a range of morphologies, some similar to those of radio relics, but typically have smaller sizes ($\lesssim 300 - 400$ kpc), lower radio powers and steeper spectra (Enßlin and Gopal-Krishna, 2001, Kempner *et al.*, 2004, Riseley *et al.*, 2022). Unlike active AGN, where emission is directly powered by ongoing accretion onto the central black hole, revived fossil plasma sources and phoenices are typically powered by external re-energisation mechanisms such as merger activity (Ferrari *et al.*, 2008, van Weeren *et al.*, 2009, de Gasperin *et al.*, 2017, Mandal *et al.*, 2020).

Some examples of radio phoenices and revived fossil plasma sources are presented in Figure 1.12. The southern structure in the Abell 1132 image has a similar morphology to a radio relic. The elongated arc-like shape could easily be mistaken for a radio relic in a low SNR image.

### 1.2.5 Statistical studies

Many breakthroughs in the study of diffuse emission can be attributed to large-scale statistical surveys (e.g. Venturi *et al.*, 2007, Cuciti *et al.*, 2015). The connection between diffuse emissions, such as radio halos and relics, and merger activity stems from such surveys (Cassano *et al.*, 2010). However, these surveys were restricted to high-mass systems

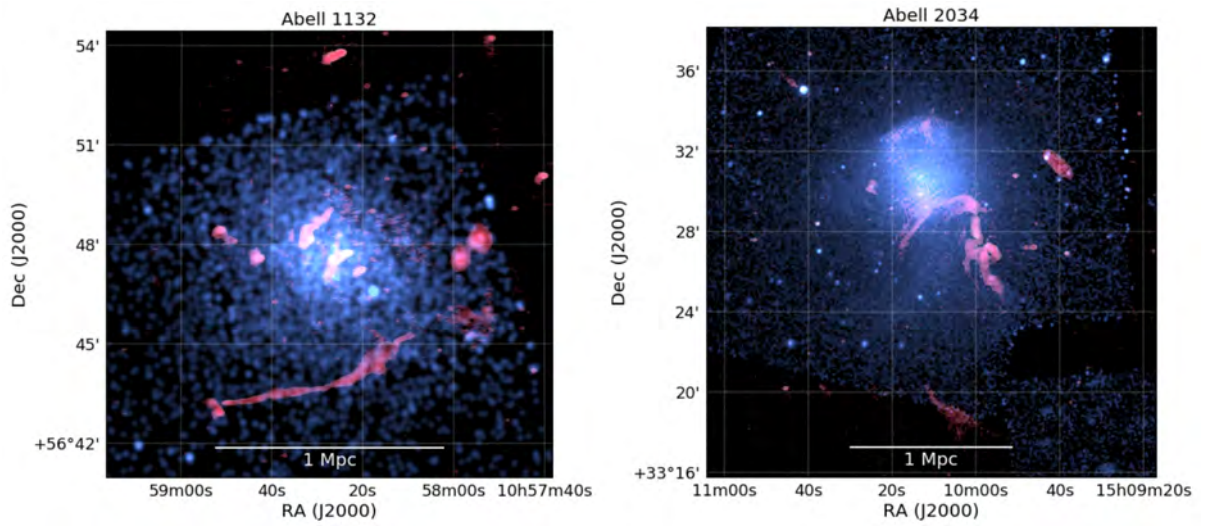


**Figure 1.12:** Examples of revived AGN sources in Abell 1132 (Wilber *et al.*, 2018) and Abell 2034 (Shimwell *et al.*, 2016). The radio emission is visible in red. Source: van Weeren *et al.*, 2019.

($M_{500} \gtrsim 6 \times 10^{14}\ M_{\odot}$) at low redshift ranges ($0.1 \gtrsim z \gtrsim 0.4$) leading to correlations within these boundaries (Venturi *et al.*, 2007, Cuciti *et al.*, 2015). More recently, studies such as Di Gennaro *et al.* (2021) and Botteon *et al.* (2022) have aided in expanding the parameter space of cluster mass and redshift explored in previous studies, the latter providing the largest statistical sample of galaxy clusters to date.

Turbulent re-acceleration formation theories predict a sharp drop in the number of radio halos at higher redshifts, where cluster magnetic fields are expected to be weaker (Cassano and Brunetti, 2005, Brunetti and Jones, 2014). There are also low mass systems (e.g. Bernardi *et al.*, 2015, Knowles *et al.*, 2016, Kale *et al.*, 2017, Hoang *et al.*, 2020) and systems outside the redshift range ($z > 0.5$; e.g. Bonafede *et al.*, 2009, Lindner *et al.*, 2014, Giovannini *et al.*, 2020) which host diffuse emission. In order to impose more stringent constraints on formation theories, statistical samples outside these ranges need to be observed.

The MeerKAT Exploration of Relics, Giant Halos, and Extragalactic Radio Sources survey (MERGHERS; Knowles *et al.*, 2016, Knowles *et al.*, 2021) is a large-scale follow-up survey of SZ-selected clusters. The target clusters form part of the Atacama Cosmology Telescope (ACT) data release 5 catalogue of more than 4000 optically confirmed clusters (Hilton *et al.*, 2021). The survey is blind to the dynamic state of the clusters and will provide an unbiased sample of clusters. The MERGHERS survey aims to probe the evolution of diffuse cluster radio emission and magnetic fields by observing a statistically significant sample (approximately 200) of galaxy clusters (Knowles *et al.*, 2016, Knowles *et al.*, 2021).

## 1.3 Multi-wavelength studies

In the search for diffuse emission, classifying radio sources can be challenging when the viewing angle is unfavourable; sources such as radio relics can easily be missed or incorrectly classified. When viewed edge-on, distinguishing radio halos from relics is relatively straightforward, as they are typically located in different regions of the cluster and exhibit distinct morphologies (Golovich *et al.*, 2019). However, phoenices and revived fossil

plasma sources can exhibit morphologies resembling either radio halos or relics. Projection effects may cause these sources to appear as if they are located at specific positions in the cluster, such as the cluster centre—where they might be mistaken for a radio halo—or the outskirts—where they may be confused with a radio relic. Projection effects and the viewing angle can also distort the emission, especially when two kinds of emission are coincident (e.g. Clarke and Ensslin, 2006, Skillman *et al.*, 2013, Rajpurohit *et al.*, 2022b, Lusetti *et al.*, 2023). In such cases, surface brightness profiles, polarisation, rotation measure, and spectral index mapping can aid in the classification process.

Galaxy clusters can be probed using observations across the electromagnetic spectrum. The primary focus of the data reduction techniques in this thesis is on radio data but archival data at various wavelengths is used to probe different aspects of the targets. By combining studies across different wavelengths, we can construct a holistic view of cluster evolution, which can then be used to improve existing models and theories.

Radio data is typically used to create radio maps or images which depict the radio sources and can be used to identify their morphology. Radio images are crucial for determining the origin of radio emission and can be used to study the interaction of the emission with the ICM. The procedure used to make these maps is known as synthesis imaging and will be discussed in Chapter 2. An example of a continuum radio image can be seen in Figure 1.13.

Surface brightness is a measure of the intensity of radio emission (flux density) per unit area on the sky. The flux density of a source, $S$, is the amount of radio power per unit area per unit frequency, commonly measured in Janskys (Jy), where 1 Jy = $10^{-26}$ W/m$^2$/Hz.. The bright spots visible in the image indicate regions of strong emission. Even the seemingly empty areas of the image exhibit a measurable flux density, commonly known as the root mean square (RMS) noise. This value varies based on factors like observation duration and the instrument used to take the measurements. These factors are discussed in Section 2.1.3. The surface brightness profile of a radio source can reveal variations in the emission intensity which can aid in identifying shock fronts and classifying radio sources (Lindner *et al.*, 2014, Lusetti *et al.*, 2023).

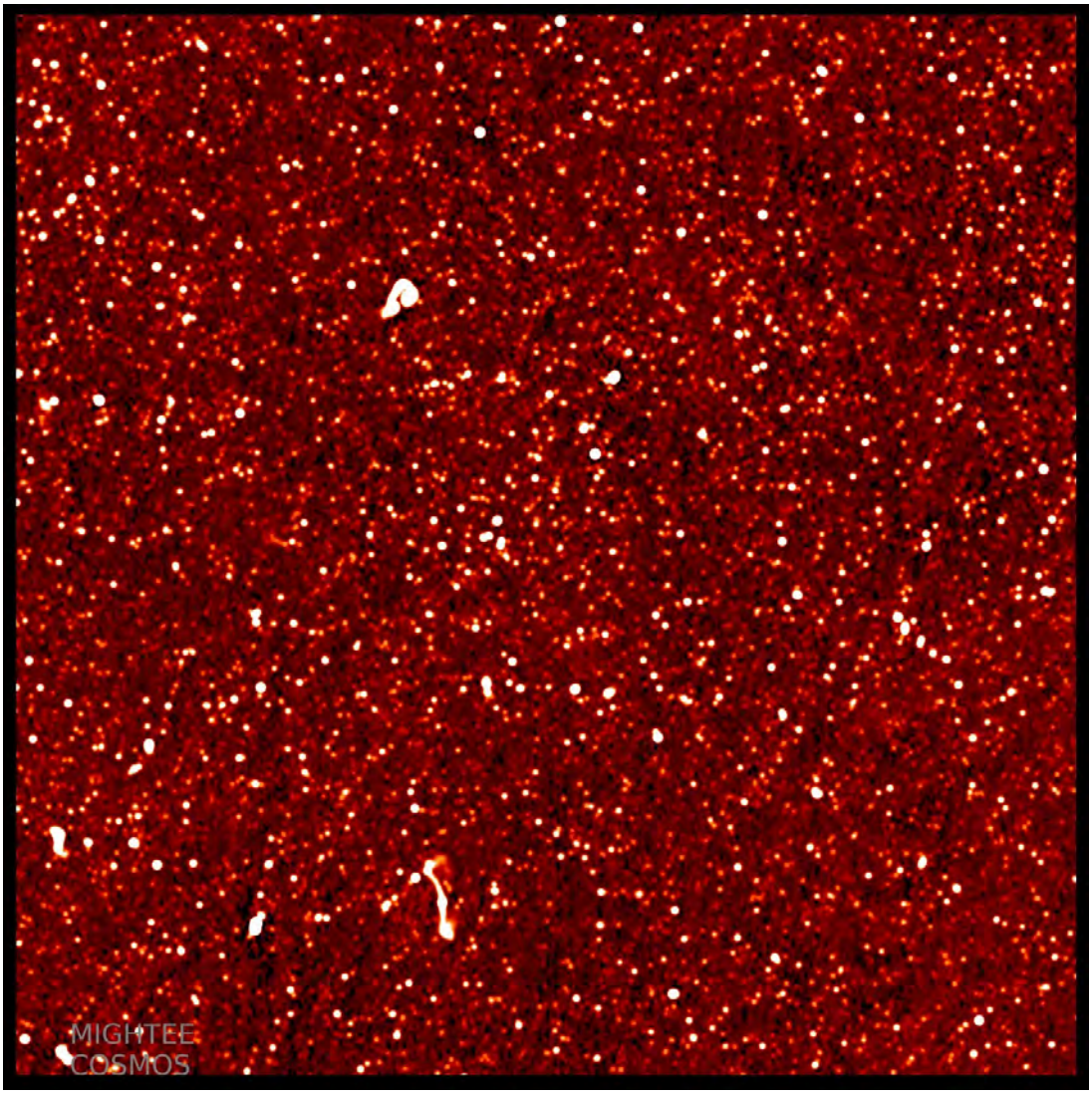


**Figure 1.13:** Example of a high resolution radio continuum map from the MeerKAT International GHz Tiered Extragalactic Exploration (MIGHTEE) Survey (Hale *et al.*, 2024).

### 1.3.1 Optical and infrared

Radio data suffers from projection effects, where all sources in the radio image are projected onto a 2D plane without any indication of depth or redshift. Redshift information is crucial for distinguishing between nearby and distant sources, especially in studies of large-scale structures like galaxy clusters. Electromagnetic waves from distant sources lose energy as they traverse space, causing their wavelengths to stretch, a phenomenon known as redshift (Condon and Ransom, 2016). This effect is observed across the elec-

tromagnetic spectrum, including in the radio band. Unlike the optical regime, where this stretching shifts signals from blue to red wavelengths, the continuum radio spectrum is mostly featureless, making redshift determination more challenging. However, photometric and spectroscopic methods provide powerful tools for estimating the redshifts of sources (Newman and Gruen, 2022).

Spectroscopic redshifts are determined by directly measuring the shift in the wavelength of spectral lines in a source's spectrum using optical spectrographs. The position of features such as emission or absorption lines are compared to known rest-frame wavelengths (Hogg *et al.*, 1998). This method is the most accurate but requires more telescope time and resources. In contrast, photometric redshifts are derived from multi-band optical photometry. The observed flux in each band (e.g., *u, g, r and i* bands) is compared with theoretical or empirical templates of the source's spectral energy distribution to estimate the redshift (Hogg *et al.*, 1998). While photometric redshifts are faster to obtain, they are less accurate (Hildebrandt *et al.*, 2008, Ilbert *et al.*, 2009).

Large-scale optical/infrared surveys such as the Sloan Digital Sky Survey (SDSS; Abazajian *et al.*, 2003), Two Micron All Sky Survey (2MASS; Skrutskie *et al.*, 2006), Cluster Lensing And Supernova survey with Hubble (CLASH; Postman *et al.*, 2012), Panoramic Survey Telescope and Rapid Response System Surveys (Pan-STARRS; Chambers *et al.*, 2016), the Dark Energy Survey (DES; Dark Energy Survey Collaboration *et al.*, 2016), Dark Energy Camera Legacy Survey (DECaLS; Dey *et al.*, 2019), and many more, provide wide coverage and can be used to estimate photometric redshifts for targets in other surveys (e.g. Kesebonye *et al.*, 2022). Redshift estimates can be used to determine the radial velocities of galaxies relative to the cluster centre (Loubser *et al.*, 2018). This allows for the calculation of the velocity dispersion, a key parameter that quantifies the range of velocities of galaxies within the cluster. The velocity dispersion reflects the dynamics within a cluster and is closely linked to merger activity (Nascimento *et al.*, 2018). High velocity dispersions are indicative of a disturbed or merging cluster environment, whereas lower, more uniform dispersions suggest more stable, virialized systems (Loubser *et al.*, 2018, Nascimento *et al.*, 2018).

An example of an optical image from the Hubble Space Telescope can be seen in Figure 1.14. Distant galaxies appear red due to higher redshifts, while closer galaxies exhibit blue hues, reflecting their shorter wavelengths. The brightest cluster galaxy, typically located near the gravitational centre of the cluster, can be identified through optical observations (Chu *et al.*, 2021). This often defines the cluster's core and acts as a point of reference when measuring cluster-centric distances for member galaxies and aligning multiwavelength observations with the cluster centre.

**Figure 1.14:** Optical image from the Hubble Space Telescope of the galaxy cluster MACS J1206. Image credit: NASA, ESA, M. Postman (STScI) and the CLASH Team

### 1.3.2 X-ray

Galaxy clusters are some of the brightest X-ray sources in the sky (Giacconi *et al.*, 1972). When observed at X-ray wavelengths, the ICM emits thermal bremsstrahlung radiation (Henriksen and Mushotzky, 1986). Bremsstrahlung radiation is produced when

one charged particle decelerates due to the electric field of another charge. The moving particle loses kinetic energy, which is converted into thermal emission that can be detected at X-ray wavelengths (Rybicki and Lightman, 1991). These interactions take place at non-relativistic speeds, making X-ray observations crucial for studying the dense, hot plasma in galaxy clusters.

The X-ray surface brightness is directly related to the gas density and temperature in the ICM. Since X-ray emission is primarily due to thermal bremsstrahlung, the surface brightness, $I$, is a function of the gas temperature and also roughly scales as:

$$I_{\rm x} \propto \eta_e^2 \tag{1.6}$$

where $\eta_e^2$ is the electron density (Sarazin, 1986). The distribution of X-ray surface brightness across the cluster provides information about the structure and dynamical state of the cluster. Cool-core clusters typically exhibit a bright, peaked X-ray surface brightness profile at the centre, indicating a dense cool core. Non-cool core clusters have a more uniform surface brightness profile, suggesting a more disturbed state (Gitti *et al.*, 2015).

The X-ray luminosity of a cluster is related to its mass and has been used as a mass proxy for targeting massive clusters. Giant radio halos in X-ray selected clusters have been found to satisfy scaling relations with the thermal properties of the cluster (Cassano *et al.*, 2013). Clusters hosting giant radio halos were found to show an overall positive radio halo power and X-ray luminosity correlation, given by $P_{1.4\,\rm GHz} \propto L_X^{\beta}$ (Cassano *et al.*, 2010, 2013). This statistically defined relation revealed the existence of a bimodal behaviour in the radio power and X-ray luminosity of galaxy clusters. Clusters hosting radio halos lie on the correlation, while clusters without radio halos have radio upper limits below the correlation (Brunetti *et al.*, 2007).

While surface brightness maps reveal the density distribution, temperature maps derived from X-ray spectral fitting provide a more detailed view of the cluster's thermodynamic state. These maps can uncover the presence of shocks, cold fronts, and other dynamical

features, often associated with mergers or interactions within the cluster (ZuHone *et al.*, 2012, Rajpurohit *et al.*, 2021).

X-ray observations play a crucial role in multiwavelength studies of clusters. For example, radio emissions can often have X-ray counterparts making X-ray observations useful for identifying shock fronts in the ICM and classifying radio emission (Oozeer *et al.*, 2021, Pillay *et al.*, 2021, Rajpurohit *et al.*, 2021).

### 1.3.3 Sunyaev-Zel'dovich emission

The SZ effect arises from inverse Compton scattering, where low-energy CMB photons interact with high-energy electrons in the hot ICM of galaxy clusters (Sunyaev and Zeldovich, 1972). The CMB photons gain energy and cause a characteristic distortion in the spectrum of the CMB. This distortion is observable as a decrement in the intensity at low frequencies and an increment at high frequencies.

High-resolution SZ-mapping involves the use of interferometers or single-dish telescopes with large apertures, such as the Planck Telescope (Martin *et al.*, 2004), Atacama Cosmology Telescope (ACT; Swetz *et al.*, 2011) or the South Pole Telescope (SPT; Ruhl *et al.*, 2004). These instruments map the SZ signal across the sky with high angular resolution and sensitivity (Benson *et al.*, 2014, Ade *et al.*, 2016, Datta *et al.*, 2018, Orlowski-Scherer *et al.*, 2022). This allows the detection of individual galaxy clusters and any substructures within them. High-resolution SZ maps can reveal shocks, cold fronts, and substructures in the ICM caused by cluster mergers or interactions (Di Mascolo *et al.*, 2019, Di Mascolo *et al.*, 2021, Orlowski-Scherer *et al.*, 2022).

The SZ effect is independent of redshift and depends only on the pressure of the ICM, which is related to the cluster mass and can be used to probe the spatial pressure distribution within the ICM and the total cluster mass (Birkinshaw *et al.*, 1984). Using SZ-selected galaxy cluster samples provides a mass-limited selection function which can be useful when studying clusters in specific mass ranges (e.g. Cuciti *et al.*, 2021).

## 1.4 This thesis

Statistical surveys are crucial for understanding the prevalence, properties, and evolution of diffuse radio sources in galaxy clusters. By providing large datasets, these surveys enable population-level studies that reveal broad trends in cluster merger activity. In addition to these broad surveys, follow-up studies of individual clusters are valuable for probing the detailed dynamics and interactions within specific systems. These studies offer insights into how diffuse radio emission traces non-thermal processes, such as shock waves and turbulence, and help identify the mechanisms responsible for their generation. These targeted studies provide an opportunity to refine the methodologies used to investigate cluster dynamics and apply them more effectively to the broader statistical sample.

In this thesis, we conduct radio spectral studies on three SZ-selected MERGHERS clusters, ACT-CL J0034+0225, ACT-CL J0137-0827 and ACT-CL J0330+5228, to investigate the complex physical processes occurring in the clusters. In Chapter 2, we introduce key concepts in radio astronomy, interferometry, and imaging. We also present the datasets, detail the calibration procedure, and describe the post-processing tests applied to the calibrated images. In Chapter 3, we present and discuss the results of the analyses performed on the calibrated images. In Chapter 4, we perform a multiwavelength investigation of serendipitous diffuse radio emission discovered in one of the cluster fields. Finally, in Chapter 5, we summarise our findings and outline potential directions for future research based on our results.

In this thesis we assume a flat ΛCDM cosmology with $H_0 = 70$ kms$^{-1}$Mpc$^{-1}$, $\Omega_{\rm m} = 0.3$, and $\Omega_\Lambda = 0.7$. We define the radio spectral index, $\alpha$, such that $S_\nu \propto \nu^\alpha$, where $S_\nu$ is the flux density at the frequency $\nu$. $R_{200}$ is the radius within which the density is 200 times that of the critical density of the Universe.

# Chapter 2

# Radio Data Processing

## 2.1 Interferometry

An antenna is a transducer that converts energy from one form to another. In the case of radio antennas, energy is converted from an electrical signal into an EM wave or vice versa (Monebhurrun, 2019). A wide range of antennas can be used to detect radio waves. The angular resolution of the telescope, $\theta$, refers to the smallest angular distance distinguishable by the instrument and is related to the largest dimension of the antenna, $D$, by:

$$\theta \approx 1.22 \times \frac{\lambda}{D} \tag{2.1}$$

where $\lambda$ is the maximum operational wavelength of the telescope (Wrobel and Walker, 1999).

Although antennas such as the parabolic reflector antenna can detect a wide range of frequencies, the radio band is wide and cannot be covered entirely by a single radio telescope. There is also a practical limit on the size of the antenna, which limits the angular resolution of the telescope. In order to improve the resolution, field of view, and sensitivity, interferometers are used. An interferometer is made up of an array of co-observing antennas and measures visibilities or the phase and amplitude of cross-correlated

signals between pairs of antennas in the array (Condon and Ransom, 2016). This allows for telescopes with much larger effective dimensions to be built, as the antennas in the array do not need to be as large as single dish telescopes to achieve the same (or improved) resolution. The resolution of an interferometer is given by Equation 2.1 where the largest dimension D is replaced with the longest baseline of the interferometer.

For an interferometer made up of $N$ antennas, the effective collecting area of the telescope is $N$ times larger than that of a single dish telescope. The interferometer can also contain as many antennas as desired (Condon and Ransom, 2016). Examples of interferometers include the Karl G. Jansky Very Large Array (Thompson *et al.*, 1980, Perley *et al.*, 2011) and the MeerKAT Telescope (Jonas and MeerKAT Team, 2016) which are both capable of providing highly detailed observations of the radio sky.

### 2.1.1 Two-element quasi-monochromatic interferometer

The simplest kind of interferometer is made up of only two antennas or "elements". The voltage outputs of the elements are multiplied and averaged to produce a single voltage reading for the interferometer as a whole (Condon and Ransom, 2016). A diagram of a two-element interferometer is presented in Figure 2.1, where the vector $\vec{b}$ is the baseline vector which denotes the displacement between elements, $\hat{s}$ is the direction of the observed source in the sky and $\theta$ is the angle between $\vec{b}$ and $\hat{s}$. Both antennas are identical and point in the same direction, but because of the distance between antenna 1 and 2, there is a delay in the signal received by antenna 1 called the geometric delay, $\tau_g = \vec{b} \cdot \hat{s}/c$. This delay represents the additional distance travelled by the signal to reach antenna 1. The output voltages of antennas 1 and 2 are identical except for the time delay experienced by antenna 1.

This example uses a very narrow frequency band thus this interferometer is known as a quasi-monochromatic interferometer. The frequency band is defined to be:

$$\Delta\nu \ll \frac{2\pi}{\tau_g} \tag{2.2}$$

with a centre frequency of $\nu = \omega/2\pi$, where $\omega$ is the phase of the signal. The output voltage of each antenna can then be written as:

$$V_1 = V\cos\left[\omega(t-\tau_g)\right] \quad \text{and} \quad V_2 = V\cos\left(\omega t\right) \tag{2.3}$$

where $V$ is the input voltage.

The total output of the interferometer is found by multiplying and time averaging the two output voltages to give the response, $R$, of the interferometer.

$$\begin{aligned} R &= \langle V_1 V_2 \rangle \\ &= \left(\frac{V^2}{2}\right)\cos\left(\omega\tau_g\right) \end{aligned} \tag{2.4}$$

The output amplitude is proportional to the flux density (power of the radiation per unit area per unit frequency) of the source and the phase, $\omega\tau_g$, is dependent on the time delay and the frequency. As the Earth rotates, the output voltage varies as the rotation changes

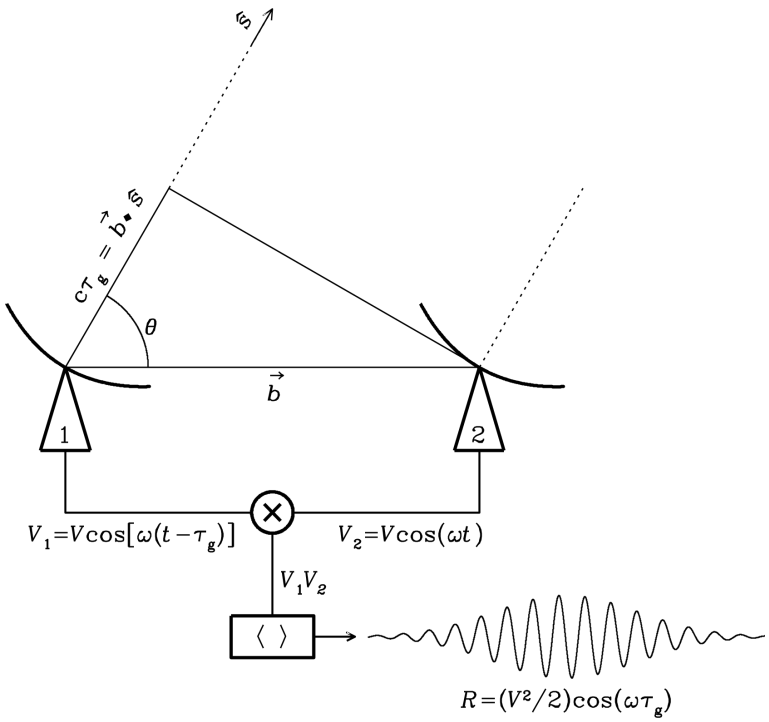


**Figure 2.1:** A two-element interferometer with identical antennas, labelled 1 and 2, and a cosine correlator which amplifies, multiplies and time averages the voltages from the antennas to give the total response of the interferometer, R (Condon and Ransom, 2016).

the angle between the source direction and baseline vector. The response is a sinusoid, $\cos(\omega\tau_g)$, multiplied by the product of the antennas' voltage patterns. Since the antennas are identical, the term $\frac{V^2}{2}$ is the power pattern of the individual antennas or the "primary beam". The primary beam represents the receiving pattern of each individual antenna in the array (Napier, 1999).

### 2.1.2 Multi-element interferometer

Extending the number of elements in the array to $N$ provides $N(N-1)/2$ pairs of antennas. Each pair can be treated like a two-element interferometer so that the point source response or synthesized beam is obtained by averaging the outputs of each antenna pair (Thompson *et al.*, 2017). The synthesized beam represents the effective resolution of the telescope, achieved by combining the sensitivity patterns of all antennas in the array. Because the antennas are directional, the interferometer can only receive a finite range of angular frequencies with a central frequency of $b \sin \frac{\theta}{\lambda}$. The antenna diameters must be smaller than the baseline, which means that the frequency response cannot extend down to zero. To find the spacings $b < D$ a single dish radio telescope with a diameter greater than the baseline can be used (Condon and Ransom, 2016).

### 2.1.3 The radiometer equation

A radiometer is a radio receiver used to measure the average power of the noise coming from a radio telescope in a well-defined frequency range. The radiometer equation describes the relationship between the signal-to-noise ratio (SNR), the system noise ($T_{sys}$), the number of antennas ($N$), integration time ($\tau$), and the bandwidth ($\Delta\nu$) (UC Berkeley, 2012, Condon and Ransom, 2016). This equation can be used to estimate the sensitivity or noise level of an observation:

$$\mathrm{SNR} = \frac{T_{src}}{T_{rms}} \quad = \frac{T_{src}}{T_{sys}}\sqrt{\Delta\nu\tau}, \tag{2.5}$$

where, $T_{src}$ is the temperature of the target source. $T_{sys}$ is the system temperature which

contains contributions from the receiver noise (thermal noise) and from everything above the antenna that is not intended to be detected. Typically, $T_{src} < T_{sys}$, which means that the system noise, $T_{rms}$, needs to be minimised in order to detect the source.

The system equivalent flux density (SEFD), the flux density as detected by the system, is the flux density equivalent of $T_{sys}$:

$$\text{SEFD} = \frac{2kT_{sys}}{A_e}, \tag{2.6}$$

where $A_e$ is the effective area of the instrument. The lower the SEFD, the more sensitive the instrument (NRAO, 2024). The radiometer equation can be expressed in terms of the SEFD as:

$$\sigma = \frac{\text{SEFD}}{\sqrt{N(N-1)\Delta\nu\tau}}, \tag{2.7}$$

where the greater the bandwidth and integration time, the smaller the flux density variations. The factor of $N(N-1)$ comes from the expression for the number of baselines in the array (Condon and Ransom, 2016).

### 2.1.4 An interferometer's view of the sky

The primary goal of interferometry is to reconstruct the true image of the sky, representing the actual brightness distribution, $I$, across the sky plane. The sky plane is the 2-D projection of the celestial sphere or sky dome (see Figure 2.2; Isella, 2011). When an interferometer observes the sky, it does so discretely due to the finite number of antennas, each having a specific field of view (primary beam). These discrete observations are governed by the sampling function, which describes how the interferometer captures limited portions of the sky at any given moment (Clarke, 1999).

Individual views of the sky from each antenna, determined by the primary beam and sampling function, form a set of visibilities. When combined, these visibilities form an interference pattern known as the visibility function, $V(u, v)$. The spatial frequency domain

of the sky is represented in frequency space as a plane where each point $(u, v)$ corresponds to a baseline vector between two antennas in the array. The coordinates $(u, v)$ are measured in units of wavelength, $\lambda$, and describe the projected baseline length and orientation in the sky plane. The visibility function is sampled at discrete points in the uv-plane. The length of the vector $(u, v)$ corresponds to the inverse of the baseline length (Clarke, 1999).

The relationship between these planes and the celestial sphere is illustrated in Figure 2.2. The sky, represented as a dome in this image, can be approximated as a flat plane with coordinates $(l, m)$—direction cosines relative to the line of sight—when observing small angular regions of the sky (typically less than $\sim 2$ degrees). While objects may appear flat in this sky-plane approximation, they are inherently curved on the celestial sphere.

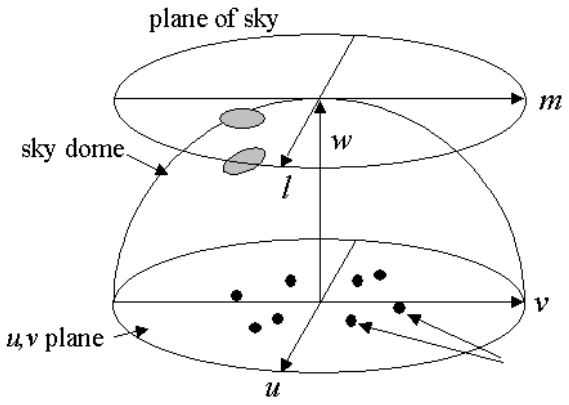


**Figure 2.2:** The relationship between the sky plane, celestial sphere or sky dome and the uv-plane are depicted. The grey circle on the sky plane is a 2-D projection of a grey circle on the celestial sphere (Isella, 2011).

This approximation holds for baselines with small $w$-components, as the $w$-term represents the deviation caused by the sky's curvature. However, baselines with significant $w$-components can introduce distortions, especially near the edges of the image (Isella, 2011). The relationship between the measured visibilities and the true sky brightness is given by Equation 2.8:

$$V(u,v,w) = \iint_{-\infty}^{+\infty} I(l,m) e^{-2i\pi(ul+vm+w(\sqrt{1-l^2-m^2}-1))} \frac{dldm}{\sqrt{1-l^2-m^2}}. \tag{2.8}$$

The visibilities are related to the brightness distribution by the van Cittert-Zenike theorem which states that the spatial visibility function, $V(u, v, w)$, is the Fourier transform of the brightness intensity distribution $I(l, m)$ (Clarke, 1999). It is possible to reduce the integral in Equation 2.8 to a 2-D Fourier transform by enforcing two conditions:

1. The interferometer array is coplanar, such that the $w$-component of the baseline can be ignored.
2. For small values of $l$ and $m$ ($l, m \ll 1$), the $w$-component can be ignored.

Under either of these two conditions, Equation 2.8 simplifies to:

$$V(u, v) = \iint_{-\infty}^{+\infty} I(l, m) e^{-2i\pi(ul+vm)} \, dldm. \tag{2.9}$$

The Fourier transform enables the translation from the spatial domain (the sky-plane) to the frequency domain (the uv-plane). By taking an inverse Fourier transform of the visibility function in the uv-plane, we can obtain the brightness distribution, $I_\nu(l, m)$, at the observing frequency, $\nu$:

$$\begin{aligned} I_\nu(l, m) &= \iint_{-\infty}^{+\infty} V(u, v) e^{-2\pi(ul+vm)} \, dudv \\ &= \mathcal{F}^{-1}[V(u, v)]. \end{aligned} \tag{2.10}$$

As the visibilities are sampled at discrete points in the uv-plane, the inversion must depend on the sampling function, $S(u, v)$, to account for the discrete data points. Instead of the true sky brightness, $I_\nu(l, m)$, we now get a dirty image, $I_\nu^D(l, m)$, which retains effects of the sampling function:

$$I_\nu^D(l, m) = \mathcal{F}^{-1}[V(u, v)S(u, v)]. \tag{2.11}$$

Using the convolution theorem, the Fourier transform of the product of $V$ and $S$ is the Fourier transform of the convolution of $V$ and $S$ (D.S. Briggs, 1999):

$$\begin{aligned}\mathcal{F}^{-1}[V(u,v)S(u,v)] &= \mathcal{F}^{-1}[V(u,v)] * \mathcal{F}^{-1}[S(u,v)] \\ &= I_\nu(l,m) * \mathcal{F}^{-1}[S(u,v)] \\ &= I_\nu(l,m) * P(l,m).\end{aligned} \tag{2.12}$$

The inverse Fourier transform of the sampling function is the point spread function (PSF), $P(l,m)$—also known as the dirty beam of the interferometer. The goal of radio synthesis imaging is to remove the effects of the PSF from the true sky brightness; a process called deconvolution is used to achieve this (T. Cornwell, 1999).

### 2.1.5 The radio interferometry measurement equation

Radio signals from celestial objects can be affected by a multitude of propagation effects along the paths over which they travel. Corruptions can occur due to atmospheric effects, solar conditions and the receiver electronics. The radio interferometer measurement equation (RIME) takes these effects into account allowing corrections to be applied to radio data during the calibration procedure. This section provides an overview of the RIME and calibration using the RIME.

For a single source, $\mathbf{e}$, assuming all corruptions occur along the signal's path, the corruptions can be represented as a $2 \times 2$ matrix $\mathbf{J}$:

$$\mathbf{e}' = \mathbf{J}\mathbf{e}, \tag{2.13}$$

where $\mathbf{J}$ is a complex Jones matrix (Jones, 1941). Each corrupting effect along the signal's path can be represented as a Jones matrix. The resulting chain of matrices is known as a *Jones chain* and represents the corrupting effects in the order in which they affect the signal.

The correlator products of two antennas can be written as:

$$V_{pq} = 2\left\langle \mathbf{v}_p \mathbf{v}_q^H \right\rangle. \tag{2.14}$$

Where the signals received by both antennas have independent paths, $p$ and $q$, and thus different corrupting effects. A total Jones matrix for each path is substituted into Equation 2.14 to obtain:

$$V_{pq} = 2\left\langle \mathbf{J}_p \mathbf{e}(\mathbf{J}_q \mathbf{e})^H \right\rangle = 2\mathbf{J}_p \left\langle \mathbf{e}\mathbf{e}^H \right\rangle \mathbf{J}_q^H = 2\mathbf{J}_p \begin{pmatrix} \langle e_x e_x^* \rangle & \langle e_x e_y^* \rangle \\ \langle e_y e_x^* \rangle & \langle e_y e_y^* \rangle \end{pmatrix} \mathbf{J}_q^H. \tag{2.15}$$

The terms in brackets in Equation 2.15 are related to the Stokes parameters (Smirnov, 2011a). The Stokes $I$ parameter represents total intensity, $Q$ and $U$ are the linear polarisation terms and $V$ is the circular polarisation term. The matrix in 2.15 can be written in terms of the Stokes parameters to form the brightness matrix, $\mathcal{B}$:

$$2\begin{pmatrix} \langle e_x e_x^* \rangle & \langle e_x e_y^* \rangle \\ \langle e_y e_x^* \rangle & \langle e_y e_y^* \rangle \end{pmatrix} = \begin{pmatrix} I+Q & U+iV \\ U-iV & I-Q \end{pmatrix} = \mathcal{B}, \tag{2.16}$$

which represents the true sky brightness. Using $\mathcal{B}$, the RIME can be written as:

$$V_{pq} = \mathbf{J}_p \mathcal{B} \mathbf{J}_q^H. \tag{2.17}$$

When expanding the Jones matrices, we get the onion form of the RIME. The effects with the smallest values of $m$ and $n$ occur at the source, and moving outward in Equation 2.18, effects occur closer to the antennas. In Equation 2.18, $n \neq m$ as the signals received by antennas $p$ and $q$ travel along different paths:

$$V_{pq} = \mathbf{J}_{pn}(\mathbf{J}_{pn-1}(...(\mathbf{J}_{p1}\mathcal{B}\mathbf{J}_{q1}^H)...)\mathbf{J}_{qm-1}^H)\mathbf{J}_{qm}^H. \tag{2.18}$$

The phase delay is an intrinsic effect which needs to be accounted for. The difference in path length of two received signals affects the phase of the signals even in the absence of corrupting factors. The derivation of the phase delay Jones matrix or K-Jones matrix can

be found in Smirnov (2011a). The visibility of a single uncorrupted source measured by an ideal interferometer with no corrupting effects can be written as:

$$V_{pq} = \mathbf{K}_p \mathcal{B} \mathbf{K}_q^H = X_{pq}, \tag{2.19}$$

where $\mathbf{K}$ is the delay matrix and $X_{pq}$ is the source coherence function. The $\mathbf{K}$ matrix can be expressed as:

$$\mathbf{K} = \begin{pmatrix} e^{i\phi} & 0 \\ 0 & e^{i\phi} \end{pmatrix}, \tag{2.20}$$

where the diagonals, $e^{i\phi}$, represent the phase delay.

Direction-independent corruptions such as the antenna gain ($\mathbf{G}$) and bandpass ($\mathbf{B}$) can be represented in similar matrices:

$$\mathbf{G} = \begin{pmatrix} g_a(t) & 0 \\ 0 & g_b(t) \end{pmatrix}, \qquad \mathbf{B} = \begin{pmatrix} b_a(\nu) & 0 \\ 0 & b_b(\nu) \end{pmatrix}. \tag{2.21}$$

Here, both diagonal terms in the $\mathbf{G}$ matrix are time-dependent, with $a$ and $b$ denoting two different antenna feeds. For the $\mathbf{B}$ matrix, the diagonals $b(\nu)$ represent the frequency-dependent complex gains for antenna feeds $a$ and $b$.

For multiple discrete sources, the direction-independent (grouped together and represented as $\mathbf{G}$ in Equation 2.22) and direction-dependent ($\mathbf{E}$) effects can be incorporated into the visibility equation (Smirnov, 2011a):

$$V_{pq} = \mathbf{G}_p \Big(\sum_s \mathbf{E}_{sp} \mathbf{X}_{spq} \mathbf{E}_{sq}^H\Big) \mathbf{G}_q^H. \tag{2.22}$$

Direction dependent errors include corruptions that vary depending on the source position. A good example of such an error is the primary beam response of the telescope which varies

across the instrument's field of view (E.B. Formalont, 1999). This causes the amplitude of signals received to depend on their position relative to the centre of the beam.

These direction-dependent variations become particularly important when imaging with a wide field of view (when $w > 0$). To compute the total visibility measured by an interferometer, the brightness from all directions must be considered. If the sky plane is used and we consider effects on the $w$-direction as direction-dependent effects, we obtain the full sky RIME:

$$V_{pq} = \mathbf{G}_p \left( \iint_{lm} \mathcal{B}_{pq} e^{-2\pi i(u_{pq}l + v_{pq}m)} dl dm \right) \mathbf{G}_q^H. \tag{2.23}$$

When contrasted with the van Cittert-Zernike theorem (see Equation 2.8), which describes a set of visibilities measured under ideal conditions, without any corrupting effects, the full-sky RIME accounts for these effects, providing a more comprehensive model that includes the full 3D sky brightness distribution.

### 2.1.6 Radio frequency interference

Radio frequency interference (RFI) refers to unwanted radio signals unintentionally captured by radio telescopes. Sources of strong radio signals such as satellites, communication devices and aeroplanes can obscure or drown out faint celestial signals; complicating the data calibration procedure.

RFI is particularly problematic as it can distort the measured data, leading to inaccuracies. The effects of RFI can manifest as artefacts or erroneous features in the final radio image. RFI can vary with time and frequency, necessitating thorough detection and mitigation strategies during data collection and processing. As a result, identifying and removing RFI is crucial for ensuring the integrity of the data.

When data exhibits the corrupting effects of RFI, it is generally discarded. This data has to be excluded from the data used to make a radio image; a procedure known as flagging. Multiple stages of the calibration procedure implement various RFI flagging

strategies to ensure that as much bad data as possible is removed before making an image or performing analyses.

## 2.2 Calibration and imaging

The goal of calibration is to correct for effects that the instruments or local conditions, e.g. weather conditions, may have on observations. The data collected by an interferometer is referred to as *observed* visibilities and the main goal of the calibration procedure is to establish the relationship between the observed, $V'_{pq}$, and true, $V_{pq}$, visibilities. Certain steps in the calibration procedure solve for terms in the RIME so that this relationship can be obtained (E.B. Formalont, 1999).

Calibration can be split into three main stages:

1. First Generation Calibration (1GC),
2. Second Generation Calibration (2GC),
3. Third Generation Calibration (3GC)

The first two stages are direction independent, while the third is direction dependent. The majority of the calibration section of this thesis will focus on the first two stages of calibration and the analysis of the products. A short section is dedicated to a 3GC strategy called source peeling.

### 2.2.1 Structure of a measurement set

The collected visibilities from interferometers are commonly stored in a table format known as a measurement set (MS). The MS is a database used to record radio data in a manner that allows the data to be calibrated (Sault and Cornwell, 1999). An MS consists of a main table containing the visibilities and sub-tables containing the auxiliary metadata about the observation. The raw or unprocessed data is stored in the `DATA` column and, after calibration, the calibrated data is stored in the `CORRECTED_DATA` column (Bean *et al.*, 2022).

### 2.2.2 First generation calibration

1GC involves using known sources to solve for the Jones matrices in the RIME (Equation 2.23). During an observation, known sources called calibrators are observed at intervals alongside the target of interest. Calibrators are typically carefully chosen point sources that are simple, isolated objects with a known, constant flux density, polarization, and absolute position. These sources are used for calibration because they provide a straightforward signal for which the interferometer response is well-understood. It is assumed that calibrations performed near in time and position on the sky are applicable to the target field (E.B. Formalont, 1999). This process is also known as cross-calibration, as the calibrations are transferred from the calibrator sources to the target field. The main corrupting factors accounted for during 1GC are the delay (K), gain (G), and bandpass (B).

Delay calibration corrects for phase delays caused by the separation of antennas (geometric delay), electronic delay and delays caused by the observing conditions. The geometric delay can be accurately determined but the other effects leave residual delay errors. Delay calibration corrects for the remaining errors (E.B. Formalont, 1999, Clarke, 1999). These delays are frequency-dependent and are represented by the K-Jones matrix (Equation 2.20).

Gain calibration involves correcting for the time-dependent antenna gains. The antenna gains can be affected by atmospheric and environmental conditions, causing fluctuations in the amplitude and phase. The phase is typically worse affected by the observing conditions and antenna electronics than the amplitude component (E.B. Formalont, 1999). As a result, the gain calibrator source needs to be observed at intervals throughout an observation. The complex gain term is described by the G-Jones matrix (Equation 2.21).

Bandpass calibration corrects for the frequency-dependent corruptions arising from the environment or the antenna electronics (E.B. Formalont, 1999). The bandpass calibrator is typically observed once or twice during an observation as this term has no significant time dependence. The bandpass calibrator is a source whose frequency spectrum is known

over the observing frequency band (Bean *et al.*, 2022). These effects are represented by the B-Jones matrix (Equation 2.21).

Different calibrators are used for various calibrations since some quantities vary more rapidly with time and others with frequency. For example, the gain phase varies with time and needs to be observed multiple times during an observation to ensure accurate calibration, while the bandpass varies with frequency and only needs to be observed once per observation.

Another important factor corrected during 1GC is the flux scaling. The correlator of an interferometer processes only the relative signal strength and phase received from the electronics system. Therefore, the correlator products must be adjusted to represent the actual flux density measured from the sky visibilities (E.B. Formalont, 1999). During the calibration procedure, the visibilities are rescaled using a flux density calibrator with a known flux density in the observing frequency band. Other visibilities within the same observation, using the same setup, can be adjusted using the relative scale and the absolute flux density of the calibrator.

### 2.2.3 Imaging

The 1GC-corrected visibilities can be imaged using software such as WSClean (Offringa *et al.*, 2014) or CASA using the tclean task (Bean *et al.*, 2022). After 1GC, there are often residual corrupting effects left over in the data. These manifest as artefacts when the data is imaged and can be minimised through additional calibration. An example of a 1GC image and the corresponding PSF are presented in Figure 2.3. The radiating spikes in the image are called artefacts and occur as a result of residual effects of the PSF.

The observed visibility and sky brightness are Fourier transform pairs (see Equation 2.10). Imaging software attempts to Fourier transform the corrected visibilities to produce a dirty image then iteratively removes the effects of the PSF using deconvolution. There are many different deconvolution algorithms available; the Högbom CLEAN algorithm (Högbom, 1974) and Cotton-Schwab algorithm (Schwab, 1984) are incorporated into both tclean

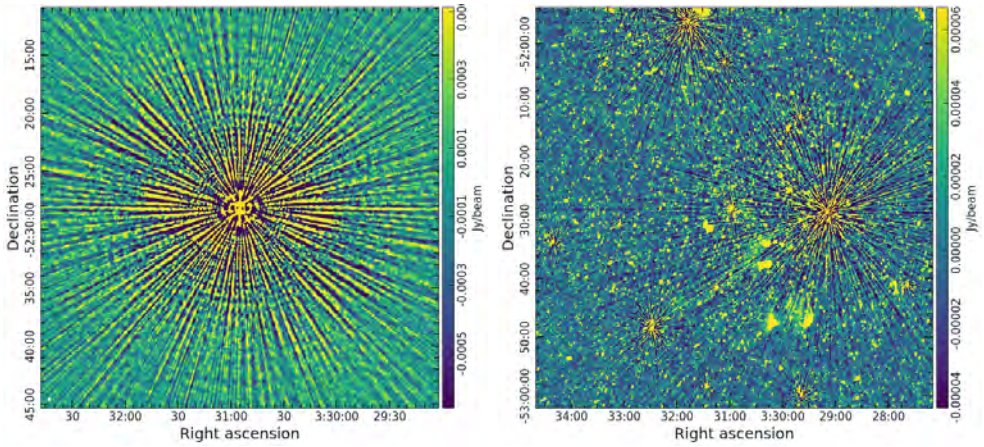


**Figure 2.3:** Example of a PSF (*left*) and associated 1GC image (*right*). Artefacts resembling the PSF are visible around the bright sources in the 1GC image.

and WSClean. The Högbom CLEAN algorithm operates by iteratively removing the PSF from the dirty image by finding and subtracting the brightest pixels in the image (Högbom, 1974). The Cotton-Schwab CLEAN algorithm is a more advanced variant of the Högbom CLEAN algorithm that alternates between deconvolution in the image space $(l, m)$ and refinement in the visibility space $(u, v)$ in a set of major and minor loops (Schwab, 1984). Both softwares also have a wide-band imaging options for high resolution and sensitivity. The imaging process is an integral part of 2GC and 3GC.

When imaging, the weight assigned to different spatial frequencies in the *uv*-plane determines which spatial scales dominate in the image. Large-scale structures are captured by shorter baselines, while smaller-scale structures are captured by longer baselines. The *uv*-plane is not always uniformly sampled, a core-heavy array typically oversamples the shorter baselines. To address this, weighting schemes are applied to modify the sampling function, $S$, which reflects the density of *uv*-samples. Three commonly used weighting schemes in tclean and WSClean are natural, uniform, and Briggs' weighting schemes (Briggs, 1995).

Natural weighting assigns equal weight to each visibility. This maximizes sensitivity, particularly for isolated point sources, but results in a sampling function that is "heavy" at the center of the *uv*-plane. Consequently, the PSF becomes larger with significant sidelobes, which can limit the ability to clean the image effectively, especially for complex

structures.

Uniform weighting normalizes the weights by the sampling density in the $uv$-plane, making the sampling function more uniform. This reduces the size of the PSF and suppresses sidelobes, enabling higher resolution imaging. However, the sensitivity to larger structures is reduced, as the short baselines are downweighted.

Briggs' weighting offers a compromise between natural and uniform weighting schemes. A robustness parameter, typically ranging from $-2$ to $+2$, allows tuning between the two extremes. Lower values produce weights closer to uniform weighting while higher values favor natural weighting (Briggs, 1995).

### 2.2.4 Second generation calibration

2GC is the process of calibrating the target against itself, commonly referred to as self calibration (T.J. Cornwell, 1999). The 1GC target data is used iteratively to improve calibration and reduce artefacts in the resulting image. This process requires two types of software: imaging software, such as WSClean, and calibration software, such as CASA (Bean *et al.*, 2022), CubiCal (Kenyon *et al.*, 2018) or QuartiCal (Kenyon *et al.*, 2023). The imaging software converts the corrected visibilities into an image, while the calibration software performs deconvolution to remove the remaining effects of the PSF (Smirnov, 2011b). The self calibration process is illustrated in Figure 2.4.

The procedure starts with a cross-calibrated image containing artefacts. This image is deconvolved, typically to a shallow flux threshold or with a limited number of CLEAN iterations. If explicit masking is used, tools such as `breizorro`[1] can be used to generate a mask from this image. A sky model is constructed by populating the `MODEL_DATA` column of the measurement set with the Fourier transform of the model image from the previous imaging step. The sky model is then calibrated against the observed data, and antenna gain solutions are derived. Using these updated calibration solutions, the data is re-imaged and deconvolved to a deeper threshold, incorporating the mask generated

[1] https://github.com/ratt-ru/breizorro

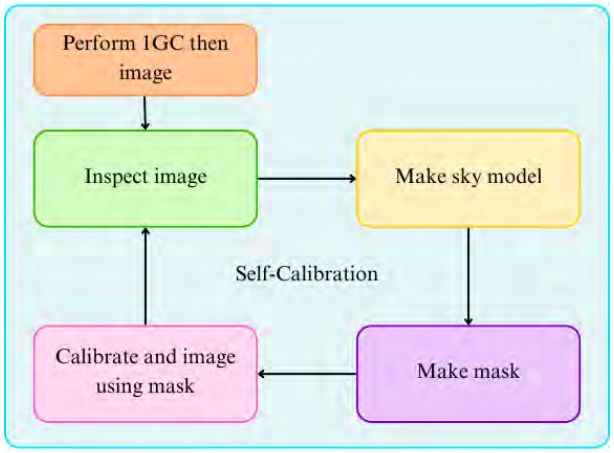


**Figure 2.4:** Summary of the self calibration procedure.

earlier. This process is repeated, iteratively improving the image. The stopping criterion for self calibration is usually when the improvement in the image becomes minimal or when the residuals—the difference between the observed visibilities and the modelled visibilities—reach a desired threshold based on the noise in the image.

When performing self calibration, the $G$ matrix, representing the complex gains of the antennas (see Equation 2.21), is iteratively refined to correct both phase and amplitude errors. Typically, gain phase corrections are applied first, as amplitude self calibration carries a higher risk of altering source characteristics and introducing artefacts.

### 2.2.5 Third generation calibration

3GC, also known as direction-dependent calibration, is the last stage of calibration where direction-dependent solutions are calculated and applied to the data. In Section 2.2.2, the assumption that calibrations performed near in time and position on the sky are applicable to the target field was made. This assumption does not hold for sources toward the edge of the field, particularly for very bright sources. Very bright sources that are not correctly modelled can cause severe artefacts in the image. 3GC aims to calculate solutions in the direction of the problematic source and apply them in order to reduce artefacts in the image.

Two different strategies for 3GC are source peeling (e.g. Noordam, 2004, Intema *et al.*,

2009) and faceting Cornwell and Perley, 1992, Smirnov, 2011b. Source peeling involves removing a problematic source by subtracting it from the corrected visibilities after calculating solutions to the RIME in the direction of the source, while faceting uses software to divide the image into facets and calculate different solutions for each facet. In this study, we attempt source peeling for each of our cluster fields.

### 2.2.6 Pipelines

Each stage of the calibration process used to be performed by hand but with the advancements in telescopes leading to large volumes of data being collected, treating each dataset by hand becomes too time consuming and often is not reproducible. To solve this problem, pipelines were created. A pipeline employs various software in an automated manner to perform calibration. Pipelines are usually telescope-specific and make use of software tailored for certain instruments. Examples include the VLA calibration and imaging pipeline (Bean *et al.*, 2022) developed for the JVLA, SPAM (Intema *et al.*, 2009) developed for the Giant Metrewave Radio Telescope (Swarup, 1990), and oxkat (Heywood, 2020) and the Containerized Automated Radio Astronomy Calibration (CARACal) pipeline (Józsa *et al.*, 2020) which were developed for the MeerKAT. The VLA pipeline makes use of CASA exclusively while SPAM employs the Astronomical Image Processing System (AIPS; Bridle and Greisen, 1994) and oxkat and CARACal use a variety of software.

## 2.3 Observations

We make use of data from multiple observations and different telescopes in order to study the radio environment and dynamics of three galaxy clusters: ACT-CL J0034+0225, ACT-CL J0137-0827 and ACT-CL J0330-5228 (hereafter J0034, J0137, and J0330 respectively). These clusters were all detected through their SZ-signal by the Atacama Cosmology Telescope during the ACTpol survey (Datta *et al.*, 2018, Hilton *et al.*, 2021) and are part of the MERGHERS survey (Knowles *et al.*, 2016, Knowles *et al.*, 2021, Knowles, 2024). The J0034 (Knowles *et al.*, 2016) and J0137 (Sikhosana, 2017) clusters have candidate

or confirmed detections of a diffuse radio halo, while J0330 is a likely candidate to host diffuse emission. The cluster properties, as published in the ACTpol DR5 catalogue, are summarised in Table 2.1.

| Name (ACT-CL) | $RA_{J2000}$ (deg) | $DEC_{J2000}$ (deg) | Redshift | Redshift Type | $M_{500cCal}$ ($10^{14}$ $M_\odot$) | $M_{200m}$ ($10^{14}$ $M_\odot$) |
|---|---|---|---|---|---|---|
| J0034.5+0225 | 8.62505 | +2.42285 | 0.388 | Spec | 8.12323 | 10.54492 |
| J0137.4-0827 | 24.35266 | -8.46097 | 0.56868 | Spec | 8.7926 | 11.08068 |
| J0330.9-5228 | 52.72849 | -52.4698 | 0.4417 | Spec | 5.813 | 7.39984 |

**Table 2.1:** Summary of the cluster properties from the ACTpol DR5 catalogue (Hilton *et al.*, 2021). All three clusters have spectroscopic (spec) redshifts. We make use of these properties for the analyses detailed in Chapter 4.

Data from the JVLA and MeerKAT instruments are calibrated and imaged in this study. This section provides background information on the telescopes and observations. We make use of the VLA Calibration and Imaging Pipeline and the CARACal Pipeline to streamline our data reduction.

### 2.3.1 JVLA data

The Karl G. Jansky Very Large Array (JVLA) is a radio interferometer situated in the United States. The JVLA comprises 28 25-metre antennas configured in a Y-shaped array (Thompson *et al.*, 1980, Perley *et al.*, 2011). Each leg of the array stretches approximately 21 kilometres. All of the antennas are mounted on railroad tracks, so that the radius and density of the array can be arranged to adjust the balance between angular resolution and sensitivity. The antennas can be arranged in four configurations, designated A through D. The longest baselines are achieved using configuration A while the shortest are achieved using configuration D. The frequency coverage of the VLA spans from 1.0 GHz to 50 GHz (Perley *et al.*, 2011).

The B configuration has a maximum baseline length of 11.4 km and provides a combination of long baselines, useful for resolving small scale objects, and short baselines, useful for detecting large scale structures (Perley *et al.*, 2011). This configuration provides a good trade-off between resolution and sensitivity for studying diffuse emission in galaxy clusters.

We calibrate and image four observations conducted using the JVLA between the 4th and 17th of May 2019 in the L-band (1.08 GHz − 2.03 GHz) in B-configuration. This configuration was used as it allows for the detection of large-scale diffuse objects while still achieving high resolution. Three of the observations are dedicated to J0034 and one to J0137 with a total of ∼3 hours and 30 minutes on source for J0034 and 30 minutes for J0137. The frequency band is split into 16 unique spectral windows and 1 unique polarization setup. The observing setup includes 1024 channels with a channel width of 1000 kHz and a 3 s integration time. The properties of the VLA calibrators[2] observed are summarised in Table 2.2.

| Name | RA (J2000) | DEC (J2000) | $S_{1.5\text{GHz}}$ (Jy) | $\Delta S$ (Jy) | Calibrator type |
|---|---|---|---|---|---|
| 3C48 | 01:37:41 | +33:09:35 | 16.50 | <0.495 | Bandpass, flux |
| 3C138 | 05:21:09 | +16:38:22 | 8.47 | >0.254 | Polarisation |
| 0059+001cal | 00:59:05 | +00:06:52 | 2.50 | <0.075 | Amplitude, phase |

**Table 2.2:** Summary of VLA calibrator properties. All three calibrators were used for both J0034 and J0137 observations.

### 2.3.2 MeerKAT data

The MeerKAT telescope is a radio interferometer located in the Northern Cape province of South Africa (Jonas and MeerKAT Team, 2016). The MeerKAT telescope is composed of 64 offset Gregorian antennas, each with a diameter of 13.5 m. Each antenna has three receivers, allowing for three separate observing bands, the UHF-, L- and S-band with central frequencies of approximately 800 MHz, 1.2 GHz and 2.6 GHz respectively. All observing bands have up to 4096 channels with varying channel widths.

The array is laid out in a "core-heavy" configuration. A dense inner region with a radius of about 1 km hosts 70% of the antennas forming many short baselines. The outer region contains 30% of the the antennas, forming longer baselines with a maximum of 7.7 km. This configuration makes it ideal for observing diffuse emission hosted by galaxy clusters. With most baselines being relatively short, this instrument is well-suited for resolving

[2] https://science.nrao.edu/facilities/vla/observing/callist

large scale structures, such as diffuse, low surface brightness emission. The remaining antennas form the longer baselines which are used to resolve small, compact sources with high resolution.

We make use of L-band and UHF-band MeerKAT data observed as part of the MERGHERS pilot, tier 1, and tier 2 surveys (Knowles *et al.*, 2016, Knowles *et al.*, 2021, Knowles, 2024). The MeerKAT data for J0137 was pre-processed with the CARACal pipeline as part of the MERGHERS tier 1 data release (Knowles, 2024). We make use of the 2GC data to re-image the cluster for this study. A summary of the MeerKAT observations is presented in Table 2.3.

| Field | | J0034 | J0137 | J0330 |
|---|---|---|---|---|
| Observation | Central freq (MHz) | 1160 | 1284 | 816 |
| | Bandwidth (MHz) | 524 | 856 | 544 |
| | Channels | 2511 | 1024 | 4096 |
| | Channel width (kHz) | 209 | 836 | 132 |
| | Dump time (s) | 2 | 4 | 2 |
| | Total time (hrs) | 0.67 | 2 | 2 |
| 2GC Image | $B_{\rm Maj}$ ($''$) | 10.4 | 9.4 | 14.5 |
| | $B_{\rm Min}$ ($''$) | 7.6 | 7.5 | 10.2 |
| | PA (deg) | -44.9 | -37.8 | -19.4 |
| | $\sigma_{\rm rms}$ (μJy) | 24.4 | 7.9 | 14.3 |
| | Target data flagged (%) | 42.8 | 50.7 | 31.5 |

**Table 2.3:** Summary of MeerKAT observations and 2GC image parameters for each field.

| Name | RA (J2000) | DEC (J2000) | $S_{1.4\rm GHz}$ (Jy) | $\Delta S$ (Jy) | $\alpha$ | $\Delta\alpha$ | Calibrator Type |
|---|---|---|---|---|---|---|---|
| J0022+0014 | 00:22:25 | +00:14:56 | 2.90 | 0.07 | -0.56 | 0.02 | Amplitude, phase |
| J0210-5101 | 02:10:46 | -51.01.02 | 3.40 | 0.07 | 0.13 | 0.02 | Amplitude, phase |
| J0303-6211 | 03:03:51 | -62:11:26 | 3.19 | 0.07 | -0.09 | 0.01 | Amplitude, phase |
| J0408-6545 | 04:08:20 | -65:45:09 | 15.20 | 0.34 | -1.20 | 0.00 | Bandpass, flux |

**Table 2.4:** Summary of MeerKAT calibrator properties. The amplitude/phase calibrators in the order listed correspond to J0034, J0137, and J0330, respectively. All three observations make use of the same bandpass/flux calibrator.

## 2.4 Data processing

### 2.4.1 The VLA calibration and imaging pipeline

1GC and 2GC are performed using the VLA Calibration and Imaging Pipeline[3]. The pipeline makes use of CASA to implement 1GC and 2GC in an automated manner (Bean *et al.*, 2022). The data products produced include 1GC and 2GC calibrated images along with a multitude of diagnostic plots. The default pipeline script[4] is used with minor alterations to limit the graphical user interface (GUI) dependence allowing the pipeline to be run in the background.

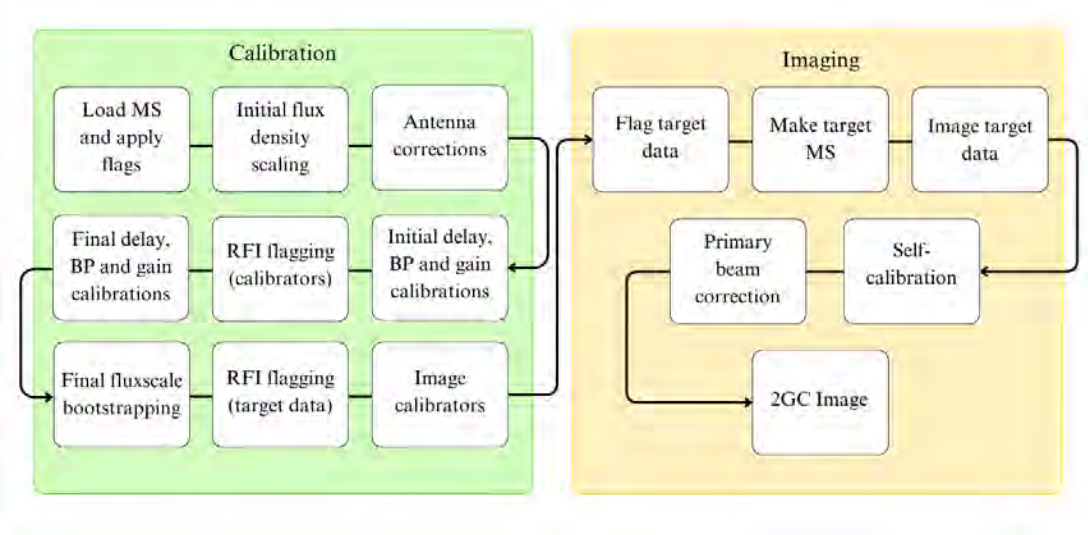


**Figure 2.5:** General steps in the calibration process using the VLA Calibration and imaging pipeline.

Figure 2.5 gives a brief overview of the calibration and imaging process using the pipeline. The MS is loaded and preliminary corrections are applied. This step includes the application of Hanning smoothing and online flags generated during the observation, as well as antenna position corrections. As the JVLA antennas are movable, the exact positions of the antennas need to be measured in order to correctly correlate signals received by the antennas.

[3] https://science.nrao.edu/facilities/vla/data-processing/pipeline

[4] https://science.nrao.edu/facilities/vla/data-processing/pipeline#section-9

The initial flux density calibrator model is then prepared. The flux density of a primary calibrator source is assumed to be known and is compared to the observations of the calibrator in order to determine the antenna gains. Pre-determined calibrations such as antenna position corrections, gain curves, and atmospheric opacity corrections are also applied at this stage. The final flux density scaling is determined and applied at a later stage.

Next, the initial delay, bandpass, and gain calibrations are iteratively determined by solving for the corresponding Jones matrices, as described by Equations 2.20 and 2.21 presented in Subsection 2.2.2. Automated flagging of RFI is then performed on the calibrator data with the initial calibrations applied. This stage uses the CASA `RFLAG` and `TFCROP` algorithms to detect and flag anomalous data in the frequency and time domains. Documented sources of RFI affecting the observing frequency band are also flagged out at this stage. In all of our JVLA datasets there is residual RFI corrupting the data. The pipeline uses quality assessment scores at each stage to indicate whether the stage was successful, assigning a score from 0 to 1 to the data products where a score of 1 indicates that the stage was performed successfully. At this stage our datasets received scores of $\sim 1.0$, however, upon inspecting the diagnostic plots, such as the amplitude versus frequency plot, there are frequencies at which the amplitude is multiple orders of magnitude higher. This remaining RFI is removed through manual flagging, whereby the CASA task `plotMS` is used to visualise the data and the anomalous data is flagged by hand using `flagdata`. Much of the data flagged manually lies in the frequency range $\sim 1000 - 1100$ and $\sim 1500 - 1600$, likely caused by aircraft navigation and Global Positioning System (GPS) signals[5].

After flagging, the final delay, bandpass, and gain calibrations ($\mathbf{K}$, $\mathbf{B}$, and $\mathbf{G}$ matrices in the RIME, Equation 2.23) are determined and applied to the data. The final flux scaling is also determined at this stage and applied. The corrections made to the bandpass, delay and gain terms of the RIME are stored in calibration tables which are then applied to the `DATA` column and written to the `CORRECTED_DATA` column.

[5] https://science.nrao.edu/facilities/vla/docs/manuals/obsguide/rfi

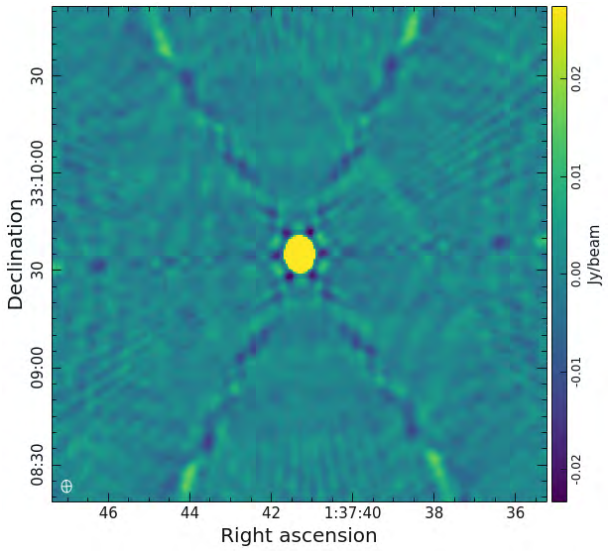


**Figure 2.6:** An example of a calibrator source image from the VLA Calibration and Imaging Pipeline. The bright source seen here is 3C48, the primary flux calibrator for the J0034 and J0137 observations.

The target scans are then flagged for known sources of RFI and the calibrations are applied to the target data. At this stage, the target data is also flagged manually using the same method as with the calibrators. Again, much of the RFI is likely caused by aircraft navigation and GPS signals. In the last stage of the calibration pipeline, the calibrators are imaged for diagnostic purposes. The calibrators should appear as point-like sources in these images, Figure 2.6 shows an example image of one of our calibrators post-1GC. The restoring beam of this image is $3.86'' \times 3.12''$ causing the source to appear slightly oval-shaped. This can occur if the array has more antennas distributed along one axis causing the uv-coverage to be more extensive along that direction. The striping in this image is the leftover effects of the JVLA PSF. The calibrator images produced after 1GC are shallow, performing only two short rounds of deconvolution, this is enough to inspect the structure of the source but not enough to remove the effects of the PSF entirely.

The imaging part of the pipeline makes use of the products from the calibration stage. The 1GC-calibrated target data is split off into a separate MS and imaged. The pipeline uses CASA's native imager, TCLEAN, to image the target, apply primary beam correction, and perform 2GC or self calibration. Primary beam correction ensures that sources across the image have accurate flux density values, as the primary beam response becomes less

reliable toward the edges of the image. These stages are described in more detail on the VLA Calibration and Imaging Pipeline website.

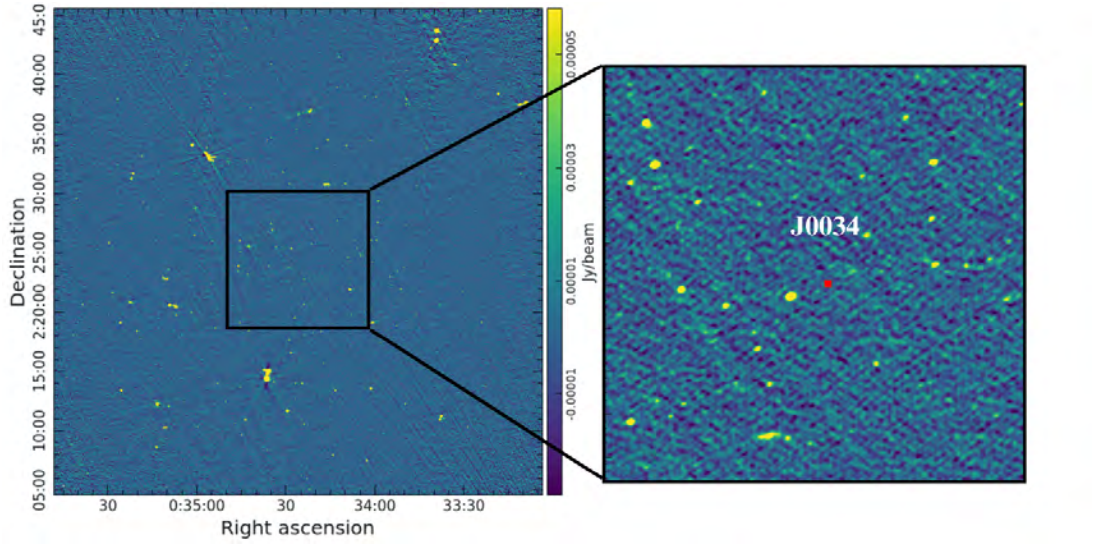


**(a)** JVLA 2GC image of the J0034 field with a close-up of the cluster. The RMS noise in the image is $\sigma \approx 9.5$ $\mu$Jy/beam and the SZ peak is indicated as a red point.

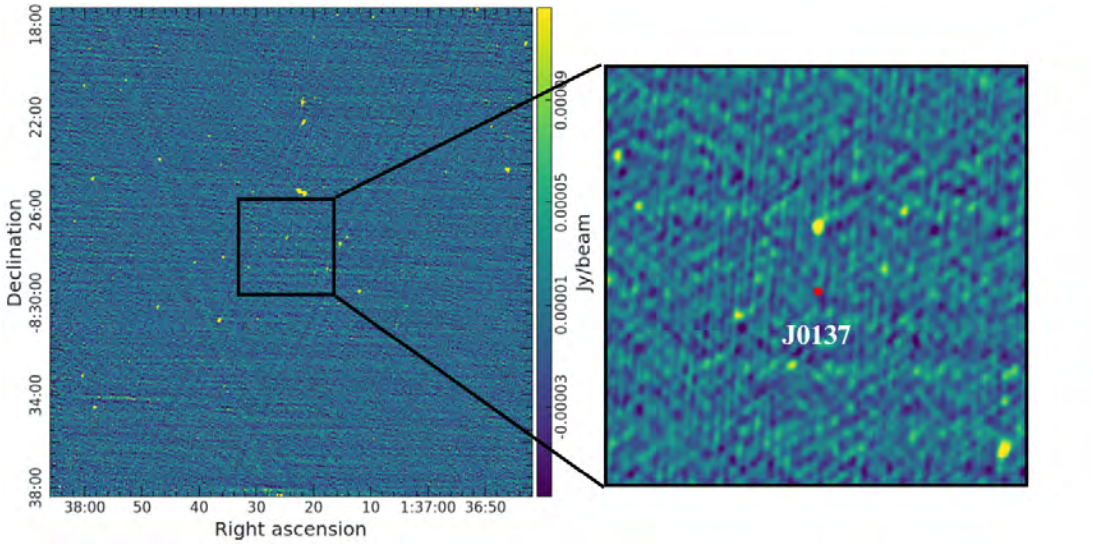


**(b)** JVLA 2GC image of the J0137 field with a close-up of the cluster. The RMS noise in the image is $\sigma \approx 30$ $\mu$Jy/beam and the SZ peak is indicated as a red point.

**Figure 2.7:** Self-calibrated, primary beam corrected JVLA 2GC images of the J0034 and J0137 fields at 1.5195 GHz. The colour scales of each full image and inset are matched.

In the case of J0034, we calibrate each observation separately using the calibration pipeline and combine the calibrated data when imaging. The final images we present in Figures 2.7a and 2.7b are created using WSClean and the primary beam corrections applied

manually using python. This choice was made due to the computational efficiency of the WSClean algorithm. The native CASA imaging algorithm requires long computation times. We make use of multiscale cleaning in both images, using the default scale settings to recover emission on a range of spatial scales. We apply multifrequency synthesis cleaning by enabling channel joining and fitting a second-order polynomial to model spectral variations across the frequency range. However, multifrequency weighting is disabled. This means that while the spectral structure is accounted for, the weighting scheme does not fully optimize sensitivity across all frequencies. This ensures that the image is not biased towards the higher-frequency channels, which could dominate the weighting scheme and artificially sharpen the image. The properties of the 2GC-calibrated JVLA images are summarised in Table 2.5.

| Field | $\nu$ (GHz) | $B_{maj}$ ($''$) | $B_{min}$ ($''$) | PA (deg) | $\sigma_{rms}$ ($\mu$Jy) |
|---|---|---|---|---|---|
| J0034 | 1.5195 | 3.8 | 2.8 | -69.7 | 10.3 |
| J0137 | 1.5195 | 3.8 | 2.9 | -13.9 | 29.9 |

**Table 2.5:** Properties of the 2GC-calibrated JVLA images. The resolution is given as the major and minor axes of the restoring beam, the frequency is the central frequency and $\sigma_{rms}$ is the RMS noise.

Artefacts are visible around the bright sources in each of the cluster fields after the 2GC stage of the pipeline. We follow the procedure outlined in the CASA Self Calibration Tutorial to perform two additional rounds of self calibration outside of the pipeline. Specifically, we perform two rounds of phase-only self calibration; making use of WSClean. Both images still show significant artefacts around the bright sources in the field, particularly those toward the outskirts of the image. For this reason, we attempt to remove the sources using the source peeling procedure described in Section 2.4.3.

### 2.4.2 The CARACal pipeline

The CARACal pipeline (Józsa *et al.*, 2020) is used to calibrate all of the MeerKAT data used in this study. The pipeline makes use of software such as CASA (Bean *et al.*, 2022), WSClean (Offringa *et al.*, 2014), CubiCal (Kenyon *et al.*, 2018), and DDFacet (Tasse

*et al.*, 2023) to automate the process of 1GC, 2GC and 3GC. CARACAL is operated using a configuration file or YAML file that provides a set of instructions for the calibration and imaging procedures. Each step of the process is contained within a worker and each worker can make use of various software. All of the YAML files used to calibrate our MeerKAT data are adaptations of the default MeerKAT continuum YAML [6] supplied with CARACAL.

The calibration procedure using CARACAL is very similar to the procedure used in the VLA Calibration and Imaging pipeline. The first stage of the calibration procedure involves importing the data; the calibrators and target are also split into separate measurement sets at this stage. The calibrator MS is then flagged for common sources of RFI. A flagging mask is used to exclude all channels within the MeerKAT observing band known to be affected by RFI. We make use of the MeerKAT RFI[7] flagging mask for both J0034 and J0330.

Additional RFI flagging strategies are used to get rid of residual RFI in the calibrator data that is not removed by the MeerKAT RFI mask. We make use of a combination of the AOFlagger (Offringa *et al.*, 2010) and Tricolour (Hugo *et al.*, 2022) algorithms with the Khruschev and first pass QUV flagging mask strategies, respectively, for J0034. When used together, these algorithms effectively removed RFI without over-flagging the calibrator data. It is important that the calibrator data is not over-flagged as this is the data used to calculate the calibration solutions. The Tricolour flagger with a variant of the Khruschev masking strategy, tailored to the UHF-band, developed by Trehaeven (2022) is used for J0330. This strategy was chosen because the original Khruschev strategy was too harsh, flagging more than 80% of the calibrator data.

1GC is then performed, applying the calibration solutions from the observed calibrator sources listed in Table 2.4 to the targets. There is an inspection step after 1GC which provides diagnostic plots that can be used to assess the data quality after 1GC and

[6] https://github.com/caracal-pipeline/caracal/blob/master/caracal/sample_configurations/meerkat-continuum-defaults.yml

[7] All flagging masks are available at https://github.com/caracal-pipeline/caracal/blob/master/caracal/data/meerkat_files/

flagging. We make use of the plots to ensure that the data is not over- or under-flagged when testing various flagging strategies. In cases where the flagging strategy is too harsh (flagging more than 70% of the data), or when RFI is still present in the data, the flags are reset and another flagging strategy is tested.

The target MS is also flagged for known RFI using the same standard MeerKAT RFI mask from the 1GC stage. Additional flagging is performed using a combination of AOflagger with the first pass QUV strategy and Tricolour with the Gorbachev masking stretegy for J0034. The tricolour flagger with the Gorbachev mask alone is used for J0330. We follow the same procedure as with the calibrators, inspecting the diagnostic plots to ensure that the target data is not over-flagged.

Phase-only 2GC is then performed for 2 iterations, this step makes use of WSClean and CubiCal to implement the 2GC procedure described in Section 2.2.4. The resulting 2GC images are presented in Figure 2.8 and their properties are summarised in Table 2.3. We present the full-field images in Appendix A.

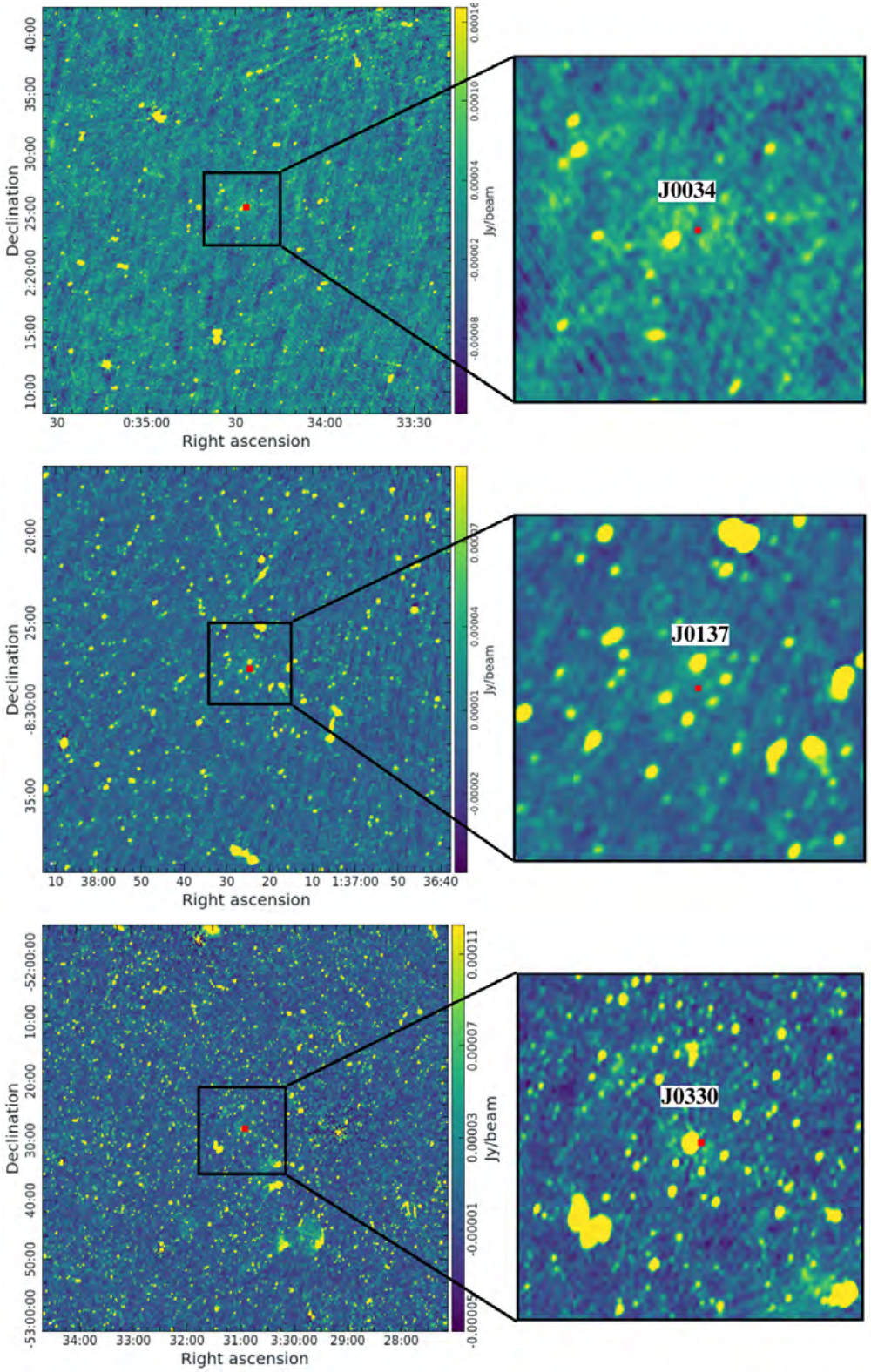


**Figure 2.8:** MeerKAT 2GC images of J0034 (*top*), J0137 (*middle*), and J0330 (*bottom*). The images show the clusters with their respective SZ peaks indicated in red.

In all three images, there are artefacts visible around the brighter sources, especially those toward the edge of the field. Some sources are far enough from the centre of the field that the artefacts have no effect on the target, while sources closer to the target cause visible striping even at the centre of the image. We attempt direction dependent calibration methods to reduce the effects of these sources on the final images.

### 2.4.3 Direction dependent calibration

We attempt a method of direction dependent calibration called source peeling for all three datasets. A combination of the calibration software, QuartiCal, and imaging software, WSClean, are used to attempt source peeling. Bright sources near the centre of the field displaying artefacts are selected from the 2GC image source list and predicted into individual source model columns in the measurement set using the software package Crystalball[8]. These models are then subtracted from the corrected visibilities using QuartiCal. During the subtraction, calibration solutions are derived in the direction of each problematic source. When performed successfully, direction dependent calibration can reduce artefacts around bright, problematic sources that may be affecting the target. The reduction of these artefacts can in turn reduce the noise in the image, boosting the signal of fainter objects in the field. In our case, we see little to no improvement after attempting source peeling.

In the MeerKAT and JVLA data, bright complex sources can be seen in the J0034 and J0137 fields. These sources all display extended emission and thus were challenging to peel. Most peeling software make use of single component models to represent sources in an image. The structure and emission of a point source can be captured completely using this method of modelling but this is not always the case for more complicated sources. For complex sources, accurate modelling requires detailed information about the extended emission, which may require multiple Gaussian components or more sophisticated shapes. If the model is incomplete or oversimplified, the subtraction will fail to fully remove the source, leaving residuals that can affect the rest of the image. An example of a

[8] https://github.com/caracal-pipeline/crystalball

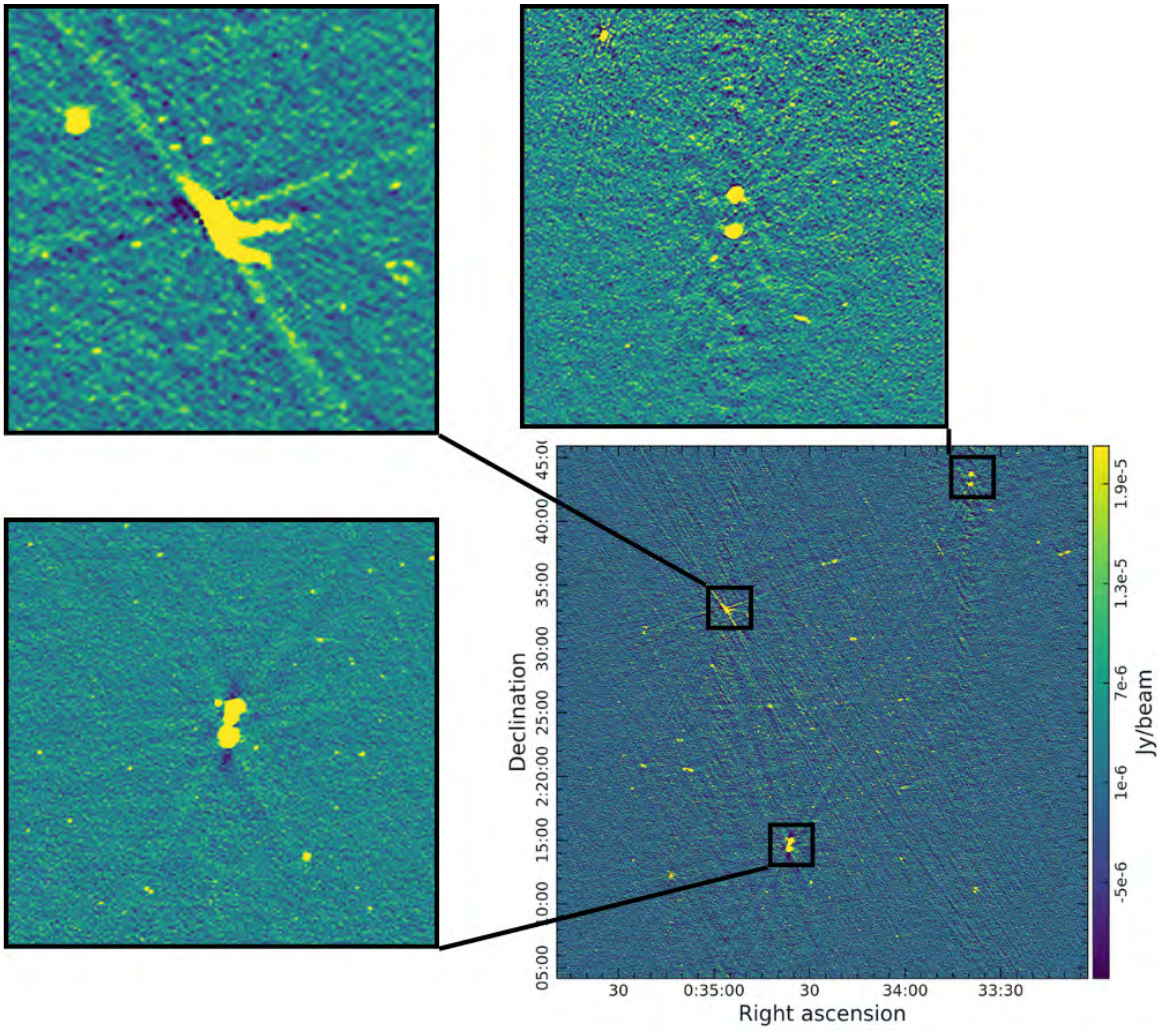


**Figure 2.9:** Examples of complex sources in the J0034 field causing artefacts to appear across the image. Despite their positions, some artefacts from these sources are visible even at the centre of the image.

failed peeling attempt can be seen in Figure 2.10. Remnants of the double lobed source can be seen in the image as well as areas of over-subtraction. Another factor affecting these images is the order of calibration. Performing source peeling after self-calibration can leave residual artefacts, even after the problematic source has been removed. In this case, performing peeling between the 1GC and 2GC stages might have reduced the severity of these artefacts. However, due to the nature of the sources, their effects would likely not have been entirely eliminated. Complex, extended sources such as these may require higher frequency-resolution modelling in order to better account for frequency-dependent effects. In our case, the data are divided into 8 frequency bins, providing a

balance between accurate frequency modelling and computational efficiency. However, more detailed frequency models could be obtained by increasing the number of frequency bins—e.g. to 16 or more—though this comes at the cost of increased computational demands and longer processing times. As our peeling strategy was unable to remove the effects of the bright sources, we use the 2GC images in all of the post-processing procedures.

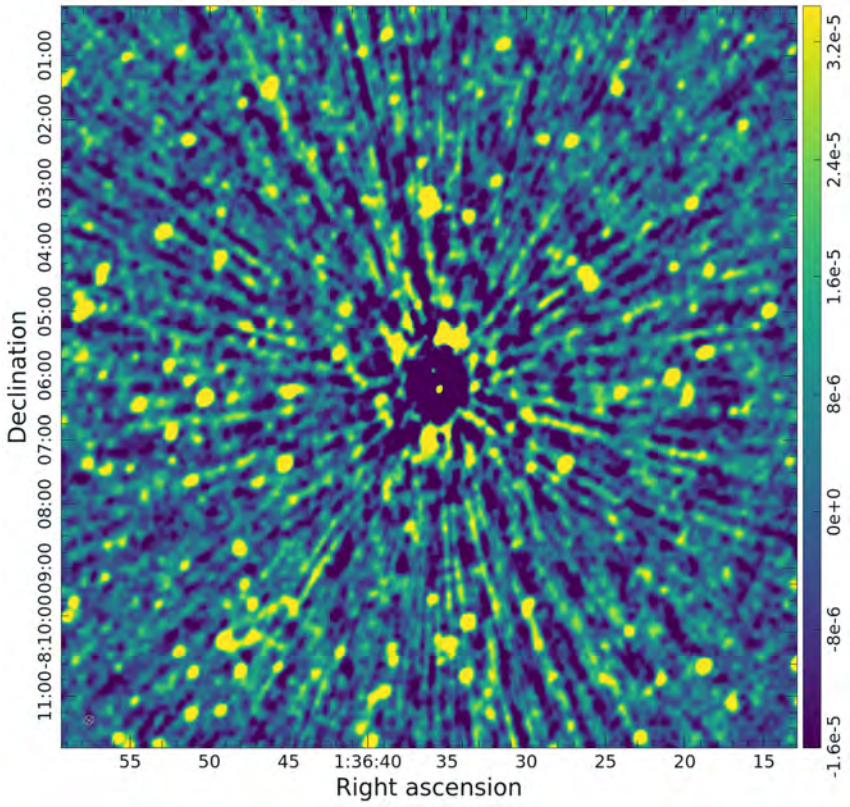


**Figure 2.10:** Example of a failed source peeling attempt. A double lobed source in the J0137 field was unsuccessfully peeled from the image, leaving behind residual source flux in some areas and over-subtracting in others.

We attempted facet-based calibration (Cornwell and Perley, 1992) methods similar to those performed by Trehaeven (2022), where the image is broken up into smaller polyhedral facets in order to correct for direction dependent errors. This procedure is attempted using the imaging software DDFacet (Tasse *et al.*, 2023), and calibration software KillMS (Tasse, 2023). However these attempts were unsuccessful and we were unable to match the quality of the 2GC images. A comparison of the failed DDFacet image and the 2GC WSClean image for J0034 can be seen in Figure 2.11.

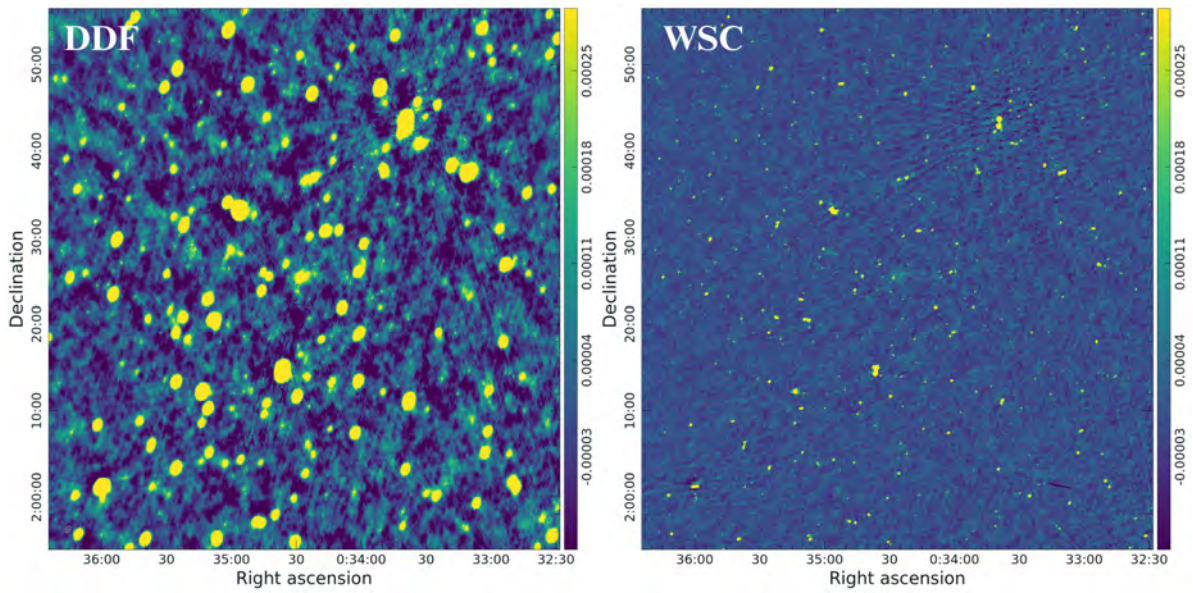


**Figure 2.11:** Comparison of a failed DDFacet image and WSClean image for the J0034 field.

### 2.4.4 Primary beam correction

Before conducting any investigations using the radio images, we perform primary beam correction on the MeerKAT images using the package KATBEAM[9] and on the JVLA images using python to multiply the images by a function with documented JVLA coefficients[10]. The images produced are masked such that they only display regions where the primary beam response is above 30 percent of the value at the phase centre.

## 2.5 Image verification

In order to verify the astrometry and fluxscale of our images, we need to compare with source catalogues from published sky surveys. Given the frequencies and sky coverage of our observations, we use the low and mid-frequency Rapid ASKAP Continuum Surveys (RACS; McConnell *et al.*, 2020, Hale *et al.*, 2021). To generate source catalogues from our images and the RACS images, we use the Python Blob Detection and Source Finder (PyBDSF; Mohan and Rafferty, 2015). PyBDSF searches for localized regions of ele-

[9] https://github.com/ska-sa/katbeam
[10] http://www.aips.nrao.edu/cgi-bin/ZXHLP2.PL?PBCOR

vated intensity above a certain threshold which are considered as candidate sources. The module attempts to fit models consisting of one or more elliptical Gaussians to the detected sources. Single-Gaussian sources are given the label 'S' if they are the only source on an island, those sharing an island are labelled 'C', and sources composed of two or more Gaussians are labelled 'M'. To ensure that only compact, isolated sources are used for the checks, we select S-labelled sources only.

As we only need to catalogue the brightest compact sources for our image verification steps, we use a pixel threshold of $8\sigma_{img}$, with source boundaries defined by an island threshold of $5\sigma_{img}$, where $\sigma_{img}$ is the local image rms determined by PyBDSF. The resulting catalogues contain the positions of the detected sources, their characterisations, integrated flux density measurements and peak flux density measurements.

### 2.5.1 Astrometry checks

All three cluster fields are checked for astrometric accuracy using Topcat (Taylor, 2011). The PyBDSF catalogues for each cluster field are cross-matched with sources in the SIMBAD astronomical database (Wenger *et al.*, 2000), which contains source information from surveys such as NVSS (Condon *et al.*, 1993, 1998), GLEAM (Hurley-Walker *et al.*, 2017b), and FIRST (Becker *et al.*, 1995). These surveys all have varying resolutions; to ensure that there is no source confusion due to different beam sizes, we select isolated sources from our catalogues to perform the cross-match. Sources are considered isolated if there are no other sources within a $60''$ radius. We chose to cross-match against SIMBAD rather than a single radio survey as this approach provides a better statistical sample ($\gtrsim 10$ sources in each field except J0137 JVLA). The crossmatch is performed using the Topcat sky crossmatch function providing an average angular offset between identified sources and their counterparts. A search radius of $4.0''$ is chosen as it provides a balanced compromise between minimizing spurious detections and maximizing true source detections. This radius is sufficiently large to account for positional inaccuracies between catalogues while remaining small enough to reduce the likelihood of incorrectly matching unrelated sources. The plots in Figures 2.12 and 2.13 show the positional offset of sources in each cluster field

for the JVLA and MeerKAT data respectively. The astrometric cross-match is plotted to show the distribution of right ascension and declination offsets.

For the sources in the J0034 JVLA and MeerKAT images, the mean offset is relatively small ($\lesssim 0.2''$ in both directions). J0330 has a slightly higher mean offset of $-0.3''$ in the declination. These offsets are comparable to the pixel size in each image and are therefore not corrected.

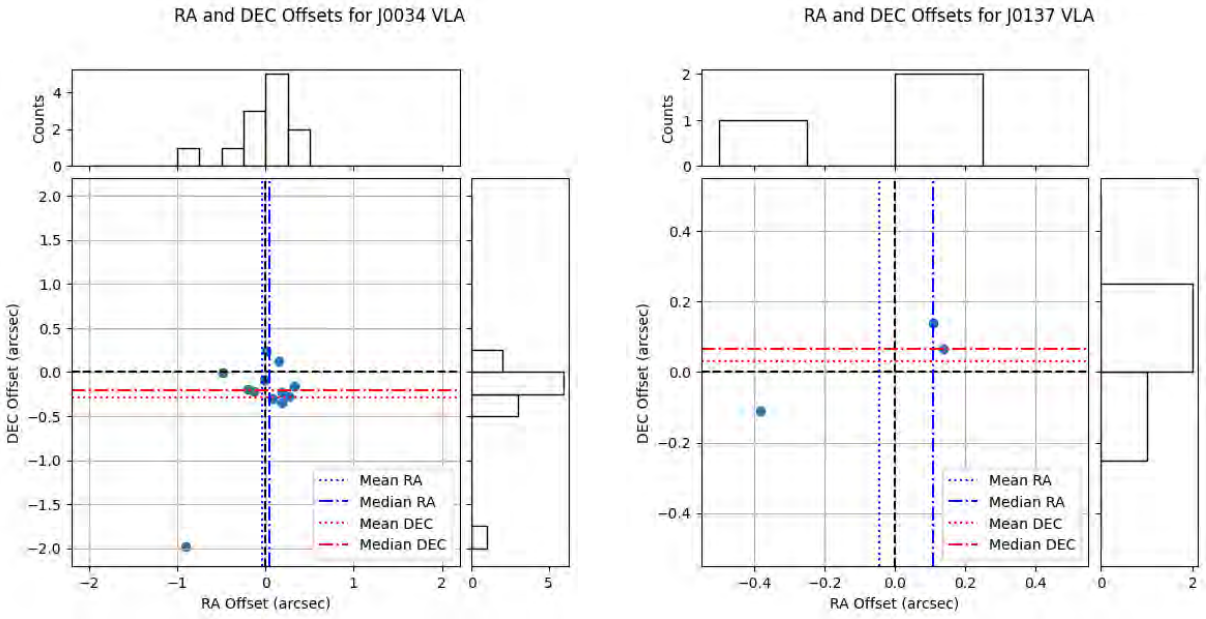


**Figure 2.12:** Astrometric checks for JVLA images.

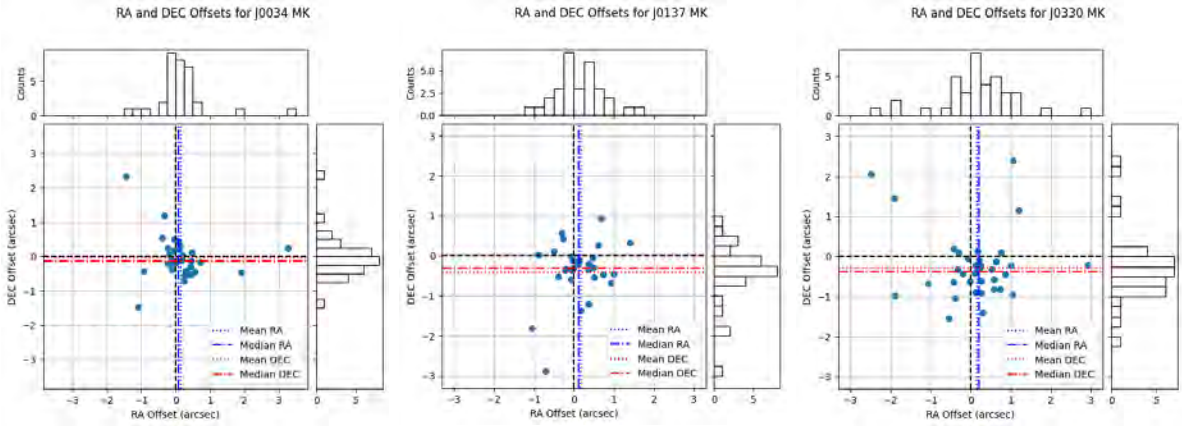


**Figure 2.13:** Astrometry check for MeerKAT images.

### 2.5.2 Flux density checks

In order to check the fluxscale of our final images, we compare our source flux densities against those in the RACS low images and published catalogue (888 MHz) which have a resolution of 25″ (Hale *et al.*, 2021). The JVLA and MeerKAT images are first convolved to the same beam size as the RACS images using the task IMSMOOTH in CASA. Our JVLA and MeerKAT images both have much higher resolutions than the RACS low images, $\sim 4''$ and $\sim 10 - 14''$ respectively; convolving the images to the same beam size ensures that the level of source blending is the same across all of the images. We then generate catalogues for the convolved images and RACS images. These catalogues are crossmatched using the sky match function in TOPCAT. Sources appearing in both images are added to a new catalogue along with their corresponding total (integrated) flux densities. The RACS flux densities are scaled to the same reference frequency as the JVLA (1.5195 GHz) and MeerKAT sources (1.284 GHz), for comparison. We assume a power law of the form $S_\nu \propto \nu^\alpha$ and a fiducial spectral index of $\alpha = -0.7$ (Smolčić *et al.*, 2017).

The scaled RACS fluxes and JVLA or MeerKAT fluxes are related by the power law:

$$S_{\text{Scaled}} = \kappa (S_{\text{JVLA/MK}})^\gamma \tag{2.24}$$

where values of 1 for $\kappa$ and $\gamma$ indicate an exact match between the two sets of flux densities (Knowles *et al.*, 2022). Equation 2.24 is linearised by taking the logarithm of both sides and the values of $\kappa$ and $\gamma$ are fitted using a linear regression.

We find that the flux plots for J0034 and J0137 (see Figures B.1-B.2 in Appendix B) show a high degree of scatter. Upon closer inspection, the RACS low images for these fields are affected by RFI and artefacts produced by bright sources in the field (see Figure 2.14 for an example). This may be the cause of the scatter in the fit plots and high errors for the fit parameters (see Table B.1 in Appendix B). It is common practice to make use of the published RACS low catalogue to perform these checks. However, despite the

visible RFI, we achieved the same (or slightly better depending on the field) fit parameters when generating our own catalogues from the RACS low images rather than the published catalogue. The published catalogue also makes use of PyBDSF but with lower pixel and island thresholds (3 and 5$\sigma$ respectively), this may be the reason for the difference.

We investigate the available RACS mid images (1.368 GHz), which are closer in frequency to the L-band MeerKAT and JVLA images, and find these to be relatively artefact-free on visual inspection. RACS mid provides a more accurate comparison as the spectral index assumption has less of an effect on closely spaced frequencies. Additionally, the RACS mid images are closer in sensitivity and depth to the MeerKAT images. The only field which yields better results using the RACS low versus the RACS mid images, is J0330. This cluster was observed at UHF-band, and so is closer to RACS low in frequency than RACS mid. We present the results of the flux density checks in Figure 2.15 and Table 2.6.

The results for the J0034 and J0137 MeerKAT images show reasonably good fits when compared to RACS mid. The fit values, $\kappa$ and $\gamma$, all lie close to 1, indicating a good fit. This is not the case for the JVLA images, the fit parameters for both the J0034 and J0137 fields have high errors and deviate far from unity. In both JVLA versus RACS mid plots,

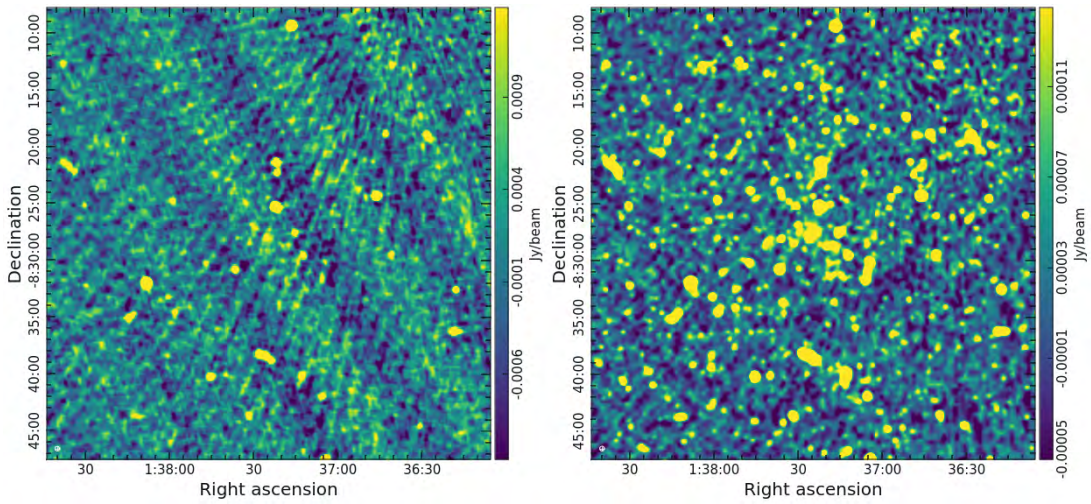


**Figure 2.14:** RACS low (*left*) and mid (*right*) images of J0137 used to perform the flux density check. Both images are centred on the cluster. Fringing is visible across the low frequency image. This is likely as a result of residual RFI detected on short baselines.

| Field | Images | $\kappa$ | $\Delta\kappa$ | $\gamma$ | $\Delta\gamma$ |
|---|---|---|---|---|---|
| J0034 | MK vs RACS mid | 0.99 | 0.19 | 0.98 | 0.04 |
| | VLA vs RACS mid | 0.66 | 0.51 | 0.79 | 0.13 |
| J0137 | MK vs RACS mid | 0.82 | 0.06 | 0.96 | 0.01 |
| | VLA vs RACS mid | 2.17 | 1.09 | 1.06 | 0.08 |
| J0330 | MK vs RACS mid | 0.69 | 0.27 | 0.86 | 0.07 |
| | MK vs RACS low | 0.95 | 0.10 | 0.99 | 0.02 |

**Table 2.6:** Fit parameters from the flux density checks.

there is a fair amount of scatter, which may be caused by differences in sensitivity coupled with poor flux calibrations around the bright sources in both fields. Sources affected by the artefacts emanating from the problematic sources in each field are found to have poor flux calibrations when compared with sources in artefact-free parts of the images.

In the case of J0330, the fit obtained when comparing to RACS low is far better than when comparing to RACS mid. This is likely due to errors relating to the assumed spectral index. The central UHF frequency, 802 MHz, is relatively far from the RACS mid frequency of 1.368 GHz. Sources with spectral indices that differ from the assumed $-0.7$ will have different scaled fluxes. For example, a 1.0 mJy source at the UHF frequency should have a scaled flux of 0.7 mJy at the RACS mid frequency using the $\alpha = -0.7$ assumption. A source with a spectral index of $-0.5$ would have a scaled flux of 0.8 mJy. For this reason, we assume the RACS low fit to be the more reliable fit of the two.

Based on the results of our image verification tests, the depth and sensitivity of the 2GC images, we choose to use the MeerKAT images to search for diffuse emission. The fluxscale uncertainties are not corrected in the images but are accounted for in the following chapter.

## 2.6 Summary

In this chapter, we discussed the fundamental concepts of radio astronomy and interferometry. The radio band provides a reliable window from which to view the cosmos. The use of interferometers enables high-resolution imaging across the radio band by combining signals from multiple antennas in an array. The RIME was introduced as a key framework that relates observed visibilities to the sky brightness distribution and the

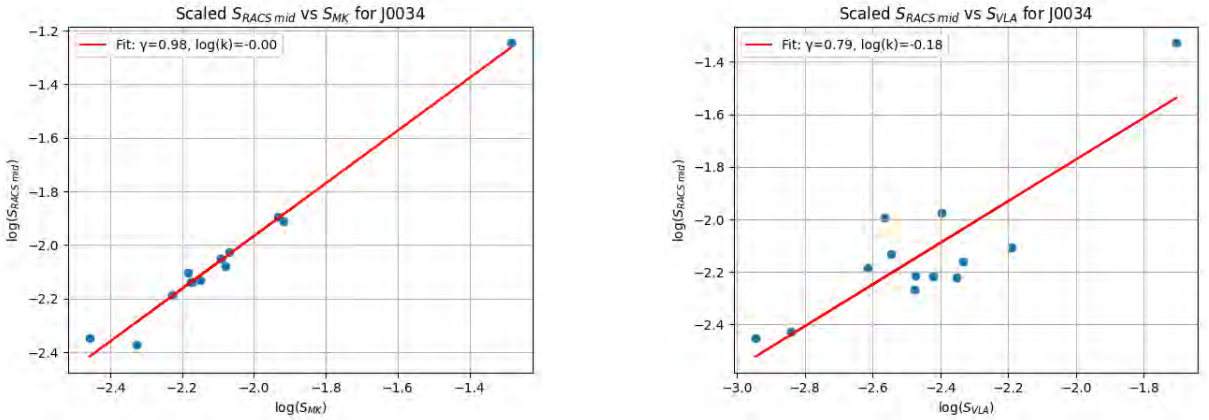


**(a)** *Left:* Regression plot for J0034$_{\mathrm{MK}}$ versus RACS mid. *Right:* Regression plot for J0034$_{\mathrm{JVLA}}$ versus RACS mid.

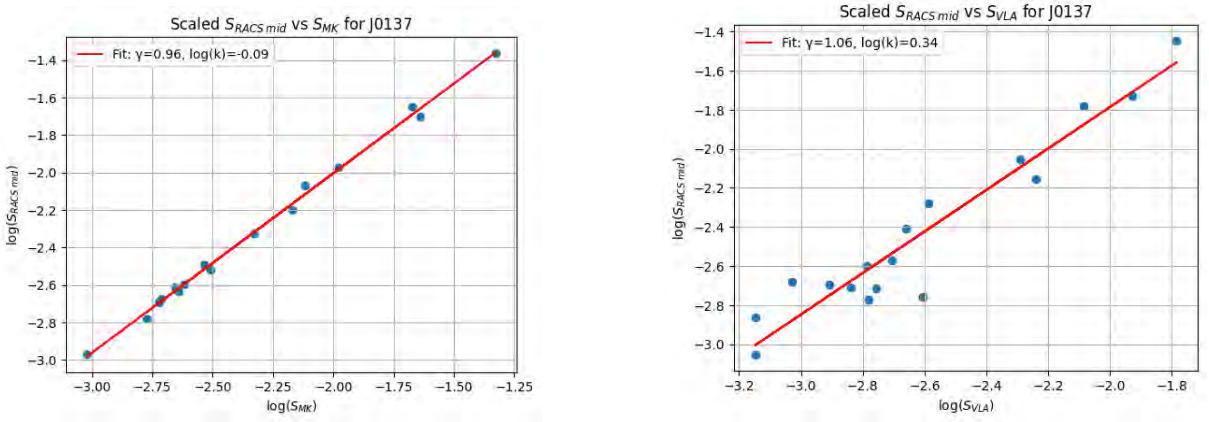


**(b)** *Left:* Regression plot for J0137$_{\mathrm{MK}}$ versus RACS mid. *Right:* Regression plot for J0137$_{\mathrm{JVLA}}$ versus RACS mid.

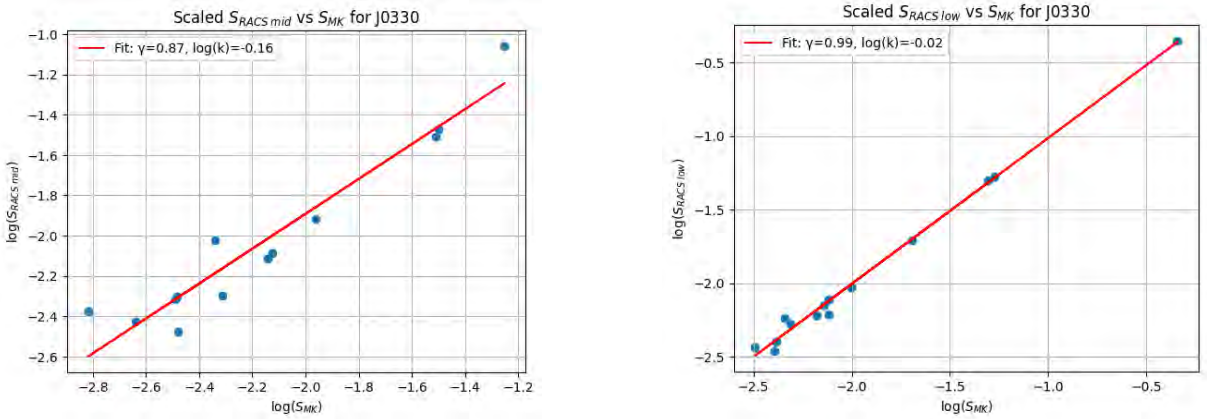


**(c)** *Left:* Regression plot for J0330 versus RACS mid and, *Right:* for RACS low.

**Figure 2.15:** Flux density checks for each cluster field versus RACS mid or low images.

corruptions that can occur along a signal's path. The three stages of calibration were discussed; highlighting their connection to the RIME. We outlined the imaging process, demonstrating how visibility data is transformed into interpretable images at each of the calibration stages. We introduced our observations and outlined how each dataset was calibrated with the use of pipelines and other software. Lastly, we presented our 2GC images and discussed image verification techniques. We find that the astrometric offsets in the JVLA and MeerKAT images are comparable to the pixel size of the images. The flux scale of sources in the MeerKAT images is consistent with that of the RACS images. However, the flux scale of the JVLA sources is impacted by artefacts in the images, leading to poor flux calibration for the affected sources.

# Chapter 3

# Searching for Diffuse Cluster Radio Emission

Here we present the results of our search for diffuse radio emission in our target clusters using the final 2GC images from Chapter 2. As these sources are expected to be faint and extended, we use several methods to improve our sensitivity to such structures, as well as remove compact source contributions, before analysing any detections.

## 3.1 Improving sensitivity to extended emission

We investigate the effect of varying the beam size on the 2GC MeerKAT images of each cluster field, specifically measuring the largest linear size of the emission within the $3\sigma$ contours. This approach aims to determine the extent to which different beam sizes can resolve the full extent of the diffuse emission. Given that cluster diffuse emissions, such as radio halos, are large-scale structures, smaller beams may only capture part of the emission, resulting in an artificially smaller apparent size or altered flux density measurements. By testing a range of beam sizes, we aim to identify an optimal balance between resolution and sensitivity for capturing the full structure of the emission. This method is used because it is a fast, computationally efficient method to explore a range of beam sizes without needing to re-image each field. This test is performed in preparation

for deeper analyses discussed in Section 3.1.2. Finding the resolution at which the images are most sensitive to diffuse emission is vital for these later analyses.

We use the task `imsmooth` in CASA to vary the beam size. The major and minor axes and position angle of the desired beam are specified; `imsmooth` then applies a Gaussian convolution. This convolution process spreads the flux from each pixel over neighbouring pixels, simulating a larger, lower-resolution beam than in the original image. We convolve each image to approximately two, three and four times the size of the 2GC beam and observe the effects on the shape and flux density of the emission before compact source removal. The resulting images are presented in Figure 3.1 and the emission properties in Table 3.1.

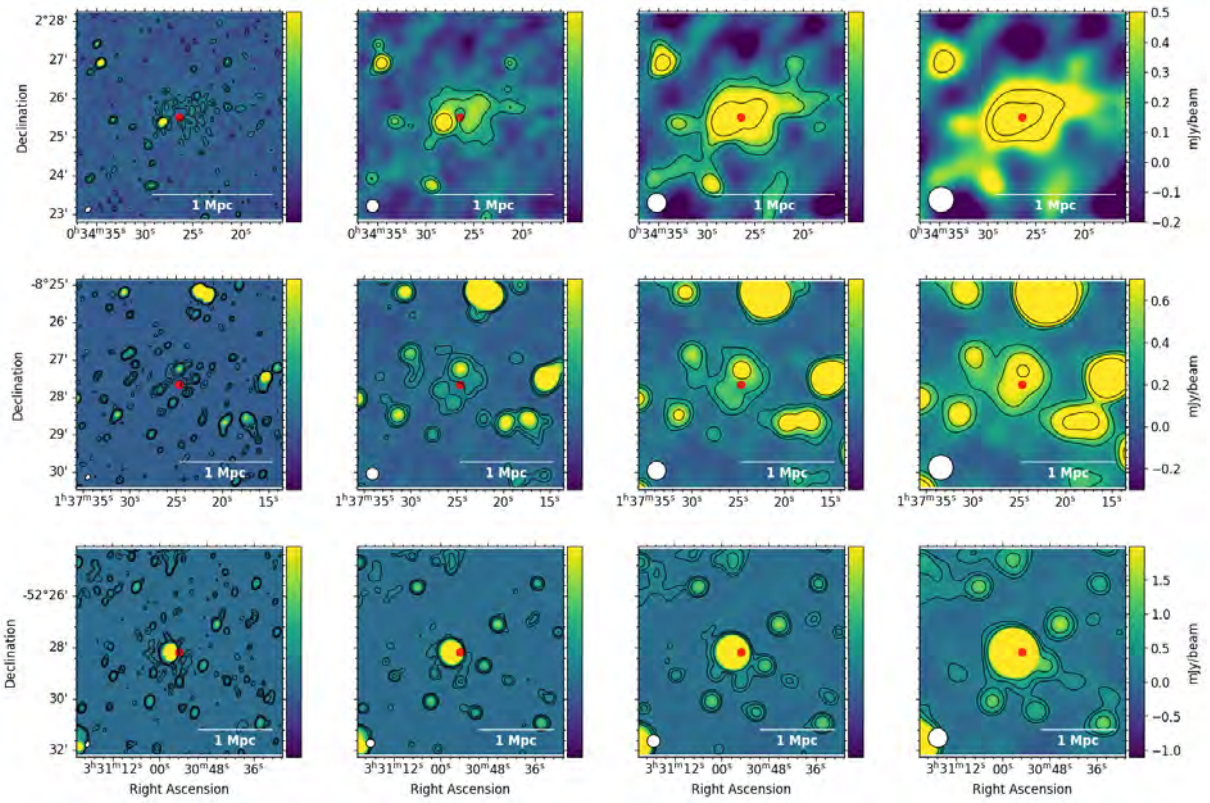


**Figure 3.1:** Images for each cluster field with varying beam size. The rows contain different cluster fields (J0034, J0137, and J0330, respectively) and columns various beam sizes. The first column contains the 2GC image for each field as a point of reference.

In all of the smoothed images, source blending is evident, with bright sources appearing larger and closer together. Sources that were initially close in the 2GC images appear

| Field | $B_{\mathrm{Maj}}$ ($''$) | $3\sigma$ Area ($''^2$) | LAS ($''$) | LLS (kpc) | $S_\nu$ (mJy) | $\Delta S_\nu$ (mJy) |
|---|---|---|---|---|---|---|
| J0034 | 2GC | 3156.5 | 99.9 | 532.0 | 3.96 | 0.15 |
| | 20 | 8410.9 | 115.0 | 612.0 | 6.21 | 0.29 |
| | 30 | 21162.2 | 132.5 | 705.2 | 9.60 | 0.56 |
| | 40 | 7673.6 | 133.8 | 712.4 | 5.13 | 0.37 |
| J0137 | 2GC | 1969.9 | 61.2 | 403.5 | 1.72 | 0.04 |
| | 20 | 15509.8 | 105.7 | 696.7 | 5.13 | 0.15 |
| | 30 | 44753.1 | 124.9 | 822.9 | 18.9 | 0.27 |
| | 40 | 11326.8 | 105.9 | 698.3 | 3.40 | 0.13 |

**Table 3.1:** Effect of varying the beam size on the integrated flux density and size of the J0034 and J0137 halos before source subtraction. The uncertainty in the flux density is the statistical uncertainty obtained when measuring the flux of the $3\sigma$ halo regions.

almost merged in the smoothed images.

The integrated flux density of the J0034 and J0137 emission, measured using the $3\sigma$ contours as a guide, increase drastically with beam size. This increase suggests that a fraction of the halos' emission exists on scales larger than the 2GC resolution. However, in both cases, when increased to a beam size of $40''$, the flux decreases, indicating that the beam size is too large, causing the emission to be diluted. Certain structures in the emission may be partially resolved out at the largest beam size, leading to incomplete sampling and reduced measured flux. For both structures, we also see an increase in the $3\sigma$ area when the beam size is increased to $30''$ and a decrease when further increasing the beam size. This indicates that $30''$ is the optimal beam size for both fields. The images used for further analyses are smoothed to $30''$ to ensure as much of the halo emission is uncovered as possible (at the cost of resolution).

In the J0330 images, increasing the beam size leads to the expected source blending; however, convolving the 2GC image does not reveal much unresolved diffuse emission in the cluster centre. There appears to be faint emission surrounding the central source but much of the emission is obscured by the sources surrounding the SZ peak. This suggests that the absence of detectable diffuse emission is not due to the beam size being too small. Further increasing the beam size can lead to blending with nearby sources, making it challenging to distinguish the emission from these blended sources.

### 3.1.1 Compact source removal

In order to inspect the diffuse emission alone, we create source subtracted images. This allows the fainter diffuse emission to be seen more clearly by removing bright compact sources from the field. We explore compact source removal both in the visibility $(u, v)$ plane and in the image $(l, m)$ plane, and compare the results.

For all three cluster fields, we use two different methods of visibility plane source subtraction. The first method makes use of the list of sources produced during the 2GC imaging procedure while the second makes use of an additional imaging step to produce a high-resolution point source model. We use filtering code developed by Rudnick (2002) and an inpainting[1] package to test image-based source subtraction. These methods are useful as the original visibility data is not always available. It is more common to find archived images as these require far less storage space. These subtraction methods provide an image-based alternative to the visibility space source subtraction methods.

#### 3.1.1.1 Visibility plane: 2GC source model

In this method, the source list generated during imaging after 2GC is used to predict the compact source information into a separate source-model column in the MS. The point source model is then subtracted in uv-space from the corrected visibilities, leaving behind only the diffuse emission and non-compact sources with complex morphologies. We use the CASA task `uvsub` to perform the subtraction. The column containing the subtracted visibilities is then re-imaged using the same imaging parameters as the 2GC image. This image is created to inspect for compact source contamination. If residual source data has not been fully subtracted, the remaining source information may cause artefacts in the image, or sources may still be partially visible.

After visually checking for point source contamination, we re-image the subtracted visibility column using parameters that further enhance the diffuse emission. Parameters such as the beam size and visibility weighting are adjusted to reduce sensitivity to small

[1] https://github.com/twillis449/radio_source_analysis.git

scales, decreasing the resolution but making the diffuse emission more visible. We test this method of subtraction as this procedure is more efficient than the second method presented. It requires one less imaging step, and the compact sources are reasonably well modelled in the 2GC source list, provided a good mask is used when making the 2GC image. The mask should accurately identify and exclude compact sources while preserving diffuse emission, avoiding over-masking that could lead to flux loss.

#### 3.1.1.2 Visibility plane: High-resolution source model

The second method we explore involves an additional imaging step to model the compact sources as accurately as possible. This technique is commonly used for compact source subtraction (for examples see Knowles *et al.*, 2016, Wilber *et al.*, 2018, Trehaeven *et al.*, 2023). The data is imaged using a uv-cut and taper, which depends on the angular size of the emission, and a robust value of $-1.0$. These parameters are chosen to boost the resolution of the image at the cost of sensitivity to large-scale structures. To ensure that none of the diffuse emission is subtracted, the angular size of the emission is measured and converted to uv-wavelengths using Equation 3.1:

$$\text{Angular size} \sim \frac{1}{\text{uv-wave}}, \tag{3.1}$$

where the angular size is measured in steradians and uv-wave is the distance measured in wavelengths.

The high-resolution (HR) image requires the data from the long baselines in the array to be dominant. To achieve this, we apply a uv-cut and taper so that only sources smaller than the measured diffuse emission are imaged. Figure 3.2 demonstrates how the uv-cut and taper functions of WSClean operate. To minimise the influence of shorter baselines (larger structures), the minuv-l and inner-Tukey taper are used. The Tukey taper is used to smooth the edges of the plot with a Tukey window or tapered cosine window. If a strict UV-cut is applied without tapering, the edges of the selected UV region could introduce artefacts such as ringing into the image. Tapering smooths the abrupt uv-cut

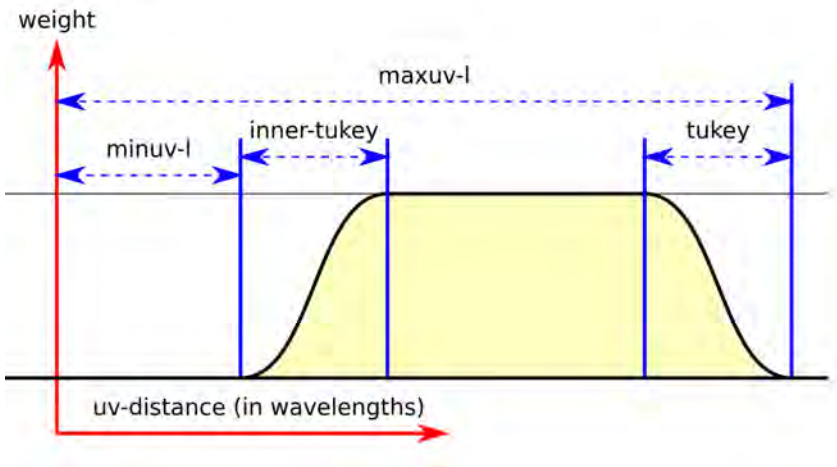


**Figure 3.2:** Plot showing how the Tukey taper can be used to influence the weights of the visibilities (Offringa *et al.*, 2014).

by gradually down-weighting the contribution from the undesired baselines, leading to a more artifact-free image.

#### 3.1.1.3 Image plane: Filtering

We apply the filtering method used by Knowles *et al.* (2021) to our images. This code employs a series of filters to separate large- and small-scale emission within an image. First, a minimum filter is applied over a box approximately three times the size of the beam's major axis, isolating the lowest intensity values in each region and effectively capturing the large-scale emission. A maximum filter is then applied to this result over the same box size, further smoothing the isolated large-scale structure by taking the maximum values from the previous step. Finally, the smoothed large-scale structure image is subtracted from the original image to isolate the small-scale structures, which correspond to compact sources or high-frequency features (Rudnick, 2002, Knowles *et al.*, 2021).

The large-scale image retains the same units and resolution as the original since no convolution occurs during the filtering process. However, the filtered images exhibit a negatively offset zero-level that requires correction. The large-scale filtered image represents only the lowest values within each region and does not fully capture the true intensity of the background emission. Instead, it creates an image that appears "flattened", resulting in an

artificial reduction in baseline intensity or an offset from the true zero level (Knowles *et al.*, 2021). This is corrected by measuring the noise in the low-pass filtered image and adding it back to the large-scale filtered image.

After the zero-level correction, the large-scale image is convolved to a larger beam size for aesthetics. We use this smoothed minimum-filtered image, containing only the large-scale emission, to generate contours for the diffuse emission in our clusters.

#### 3.1.1.4 Image plane: Inpainting

The inpainting package makes use of two main scripts: one script to perform morphological erosion and dilation in order to remove background sources from the image, and another to extract morphological parameters of selected galaxies in the image. The package builds on the technique described in Rudnick (2002). The technique makes use of mathematical morphology to remove compact sources from the image and fills in the values in these areas by inpainting values from the surrounding emission using Navier-Stokes inpainting or Fast Marching Method inpainting. This does pose a challenge when bright sources partially overlap with emission and there is a disjoint in the surrounding region providing information to the inpainting algorithm. Such an example is presented in the Bullet cluster inpainting tutorial (see Bullet cluster example). The code also has the option to exclude such regions in the inpainting step, leaving the subtracted region unfilled.

The most noticeable feature of the inpainted image is the appearance of the filled-in regions, where traces of the subtraction process remain visible. The algorithm used to fill in these subtracted areas is sensitive to local noise; any significant variation in noise causes the regions to be unevenly filled, resulting in inconsistencies in the reconstructed flux. This occurs because the algorithm relies on surrounding noise levels to inpaint the region. If one side of the region is near a noise peak, that portion will be filled with a higher flux density compared to the opposite side. An example of this effect is shown in Figure 3.3: region 'A' is adjacent to a noise peak, while region 'B' is at a noise minimum. Consequently, the filled region exhibits a disjoint, with one half containing higher flux values and the other lower flux values. Variations of the inpainting scripts can be used

to exclude extended structures that overlap with regions where the background changes drastically.

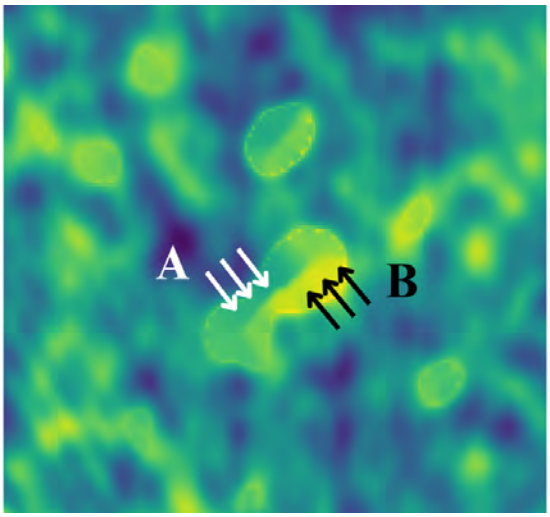


**Figure 3.3:** Example of an inpainted region affected by the local noise variations. One half of the region is filled in using the noise in region 'A' while the other half is filled in using the noise in region 'B', causing a disjoint in the filled region.

The inpainted images are generated using the original 2GC image. This means that the beam size and other image parameters are identical. We make use of `imsmooth` to convolve the inpainted image to a larger beam size to ensure most of the emission is resolved. The low-resolution (LR) inpainted images are affected by the bright edges as the smoothing process redistributes the flux from these edges.

### 3.1.2 Comparison of source subtraction methods

The source-subtracted, filtered, and inpainted images for each field are presented in Figures 3.4, 3.5, and 3.6. For each method, the 2GC image is shown alongside the point source subtracted full-resolution (PSSUB-FR) image—to assess compact source contamination, as well as the point source subtracted low-resolution (PSSUB-LR) or convolved image, which highlights the diffuse emission.

The 2GC model-subtraction method is successful for two of the three clusters (J0034 and J0137). In both cases, a visual inspection of the PSSUB-FR image indicates that the

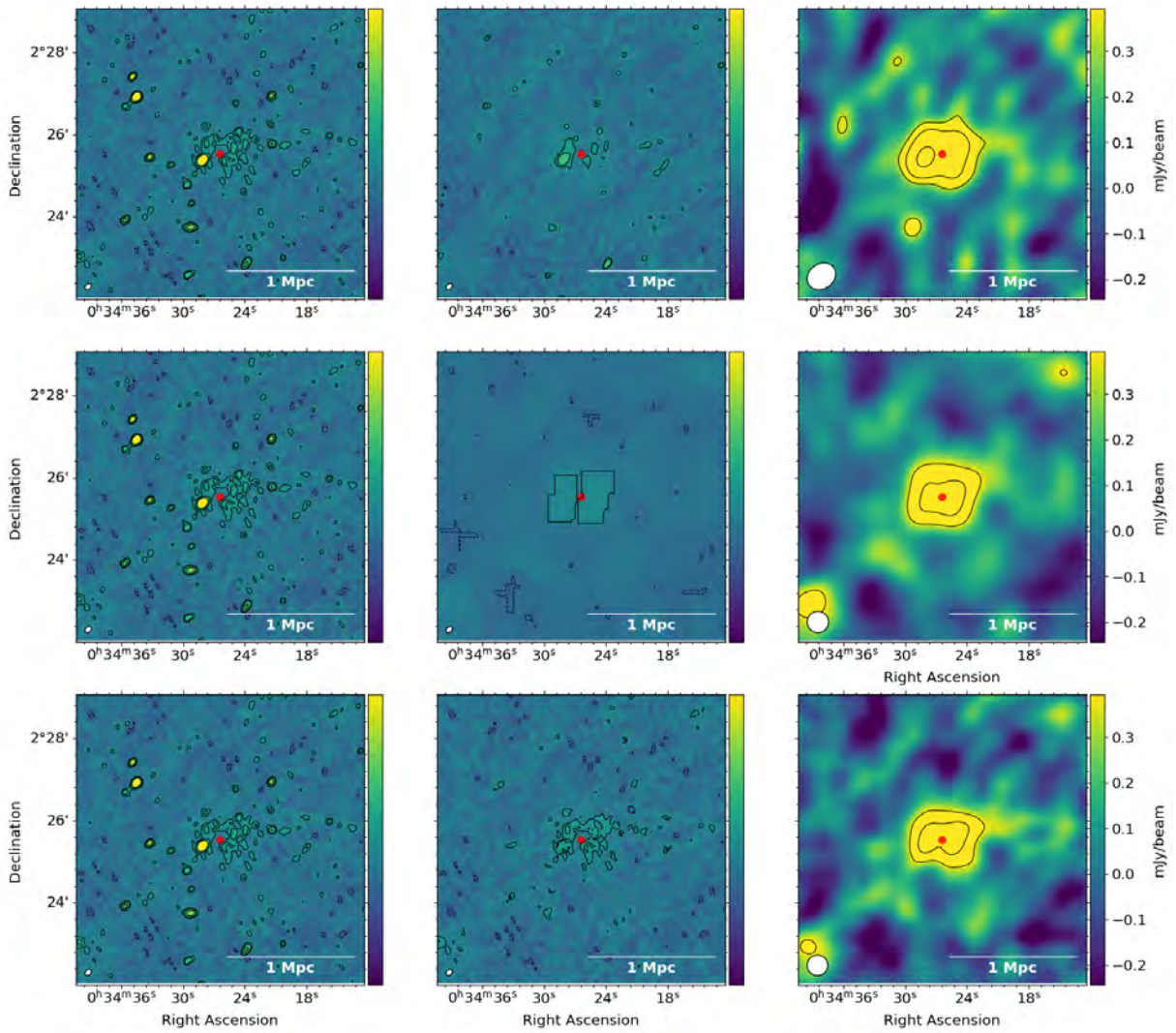


**Figure 3.4:** Comparison of source subtraction methods for J0034. Columns represent: (1) 2GC image, (2) PSSUB-FR image, and (3) PSSUB-LR image. Rows correspond to different subtraction techniques: 2GC model subtraction (*top*), filtering (*middle*), and inpainting (*bottom*).

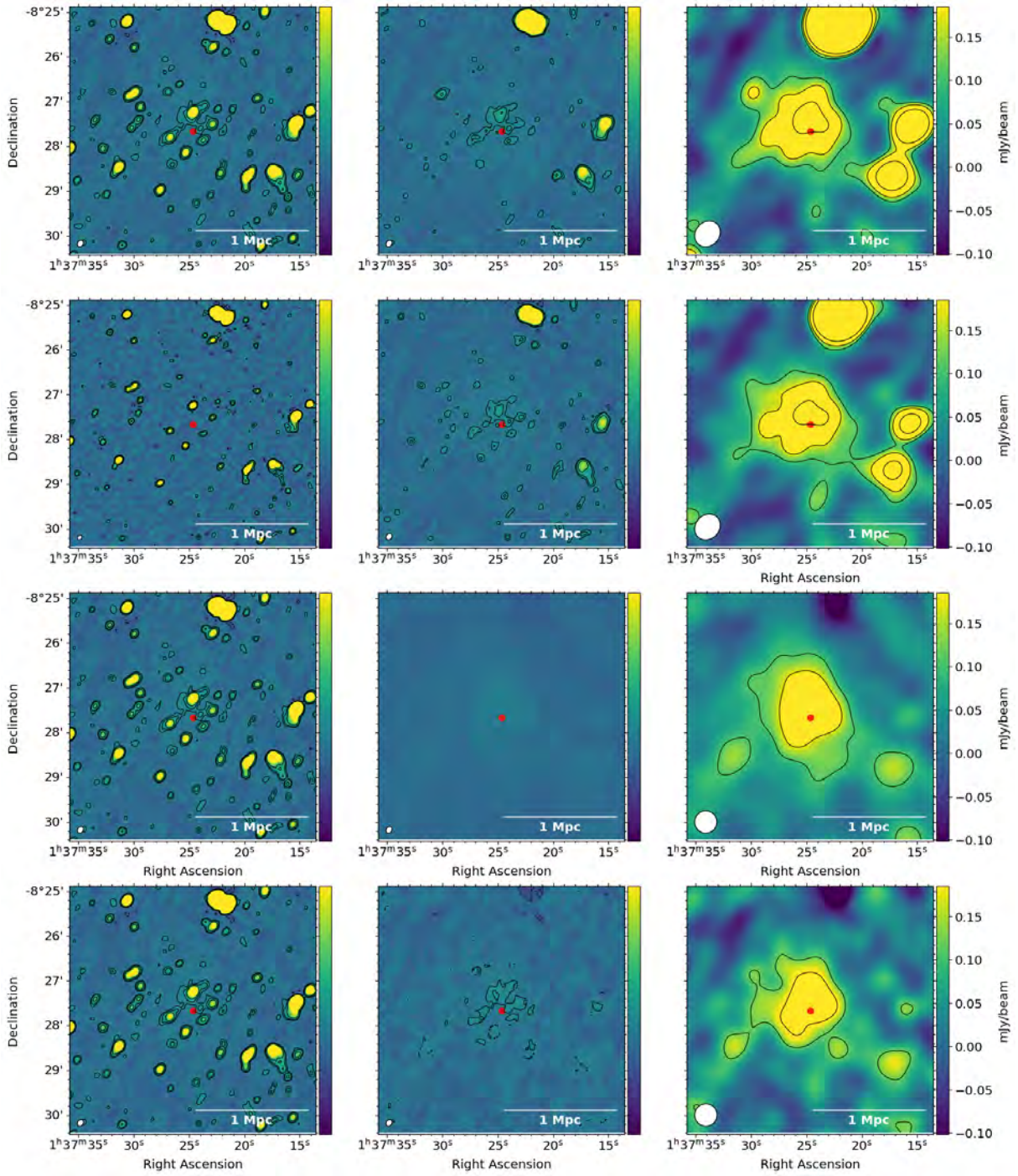


**Figure 3.5:** Comparison of source subtraction methods for J0137. Columns represent: (1) 2GC image (HR image for row 2), (2) PSSUB-FR image, and (3) PSSUB-LR image. Rows correspond to different subtraction techniques: 2GC model subtraction (*top*), HR model subtraction (*middle-top*), filtering (*middle-bottom*), and inpainting (*bottom*).

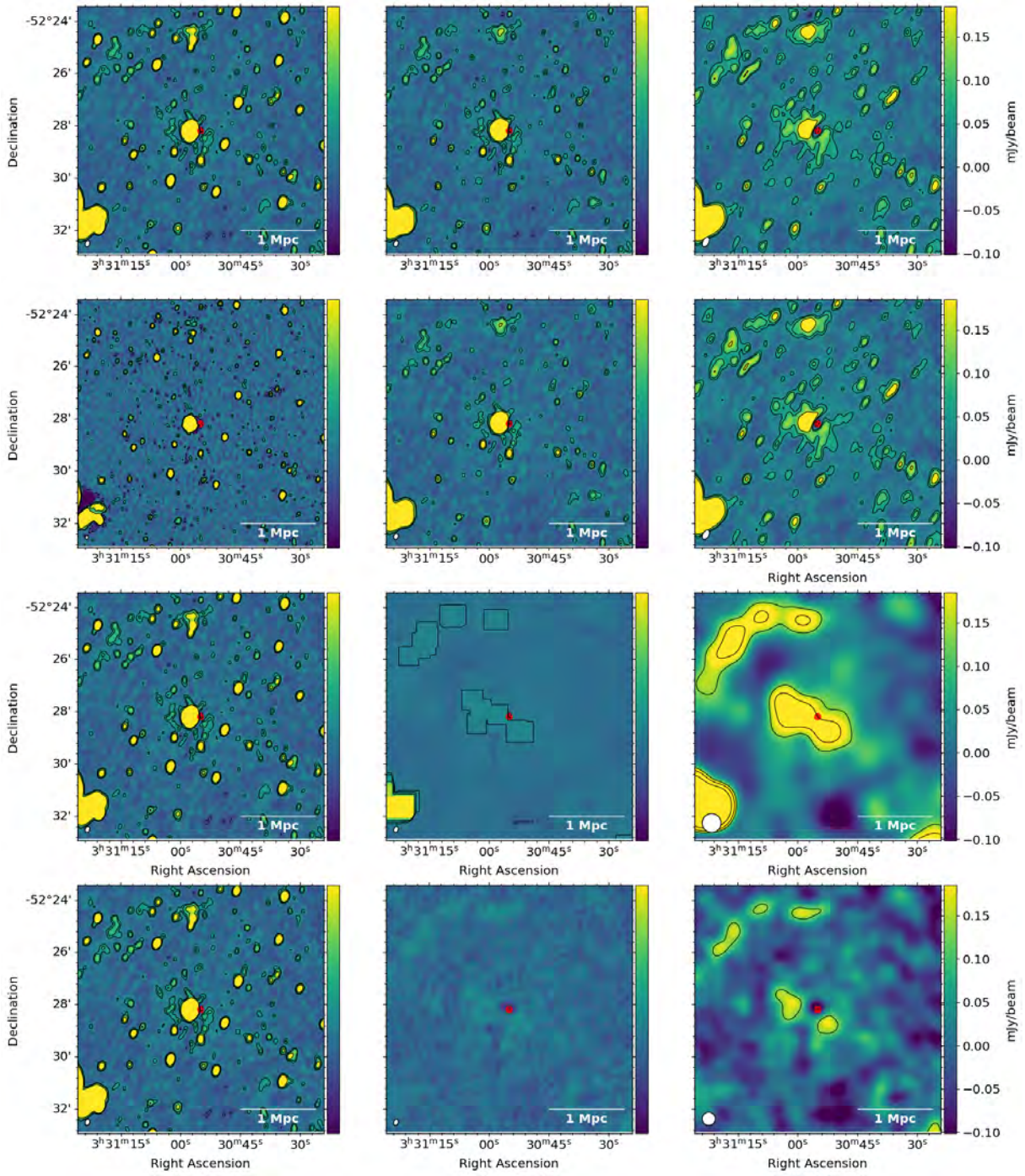


**Figure 3.6:** Comparison of source subtraction methods for J0330. Rows and columns are the same as in Figure 3.5.

subtraction was largely successful. Most compact sources are absent, revealing the underlying diffuse emission and non-compact sources. The resulting PSSUB-FR images show minimal signs of source contamination, though a quantitative analysis of the uncertainty introduced by the subtraction procedures into the LR images is provided in Section 3.1.3.

The HR model subtraction method is successful on only one field, J0137. On visual inspection, the level of source contamination appears lower than in the 2GC-subtracted image. This suggests that the HR method produced a better compact source model than the 2GC method. This method failed for J0034, likely due to the short integration time and the large number of short baselines of the MeerKAT telescope. Restricting the data to model only point sources led to severe artifacts in the images, indicating that the sources were not well modelled. An example of such an image is shown in Figure 3.7. Many of the sources visible in the 2GC image are not visible in the HR model. When the sources from this model image are subtracted from the visibilities, there is significant under-subtraction across the field, resulting in a subtracted image that still contains many compact sources. This was also the case for Knowles *et al.* (2021), who instead make use of the filtering method outlined in Section 3.1.1.3 to isolate the diffuse emission.

Both visibility plane subtraction methods are unsuccessful for the J0330 region of interest as they fail to remove the central bright source. In the PSSUB-FR images, 3 and $5\sigma$ contours appear to trace emission emanating from the central source. In the LR images, the emission appears more diffuse and elongated. Nevertheless, the central source remains visible in the subtracted images, suggesting that the emission may simply result from redistributed residual flux or from background sources.

The filtering process produces a "full-resolution" image containing only large-scale emission that appears highly "pixelated". This image is smoothed to a larger beam size (calculated by the filtering code) for visual clarity. We make sure that the beam size is large enough to resolve the emission based on our results in Section 3.1. The contours generated from the smoothed, filtered images for J0034 and J0137 resemble those produced from the previous source-subtracted images in terms of shape and extent. The filtering technique appears successful for the J0330 field, with 3 and $5\sigma$ contours tracing an elongated shape

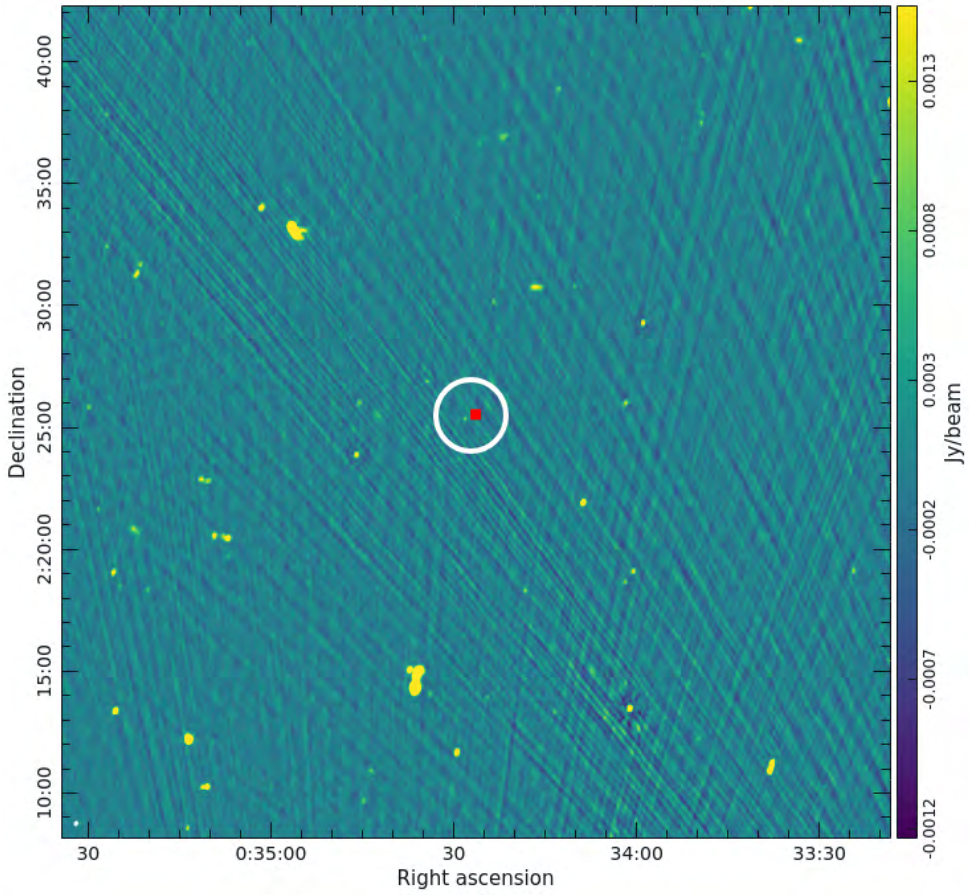


**Figure 3.7:** HR MeerKAT image of J0034, with the cluster circled in white. Artifacts from multiple sources are visible throughout the field, and the compact sources near the cluster remain entirely unmodelled.

in the north-west to south-east direction. This shape could be as a result of true emission or as a result of residual flux from sources surrounding the SZ peak. Another possibility is that this emission is AGN-related.

The inpainted images are successful for two of the three fields, the halos in J0034 and J0137 are visible in the LR inpainted images. The contours produced by these images are similar in shape and extent to the previous methods. In the J0330 inpainted image, the central source is visibly over-subtracted, leaving a negative bowl in the centre of the image.

### 3.1.3 Compact source contamination

In order to assess the effectiveness of the compact source subtraction methods, we use a statistical method derived by Knowles *et al.* (2016) to quantify the level of source contamination in the subtracted, filtered and inpainted images. We measure the flux density of 100 random off-source and on-source positions in the PPSUB-LR images. The flux densities are first measured in the PSSUB-FR images, made after source subtraction, in regions the size of one beam. The flux in the PSSUB-LR images is then measured in LR beam-sized regions. The regions are selected randomly, first measuring positions where there should only be noise (no sources) then measuring regions containing compact sources with flux densities five times the noise of the image. The mean and standard deviation are calculated for each set of flux densities. The mean of the on-source flux densities, $\mu_{src}$, gives an indication of whether the subtraction process has removed point sources effectively or if there is residual contamination. As the noise in the image should be Gaussian, the mean should be close to zero. The true flux density, $S_{true}$, is related to the measured flux density, $S_{meas}$, and $\mu_{src}$ by:

$$S_{true} = S_{meas} - (\mu_{src} \times N), \tag{3.2}$$

where $N$ is the number of beams within the measured region. The standard deviation of the fluxes at the point source positions, $\sigma_{src}$, is related to the random noise, $\sigma_{off-src}$, and the systematic noise introduced by the subtraction process, $\sigma_{sub}$. Equation 3.3 relates these values:

$$\sigma^2_{sub} = \sigma^2_{src} - \sigma^2_{off-src}. \tag{3.3}$$

When measuring the final integrated flux densities ($S$), the uncertainty in the integrated flux is given by:

$$\sigma^2_S = (f \times S)^2 + N_{beam}(\sigma^2_{rms} + \sigma^2_{sub}), \tag{3.4}$$

where $N_{beam}$ is the number of beams covering the source region, $\sigma_{rms}$ is the image noise, and $f$ is the uncertainty of the flux calibrator. The uncertainty introduced by the compact

source subtraction is given by Equation 3.3. The contamination levels are presented for all three fields in Table 3.2. The HR subtraction column for J0034 is left blank as this method failed for this cluster.

| Field | | Subtraction Method | | | |
|---|---|---|---|---|---|
| | | 2GC | HR | Filtered | Inpainted |
| J0034 | $\mu_{\text{on}}$ | 0.156 | – | 0.274 | 0.212 |
| | $\sigma_{\text{on}}$ | 0.247 | – | 0.257 | 0.311 |
| | $\mu_{\text{off}}$ | 0.058 | – | 0.122 | -0.001 |
| | $\sigma_{\text{off}}$ | 0.170 | – | 0.311 | 0.303 |
| | $\sigma^2_{\text{sub}}$ | 0.032 | – | -0.031 | 0.005 |
| J0137 | $\mu_{\text{on}}$ | 0.091 | 0.088 | -0.005 | 0.091 |
| | $\sigma_{\text{on}}$ | 0.377 | 0.214 | 0.066 | 0.121 |
| | $\mu_{\text{off}}$ | -0.002 | -0.011 | 0.019 | 0.014 |
| | $\sigma_{\text{off}}$ | 0.067 | 0.067 | 0.342 | 0.081 |
| | $\sigma^2_{\text{sub}}$ | 0.138 | 0.041 | -0.113 | 0.008 |
| J0330 | $\mu_{\text{on}}$ | 0.189 | 0.162 | -0.009 | 0.049 |
| | $\sigma_{\text{on}}$ | 0.762 | 0.249 | 0.094 | 0.064 |
| | $\mu_{\text{off}}$ | 0.010 | 0.038 | 0.009 | -0.022 |
| | $\sigma_{\text{off}}$ | 0.080 | 0.060 | 0.044 | 0.041 |
| | $\sigma^2_{\text{sub}}$ | 0.058 | 0.058 | 0.007 | 0.002 |

**Table 3.2:** Measurements used to quantify source subtraction uncertainty. All $\mu$ and $\sigma$ values are measured in units of mJy/beam$_{LR}$ and $\sigma^2_{sub}$ in units of (mJy/beam$_{LR}$)$^2$

The subtraction uncertainties for each method vary between fields, with filtering and inpainting techniques typically producing the lowest contamination levels. Each method has its own limitations. The 2GC-subtraction method, for example, depends heavily on the number of sources and the presence of complex sources in the region of interest. In sparser fields or shallow observations, such as J0034, this method performs well and serves as a viable alternative when uv-cuts cannot be applied. However, in densely populated regions, like J0137, the 2GC-subtraction method tends to under-subtract sources, leaving residual flux in the image and resulting in high uncertainties. The difference between the 2GC and HR subtraction methods arises from differences in source modelling: the HR subtraction relies on a more accurate compact source model, while the 2GC model is less refined.

Among all methods, the image plane subtractions generally produce the lowest contamination levels. As noted previously, the inpainted images suffer from residual flux at the

edges of subtracted sources in the PSSUB-FR images. When smoothed to a larger beam, these residuals are redistributed, mitigating any over-subtraction. On the other hand, filtered images are prone to flux loss because the separation of small- and large-scale emission using filters may inadvertently remove some flux, depending on the filter size.

## 3.2 Cluster diffuse emission

The properties of the emission in each cluster, measured in the PSSUB-LR images, are presented in Table 3.3. Based on the level of source contamination in the final images, we choose to use the visibility-plane and image plane PSSUB-LR images with the lowest uncertainty (level of contamination) for the remaining analyses.

| Field | LR Image | $B_{maj}$ ($''$) | $\sigma_{rms}$ ($\mu$Jy/$''^2$) | $3\sigma_{rms}$ Area ($''^2$) | $S_\nu$ (mJy) | $\Delta S_\nu$ (mJy) | LAS ($''^2$) | LLS (kpc) |
|---|---|---|---|---|---|---|---|---|
| J0034 | 2GC SS | 44.1 | 0.08 | 8620 | 2.38 | 0.63 | 118.9 | 630 |
| | Filtered | 31.2 | 0.12 | 8604 | 1.40 | 0.59 | 106.5 | 570 |
| | Inpainted | 30.0 | 0.15 | 6943 | 1.99 | 0.56 | 116.0 | 620 |
| J0137 | 2GC SS | 36.9 | 0.04 | 12021 | 0.99 | 1.20 | 157.2 | 1040 |
| | HR SS | 36.9 | 0.05 | 10903 | 0.85 | 0.70 | 131.4 | 870 |
| | Filtered | 29.7 | 0.05 | 15660 | 0.57 | 0.24 | 169.2 | 1120 |
| | Inpainted | 30.0 | 0.06 | 9047 | 3.20 | 0.38 | 121.2 | 800 |
| J0330 | Filtered | 43.2 | 0.03 | 19185 | 3.31 | 1.14 | 216.0 | 1240 |

**Table 3.3:** Emission properties measured in the PSSUB-LR images. The integrated flux density and associated error both take the subtraction uncertainty and fluxscale offset into account.

### 3.2.1 Flux density

The flux density of the emission in each cluster is measured within the $3\sigma$ contour area using the radioflux[2] plugin for SAOImageDS9, a tool for astronomical imaging and data visualization (Smithsonian Astrophysical Observatory, 2000). The values quoted in Table 3.3 take the subtraction uncertainty and fluxscale error into account using Equation 3.4. The flux density of the halo measured in the 2GC PSSUB-LR for J0034 ($S_{1.16\,\mathrm{GHz}} = 2.38 \pm 0.68$ mJy) is higer than the value reported by Knowles *et al.* (2021) ($S_{1.16\,\mathrm{GHz}} = 1.26 \pm 0.2$

[2] https://github.com/mhardcastle/radioflux

mJy). This is likely due to the use of different calibration software for processing the J0034 data. For J0137, we measured the flux density of the halo in the HR PSSUB-LR image at 1.2 GHz ($S_{1.2;\mathrm{GHz}} = 0.85 \pm 0.7$ mJy), while Sikhosana (2017) reported values of $S_{0.32;\mathrm{GHz}} = 19.7 \pm 2.3$ mJy and $S_{0.39;\mathrm{GHz}} = 15.3 \pm 2.1$ mJy. The observations in Sikhosana (2017) were conducted at approximately 300 MHz, where a greater fraction of the halo's flux is expected to be detectable. The flux density of the elongated emission in the filtered J0330 image is measured to be $S_{802\,\mathrm{MHz}} = 3.31 \pm 1.1$ mJy, which is higher than the halo emission measured in the other two clusters. This elevated flux density may be explained by the emission's large physical extent.

### 3.2.2 Largest linear size

The $3\sigma$ contours in each image are used to measure the area that the emission spans, the LAS and LLS of the emission are measured using these contours. The $3\sigma$ area each field varies with the subtraction method with inpainting typically producing the smallest area. For J0034, the 2GC subtraction and inpainted images reveal very similar LLS values for the halo. The LLS of the halo found by Sikhosana *et al.* (2021) is $\sim$ 730 kpc at a frequency of 323 MHz. This is larger than the LLS we measure at 1.16 GHz (630 kpc) and is likely due to more of the halo's extent being visible at lower frequencies (e.g. Rajpurohit *et al.*, 2021).

In the case of J0137, the area measured in the 2GC PSSUB-LR and filtered images is significantly larger than that measured in the HR PSSUB-LR and inpainted images. Both the 2GC subtraction and filtering methods introduce a higher level of uncertainty for this field, under-subtracting sources in the images and leaving residual source flux which contributes to the $3\sigma$ area. The LLS measured in all of the images is consistent with the sizes of documented radio halos.

Only one subtraction method was successful for J0330. The filtering technique separated the central source from the potential underlying emission, revealing a megaparsec-sized structure. The LLS of this emission falls within the documented range of radio halo sizes, however, its elongated shape is unusual.

### 3.2.3 Spectral index

We use GMRT images at 0.323 GHz from Sikhosana (2017) to calculate the integrated spectral indices of the halos in J0034 and J0137, respectively. The $3\sigma$ contours from the 2GC PSSUB-LR image (J0034) and the HR-model PSSUB-LR image (J0137) are used to measure the integrated flux in the PSSUB MeerKAT and GMRT images. These specific images are chosen because they yield the best results for each cluster and were generated using a visibility plane subtraction procedure similar to that used by Sikhosana (2017).

We calculate the spectral index of the halo using Equation 1.3 and determine the associated uncertainty through error propagation:

$$\Delta\alpha = \frac{1}{\ln(\frac{\nu_1}{\nu_2})}\sqrt{\left(\frac{\Delta S_1}{S_1}\right)^2 + \left(\frac{\Delta S_2}{S_2}\right)^2} \tag{3.5}$$

where the subscripts 1 and 2 indicate two different frequencies. For the J0034 halo, we find a spectral index of $\alpha^{1.16\ \mathrm{GHz}}_{0.32\ \mathrm{GHz}} = -1.34 \pm 0.14$, which is less steep than the values reported by Sikhosana *et al.* (2021) ($\alpha^{1.16\ \mathrm{GHz}}_{0.39\ \mathrm{GHz}} = -1.75 \pm 0.36$ and $\alpha^{1.16\ \mathrm{GHz}}_{0.32\ \mathrm{GHz}} = -2.26 \pm 0.32$). This discrepancy is likely due to the updated calibration software used for the MeerKAT data. While we use the same dataset as Knowles *et al.* (2021), we use the CARACal pipeline, which uncovers more of the halo emission. This results in a higher measured integrated flux density and, consequently, a less steep spectral index.

For the J0137 halo, we calculate a spectral index of $\alpha^{1.16\ \mathrm{GHz}}_{0.32\ \mathrm{GHz}} = -1.33 \pm 0.10$. This is consistent with the previously reported value of $\alpha^{0.389\ \mathrm{GHz}}_{0.323\ \mathrm{GHz}} = -1.37 \pm 0.98$ by Sikhosana (2017). The difference between the two indices is likely due to the narrow frequency range used in the earlier calculation and higher uncertainty.

The spectral indices of both halos fall within the typical range of $-1.4$ to $-1.1$ for radio halos (see van Weeren *et al.*, 2019 for a review). This suggests that the synchrotron emission mechanisms in these halos are consistent with those observed in dynamically active galaxy clusters. The relatively steep spectra ($\alpha \approx -1.3$) support the turbulent re-acceleration model, wherein cluster-scale turbulence, likely induced by merger events,

re-energises relativistic electrons and sustains synchrotron emission. These spectral properties are indicative of recent or ongoing dynamical activity in the clusters.

### 3.2.4 Classification

J0034 and J0137 both host previously detected radio halos, and archival *XMM-Newton* and *Chandra* data confirm that these clusters are dynamically disturbed (Sikhosana, 2017). J0034 is estimated to be within  100 Myr of its first pericenter passage, as determined by Doze *et al.* (2024). *Chandra* imaging reveals two distinct peaks in this cluster, indicative of an ongoing merger. Doze *et al.* (2024) further constrain the merger state and properties of J0034 by comparing three X-ray-derived mass estimates. They find a discrepancy between the temperature-based mass and gas mass which reflects that J0034 is in a disturbed merging state.

The dynamical states of J0137 and J0330 were analysed by Yuan *et al.* (2022) using *XMM-Newton* imaging. They make use of a morphology index parameter, $\delta$, derived by Yuan and Han (2020). This parameter accounts for the shape of the cluster while remaining unaffected by the X-ray exposure time, providing a robust measure of cluster dynamics. They find that relaxed systems have indices of $\delta < 0$, whereas disturbed systems are characterised by $\delta > 0$. J0137 is found to have a morphology index of $\delta = 0.49 \pm 0.01$, and J0330 of $\delta = 1.47 \pm 01$, indicating that both clusters are dynamically disturbed.

Combining the results of Sikhosana *et al.* (2021), Doze *et al.* (2024) and Yuan *et al.* (2022) with the properties we measure for both clusters, we confirm that J0034 and J0137 exhibit properties consistent with other documented merging clusters. For J0330, this classification is more complicated. While the emission is comparable in size to documented radio halos, it has an atypical morphology. We make use of multiwavelength data to further investigate the dynamics of the three clusters.

## 3.3 Dynamical state analyses

### 3.3.1 Asymmetry and centre shift parameters

Optical data can reveal much about a cluster's morphology and its constituent galaxies. The software package zCLUSTER[3] is used to estimate the maximum likelihood photometric redshifts of galaxies in each cluster field and to compute their probability distributions using photometric databases (e.g., Hilton *et al.*, 2021; Pillay *et al.*, 2021). zFIELD, a subclass of zCLUSTER, is used to generate redshift probability density maps or optical density maps within a specified redshift range for each field (see Figure C.1 in Appendix C). A central redshift, $z$, along with bounds, $\delta z$, and a photometric catalogue are chosen in order to generate the map. In this thesis, we use photometric data from the DECaLS data releases 8 and 9 to generate our optical density maps. The 2-D projected density maps of the clusters are weighted by integrating the probability distribution of each galaxy around the provided redshift within specified limits. The cluster redshift from the ACTpol DR5 catalogue (Hilton *et al.*, 2021) is used as the central redshift for each field, with upper and lower bounds set to $z_{cl} \pm \delta z$, where $\delta z = 0.2$ provides a range of redshifts.

The morphology of a cluster is closely linked to its symmetry, undisturbed clusters usually take on more symmetric shapes while disturbed or merging clusters appear more asymmetrical. The turbulence induced by merger activity can result in the formation of substructures in a cluster (e.g. Wen and Han, 2013). The asymmetry of a cluster can be quantified using an optical density map to calculate the asymmetry parameter (Conselice *et al.*, 2000). The optical density map is rotated by 180° and compared pixel-by-pixel to the original map using Equation 3.6.

$$A^2 = \frac{\Sigma(I_0 - I_\phi)^2}{\Sigma(2I_0^2)} \tag{3.6}$$

In Equation 3.6, $I_0$ represents a pixel from the original map and $I_\phi$ a pixel from the map rotated by an angle of $\phi$.

[3] https://github.com/ACTCollaboration/zCluster

The centre shift method is a method used to determine the dynamical state of a cluster by comparing the position of the SZ-peak and the peak in the optical density map. In relaxed clusters, the SZ-peak usually coincides within a few kpc with the optical centre of the galaxy cluster. At the centre of a galaxy cluster typically lies the brightest cluster galaxy which can be identified using optical images. In contrast, the SZ-peak of dynamically disturbed or merging clusters can be up to hundreds of kpc away from the optical centre (e.g. Pandge *et al.*, 2018, Pillay *et al.*, 2021).

We use the coordinates of the peak in the optical density maps and the coordinates of the cluster SZ-peak from the ACTpol DR5 catalogue to calculate a centre shift value for each cluster. Equation 3.7 is used to calculate the centre shift:

$$CS = \sqrt{(x_{\rm opt} - x_{\rm sz})^2 + (y_{\rm opt} - y_{\rm sz})^2} \tag{3.7}$$

where $x_{\rm opt}$, $y_{\rm opt}$ are the coordinates of the peak in the optical density map and $x_{\rm sz}$, $y_{\rm sz}$ are the coordinates of the SZ-peak. Equation 3.7 provides the angular separation of the two peaks which can be used along with the image pixel size in Mpc and cluster redshift to find the projected distance in Mpc.

The centre shift and asymmetry parameters are plotted for each cluster in Figure 3.8. Pillay *et al.* (2021) use this method to classify a sample of 98 galaxy clusters with known dynamical states. They find that clusters with an asymmetry value, $A^2$ >0.1 and centre shift value, $CS$ >0.4 are dynamically disturbed. In contrast, clusters with centre shift values, $CS < 0.4$, and asymmetry values $A^2 < 0.1$ could be classified as either relaxed or disturbed. All clusters found outside of this ambiguous region, however, were classified as disturbed. Our three clusters lie outside of this ambiguous region, indicating that they are likely disturbed. This aligns with earlier results suggesting that the emission, particularly in J0034 and J0137, is merger-driven. The elongated emission in J0330 may arise from a combination of merger-driven and galaxy-scale emissions viewed in projection.

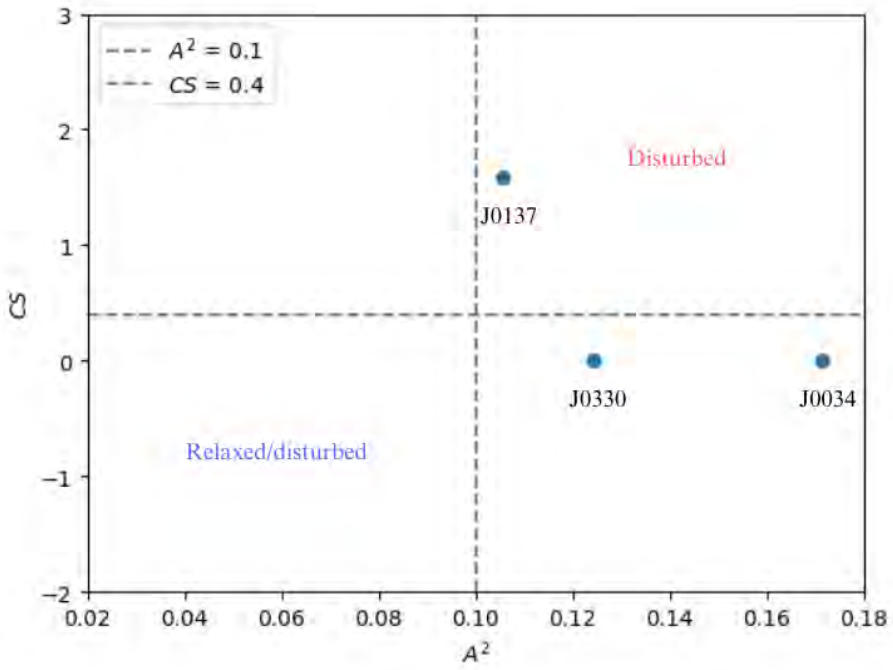


**Figure 3.8:** Plot of centre shift versus asymmetry parameter. Clusters siding in the lower left quadrant can be either relaxed or disturbed while clusters in the remaining three quadrants are likely disturbed.

### 3.3.2 Comparison with X-ray morphology

The morphology of radio halos often mirrors the distribution of X-ray emission (Feretti, 2000). Recent studies have uncovered radio halos where the radio and X-ray components are non-uniform and display surface brightness discontinuities (Botteon *et al.*, 2023). We make use of archival *XMM-Newton* X-ray images to compare the morphologies of the radio halos in J0034 and J0137 and the elongated emission in J0330. For J0330, we also make use of an *eROSITA* image (Sunyaev *et al.*, 2021) as the cluster lies at the edge of the *XMM-Newton* image. Figure 3.9 shows the available X-ray images for our clusters.

For both J0034 and J0137, the X-ray emission is similar in shape to the radio contours, suggesting a strong correlation between the radio emission and merger activity in these clusters. This supports the idea that the diffuse radio halos are driven by turbulence

generated during the merging process. In J0034, the X-ray emission appears to have two peaks and is slightly offset from the radio emission, a morphology indicative of merger activity.

The radio emission in the centre of J0330 does not entirely resemble the shape of the X-ray emission in the *XMM-Newton* and *eROSITA* images. The brightest part of the X-ray emission shows slight elongation in the north-west to south-east direction, however, the overall shape of the emission differs vastly in the radio and X-ray images. The central radio emission appears slightly offset from the X-ray emission. This displacement may indicate that the ICM's thermal and non-thermal components are not perfectly aligned,

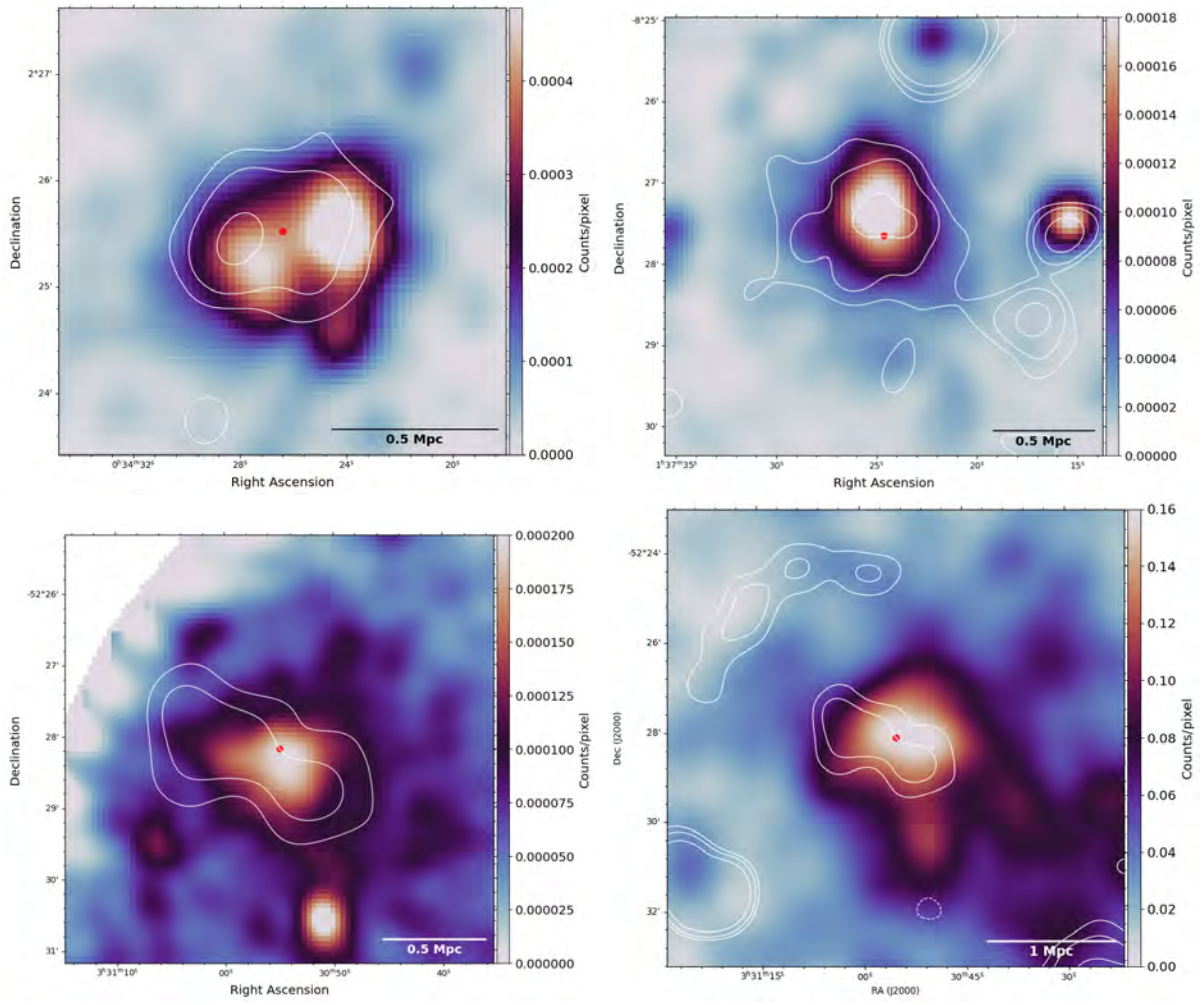


**Figure 3.9:** X-ray images for each cluster with LR MeerKAT contours overlaid. *Top right*: J0034 *XMM-Newton* image (Obs. ID: 0650380601). *Top left*: J0137 *XMM-Newton* image (Obs. ID: 0920890401) with LR. *Bottom right*: J0330 *XMM-Newton* image (Obs ID: 0400130201). *Bottom right*: J0330 *eROSITA* image.

potentially reflecting asymmetries in merger dynamics or projection effects. Based on the X-ray morphology, the elongated radio emission is unlikely to be solely an elongated halo. Instead, it is more likely a combination of a radio halo and residual emission from nearby radio sources, such as AGN jets that could contribute to the elongated radio morphology. To the north-west of the cluster centre we also detect an arc-shaped structure which appears morphologically similar to a cluster radio relic. There are no corresponding shocks visible in the *eROSITA* image that would indicate that the structure is a relic. The structure may be a combination of of residual flux from the extended sources visible in that region in the 2GC image (see left-hand column in Figure 3.6).

## 3.4 Radio cluster members

Cluster galaxies often reflect the turbulence present in merging clusters. Tailed galaxies and sources with complex morphologies interact with the dynamic cluster environment, adopting disturbed structures. These features serve as indicators of merger activity, and electrons from such galaxies can contribute to the cluster's diffuse emission, further complicating its structure (e.g. Skillman *et al.*, 2013, Rajpurohit *et al.*, 2022b, Lusetti *et al.*, 2023.

The most reliable method to select cluster members is through the use of spectroscopic redshift data. However, spectroscopic surveys with wide coverage are not always readily available. Cluster membership can, however, be determined relatively accurately using the photometric redshift distributions calculated using zCluster. To determine cluster membership, we make use of the photometric redshift and probability columns in the zCluster catalogues. We follow the same method as Kesebonye *et al.* (2022) that was developed by Brunner and Lubin (2000) and (Pelló *et al.*, 2009). We make use of the same DECaLS data as (Kesebonye *et al.*, 2022) and so we assume the same parameters used for this method of cluster membership. The probability of a galaxy in the field being a cluster member is given by:

$$P_{\text{member}} = \int_{z_{cl}-\delta z}^{z_{cl}+\delta z} P(z)dz \tag{3.8}$$

where $\delta z = n\sigma_{bw}(1 + z_{cl})$, $z_{cl}$, is the redshift of the cluster, $n\sigma_{bw}$ is the scatter in the photometric versus spectroscopic redshifts calculated using the bi-weight method by Kesebonye *et al.* (2022). For these data we use a scatter of $\sigma_{bw} = 0.03$ and a factor of $n = 2$. The $M_{200}$ value for each cluster is obtained from the ACTPol DR5 catalogue and is used to calculate the $R_{200}$ value for the cluster (Datta *et al.*, 2018). We apply the cluster membership conditions to the zCluster catalogues, classifying galaxies within the $2 \times R_{200}$ region as members, and cross match with the 2GC MeerKAT catalogues to determine which cluster members are visible in our radio images.

The MeerKAT catalogues containing only cluster members are then cross-matched with catalogues generated from the GMRT images (J0034 and J0137) used previously. In the case of J0330, the UHF-band MeerKAT catalogue is cross-matched with an L-band catalogue generated from new MeerKAT images that will be discussed in the next chapter. Table 3.4 summarizes the number of sources detected at each stage of the cross-match for each field.

| Field | DECaLS Sources | | Cluster Sources | | | |
|---|---|---|---|---|---|---|
| | Full zCluster Catalogue | $R_{200}$ | $R_{200}$ | $MK_L$ | $MK_{UHF}$ | GMRT |
| J0034 | 49349 | 8503 | 1394 | 32 | – | 8 |
| J0137 | 47114 | 4921 | 846 | 55 | – | 10 |
| J0330 | 52441 | 5817 | 986 | 9 | 9 | – |

**Table 3.4:** Number of sources present at each stage of the membership and cross-matching procedure.

The HR and LR MeerKAT contours are overlaid on the DES DR2 optical image tiles presented in Figures 3.10 – 3.12 to visually assess the spatial distribution and properties of sources relative to the clusters in order to gauge whether the cluster members are likely contributors to the emission seen in each cluster. These DES tiles are small, focusing on the inner $\sim 0.5R_{200}$ area of each cluster. Most of the radio cluster members are not visible in these images. Table 3.5 summarises the properties of cluster members visible in the DES images.

To measure the spectral indices, we measure the flux density of sources within $5\sigma$ contour regions across the images at different frequencies. These measurements are made using

| Field | Source | RA (deg) | DEC (deg) | $S_{1.2\,GHz}$ (mJy) | $S_{0.82\,GHz}$ (mJy) | $S_{0.32\,GHz}$ (mJy) | $\alpha_{0.32}^{1.2}$ |
|---|---|---|---|---|---|---|---|
| J0034 | S1 | 8.617 | 2.423 | 1.29 ± 0.04 | – | 2.60 ± 0.18 | 0.54 ± 0.14 |
| J0137 | S1 | 24.375 | -8.448 | 0.535 ± 0.02 | – | 0.756 ± 0.10 | 0.29 ± 0.02 |
| | S2 | 24.361 | -8.463 | 0.258 ± 0.02 | – | 0.195 ± 0.25 | -0.23 ± 0.15 |
| | S3 | 24.345 | -8.458 | 0.171 ± 0.01 | – | 0.393 ± 0.07 | 0.69 ± 0.02 |
| | S4 | 24.332 | -8.478 | 0.108 ± 0.02 | – | 1.414 ± 0.12 | 0.23 ± 0.01 |
| | S5 | 24.327 | -8.504 | 0.256 ± 0.01 | – | 0.373 ± 0.07 | 0.31 ± 0.02 |
| | S6 | 24.315 | -8.501 | 0.141 ± 0.01 | – | 0.140 ± 0.06 | 0.00 ± 0.05 |
| J0330 | S1 | 52.678 | -52.488 | 0.163 ± 0.02 | 0.224 ± 0.02 | – | 0.67 ± 0.03 |
| | S2 | 52.738 | -52.469 | 68.0 ± 0.07 | 91.2 ± 0.06 | – | 0.63 ± 0.10 |

**Table 3.5:** Properties of optically identified cluster members for each field.

the radioflux plugin for SAOImageDS9. Assuming a power-law model for the flux density as a function of frequency, we compute the spectral indices of cluster members.

In J0034, only one cluster member is visible in the DES image (see Figure 3.10). This source lies within the halo region and may contribute relativistic electrons to the halo. The cluster member galaxies lying outside the $\sim 0.5R_{200}$ region are predominantly compact. The distribution of compact sources across the $2 \times R_{200}$ region suggests interactions with the ICM, though no significant evidence of turbulence is observed in the majority of sources.

J0137 contains two sources near the cluster centre with complex morphologies that may contribute to the electron population driving the radio halo (see Figure 3.11). One of these sources, S4, located south-east of the cluster centre, may be a poorly resolved Fanaroff-Riley Type I (FR I) galaxy. Its jets would be slightly bent away from the cluster centre, which may suggest interaction with a turbulent ICM.

The J0330 cluster hosts a mix of compact sources and more complex morphologies, particularly on the southeastern side of the cluster (see Figure 3.12). These sources may be contributors to the elongated radio emission observed in that region. However, the northwestern portion of the emission cannot be easily explained by the current distribution of cluster members. The arc-shaped feature is also observed in this region (see Figure 3.6 and 3.9) which overlaps with a cluster galaxy and coincides with several other radio sources. It is possible that these sources collectively contribute to the arc-shaped

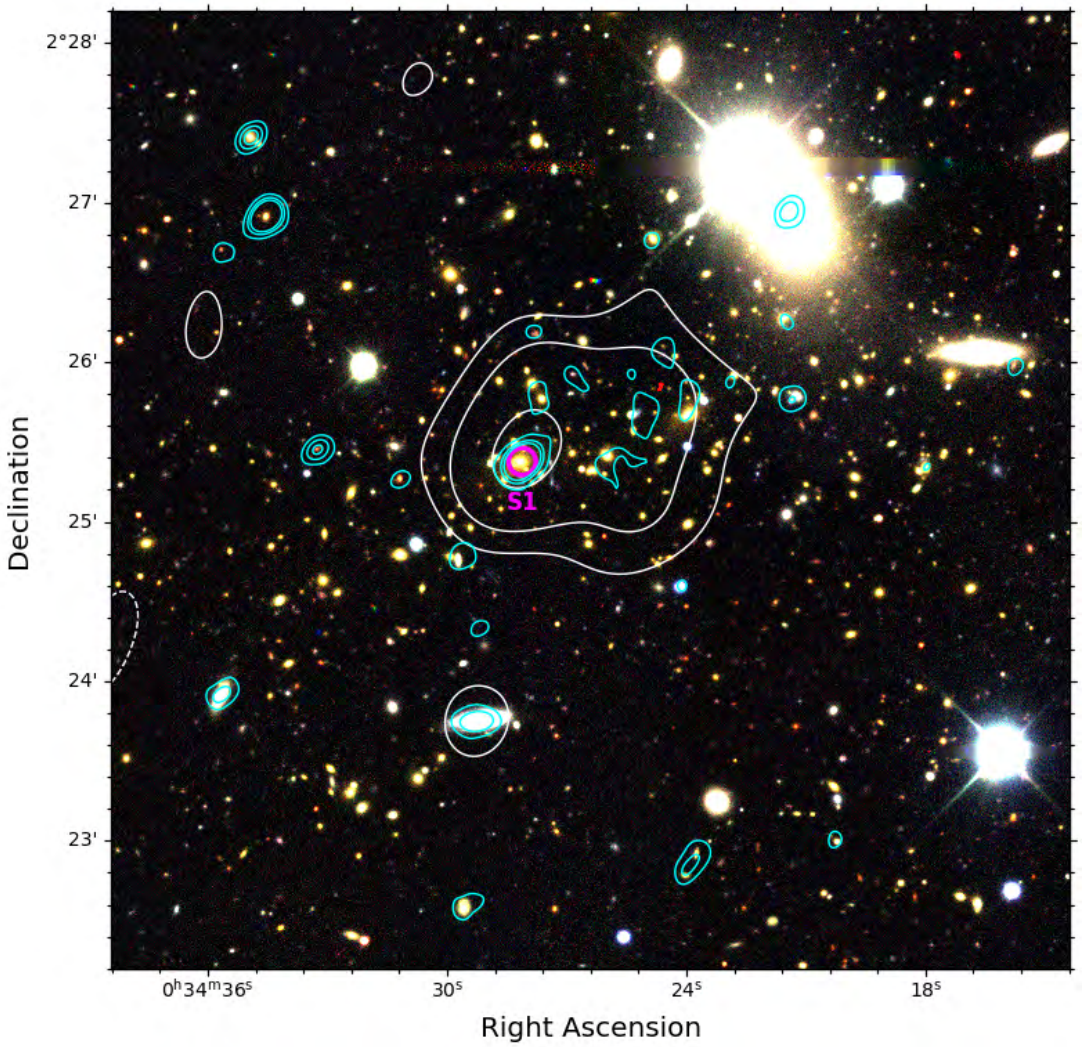


**Figure 3.10:** DES optical image of J0034 with LR MeerKAT contours (3, 5, and 10$\sigma$) overlaid in white to highlight the position of the halo, cyan FR contours (5 and 10$\sigma$) to indicate the position of radio sources and magenta markers indicating cluster members visible in the MeerKAT and GMRT images.

structure.

The cluster members visible in the FR MeerKAT and GMRT images are used to study the spectral index distribution of cluster members. Figure 3.13 shows the spectral index of cluster members for each field, plotted against their normalised radial distance from the respective cluster centre. We perform a linear regression on the plotted data to determine whether there is any correlation between the spectral index of cluster members and their projected position in the cluster. Such a relationship could suggest underlying environmental effects, such as density variations or dynamical interactions with the intracluster

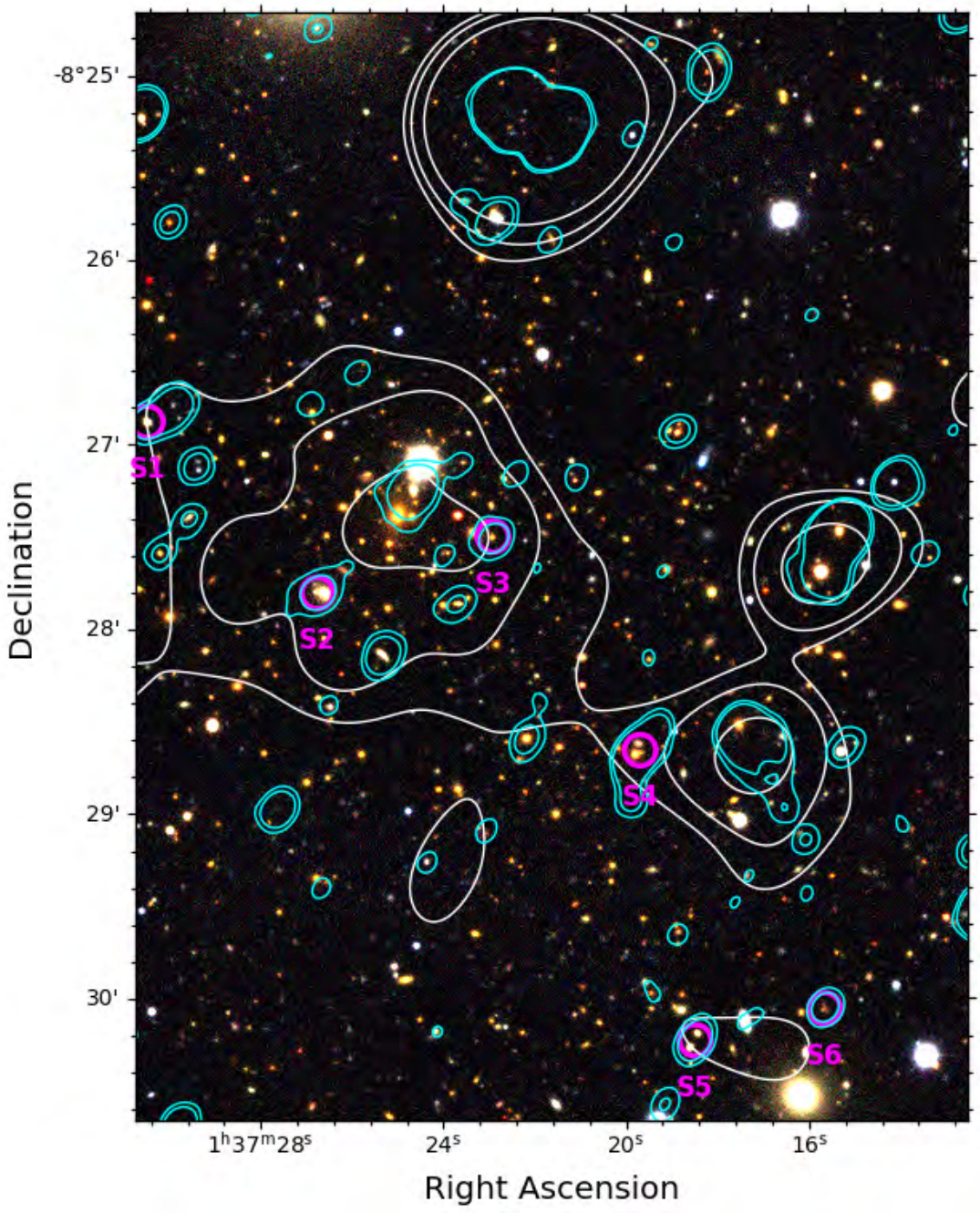


**Figure 3.11:** DES optical image of J0137. Contours and notations are the same as in Figure 3.10.

medium, that influence the energy distribution of cluster members.

The $R^2$ value calculated by the linear regression indicates the proportion of variance in the dependent variable (in this case, spectral index) that is explained by the independent variable (radial distance) in the linear regression model. The $p$-value tests the null hy-

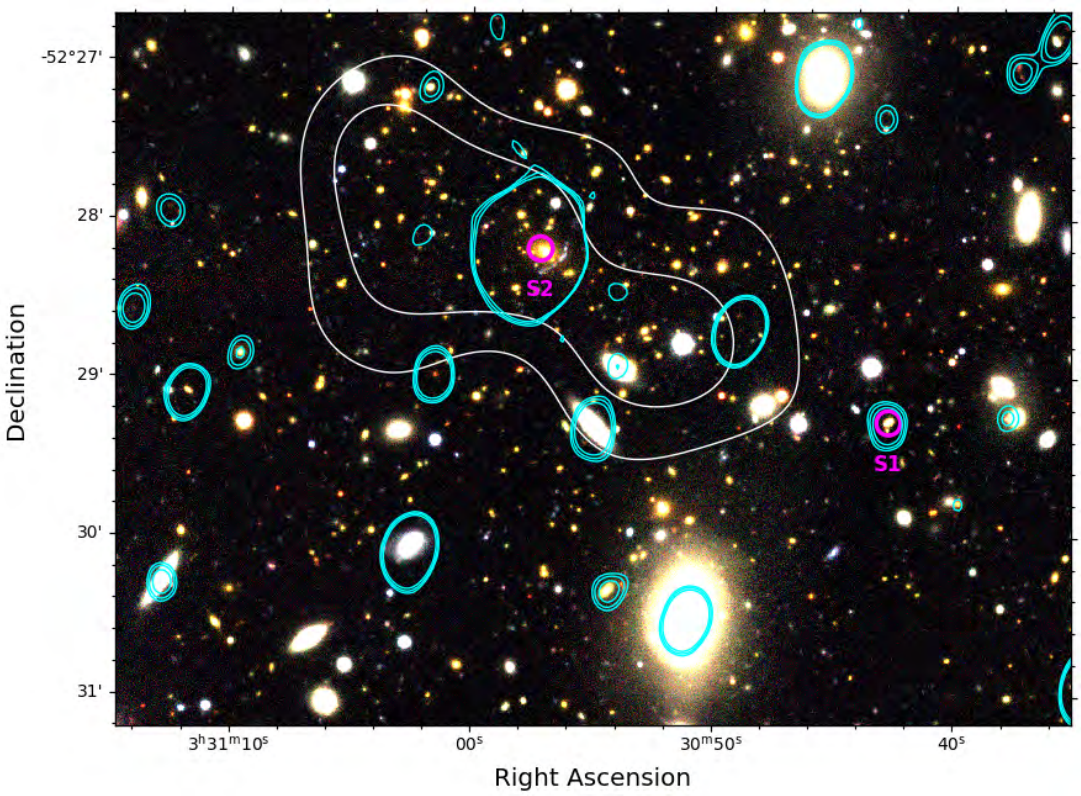


**Figure 3.12:** DES optical image of J0330. Contours and notations are the same as in Figure 3.10.

pothesis that the slope of the regression line is zero (i.e., there is no linear relationship between radial distance and spectral index). The commonly used significance level is $p = 0.05$; values higher than this indicate that the null hypothesis cannot be rejected, suggesting that any observed relationship between radial distance and spectral index could easily be due to chance.

Low values of $R^2$ ($\lesssim 0.3$) indicate that little of the variation in spectral index can be explained by radial distance, indicating a weak linear relationship that does not account for much variability in spectral index. A $p$-value greater than 0.05, would suggest that there is no statistically significant relationship between spectral index and radial distance. The combined dataset yields an $R^2$ value of 0.080 and a $p$-value of 0.144, both of which indicate a lack of a linear correlation between the spectral index and the radial position of sources within the clusters.

For all three clusters, the predominance of flat-spectrum sources ($\alpha \gtrsim -0.5$) suggests

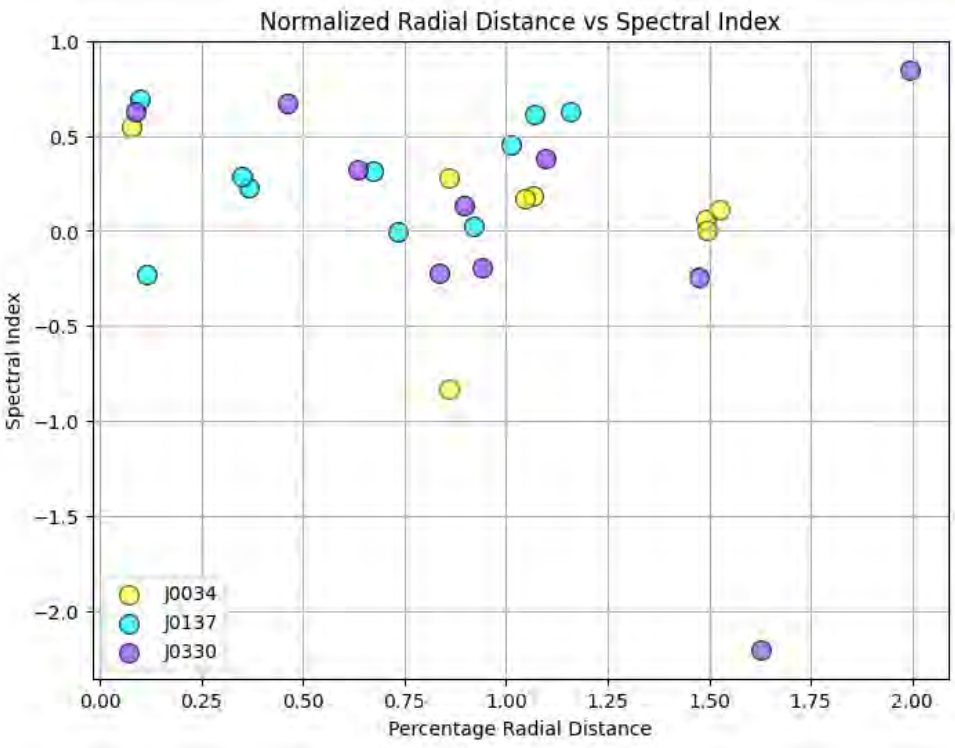


**Figure 3.13:** The normalised radial distance of cluster members from all three cluster fields plotted against spectral index.

on-going activity in the cluster environments. In each case, at least one source is located within the $3\sigma$ halo region. These flatter-spectrum sources are likely powered by active processes, such as AGN activity, where relativistic electrons are continuously injected into the surrounding medium. Alternatively, they could be radio-loud star-forming galaxies, where synchrotron radiation from starburst-driven processes dominates the emission. The lack of widespread steep-spectrum sources ($\alpha \lesssim -0.5$) suggests that interactions with the ICM may be localized rather than spread across the cluster regions, indicating that merger activity in these clusters is recent or in an early stage.

## 3.5 Summary

In this chapter, we presented the results of our post-processing analyses. The optimal beam size for all three clusters was determined to be around $30''$. We evaluated four methods of compact source subtraction, finding that the inpainting image plane subtraction procedure generally introduces the least uncertainty. The 2GC subtraction procedure,

while effective for small datasets or sparse fields, is highly dependent on the density and type of sources in the field. Of the two visibility plane subtraction procedures, the HR subtraction produced the best results for J0137 but was unsuccessful for J0034 due to the short observation time. We measured the LLS, integrated flux densities, and spectral indices for the diffuse emission in each field and found these to be consistent with published values for J0034 and J0137. Dynamical state analyses were conducted to further classify the emission, with both X-ray morphology and optical density parameters indicating that our clusters are disturbed. For J0330, however, the radio and X-ray morphologies do not align as closely as in the other clusters, suggesting that the emission is not solely from a radio halo. Finally, we examined radio cluster members and their morphologies to investigate whether cluster galaxies contribute electrons to the central emission. In each cluster, at least one source coincides with the central emission and may be contributing electrons to it.

# Chapter 4

# Multiwavelength Investigation of Diffuse Emission South of J0330

Approximately 20 arcminutes south of the J0330 cluster, we discover two diffuse objects, which we name the wedge and the arc due to their distinctive shapes. The structures appear morphologically similar to a pair of cluster radio relics. At the redshift of J0330, $z = 0.44$, the wedge and arc would have physical sizes of 1.03 Mpc and 1.41 Mpc, respectively. These sizes fall within the size range of documented cluster radio relics. A prerequisite for relics to be present is cluster merger activity. While we determined that J0330 is a candidate for merger activity in the previous chapter, the objects are too far from the cluster to be associated with it. There are also no documented galaxy clusters at the objects' position at a redshift that would give them physical sizes similar to known cluster relics.

## 4.1 Radio properties

A close-up of the structures in the FR UHF-band image is presented in Figure 4.2. The wedge has a triangular shape with a flat western edge and a radio peak in the western corner. The arc has a curved, elongated morphology with a sharp edge on the western side. The radio properties of both structures are summarised in Table 4.1.

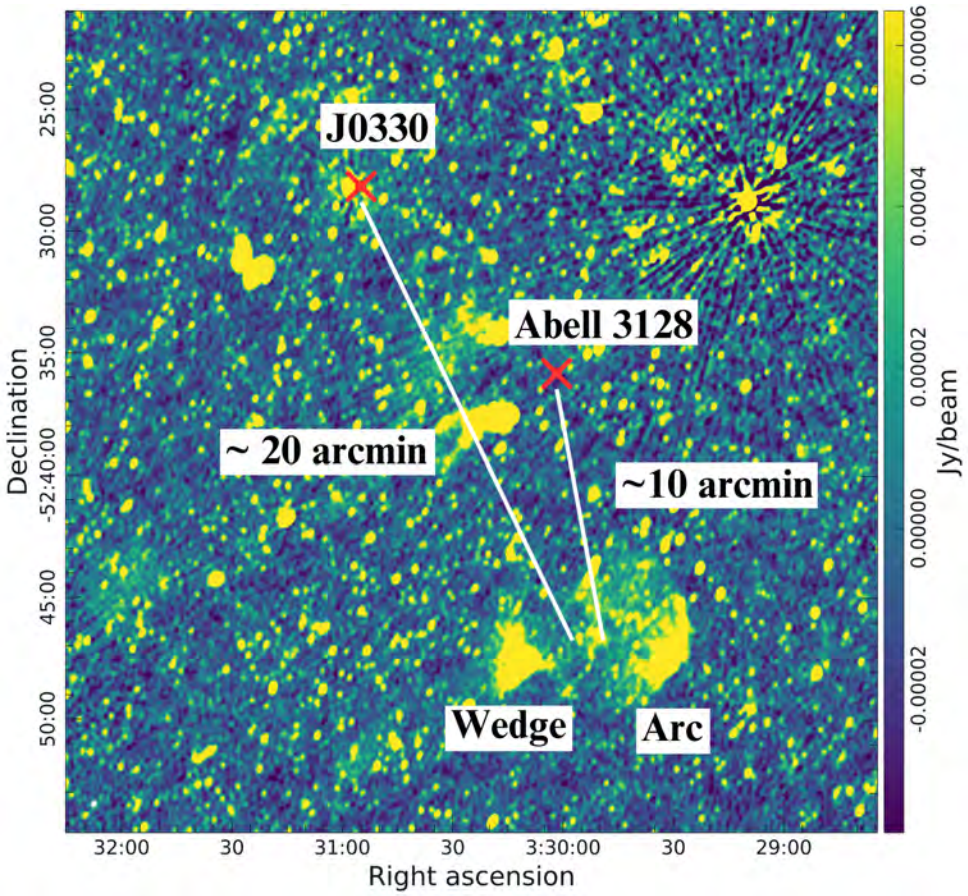


**Figure 4.1:** Close-up of the J0330 FR UHF-band image indicating the positions of J0330, Abell 3128 ($z = 0.06$), and the emission.

As discussed in Chapter 1, spectral index maps can aid in classifying diffuse emission. If the objects are radio relics, they would exhibit a spectral index gradient across their width. For the arc, this gradient would be expected to run perpendicular to the curved edge of the structure. In contrast, if the emission is associated with a radio galaxy, the jets would display a spectral gradient along their major axes.

We use the HR PSSUB MeerKAT UHF data to generate in-band spectral index maps using the software Broadband Radio Astronomy ToolS (BRATS, Harwood *et al.*, 2018). The data is imaged at two equally spaced sub-bands to create low- and high-frequency images, both of which are convolved to the same beam size before making the map. We create the map using the default BRATS settings, changing only the sigma level to $2.5\sigma$ as most of the emission visible in our images had low SNR. The spectral index map and associated error map are presented in Figure 4.3. The regions included in the maps are

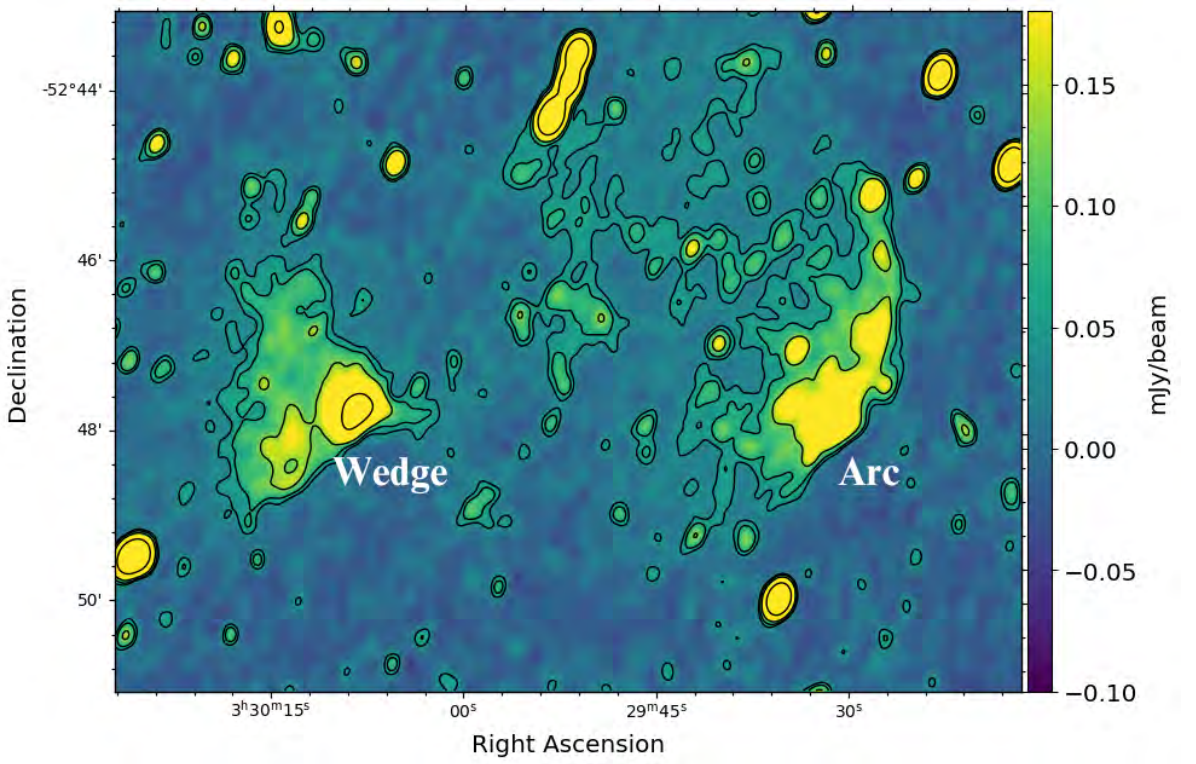


**Figure 4.2:** Close-up of the structures discovered in the J0330 field. The contours are at 3, 5, 10 and 50$\sigma$.

| Property | Wedge | Arc |
|---|---|---|
| LAS (arcmin) | 3.00 | 4.08 |
| $S_{802\ \mathrm{MHz}}$ (mJy) | 12.9 ± 0.14 | 14.4 ± 0.07 |
| $\alpha^{944\ \mathrm{MHz}}_{802\ \mathrm{MHz}}$ | -1.4 ± 0.2 | -1.1 ± 0.1 |

**Table 4.1:** Properties of the wedge and the arc measured in the UHF-band MeerKAT image. The spectral index is calculated between the central UHF frequency and the frequency of the EMU image.

limited and largely unconstrained due to the low SNR of the emission at the frequency extremes. We use the PSSUB images in an attempt to boost the SNR of the emission, however only the brightest portions of the emission provide reliable spectral indices.

The brightest region of the wedge reveals a spectral index of approximately $-1.3 \pm 0.3$. Images from the Evolutionary Map of the Universe survey (EMU, Norris *et al.*, 2011) at 944 MHz, with a noise level of $\sigma = 26$ μJy/beam (for a circular 15″ beam), are used in conjunction with the UHF-band MeerKAT image to create a similarly unconstrained map. While parts of these objects are visible in RACS low- and mid-frequency images,

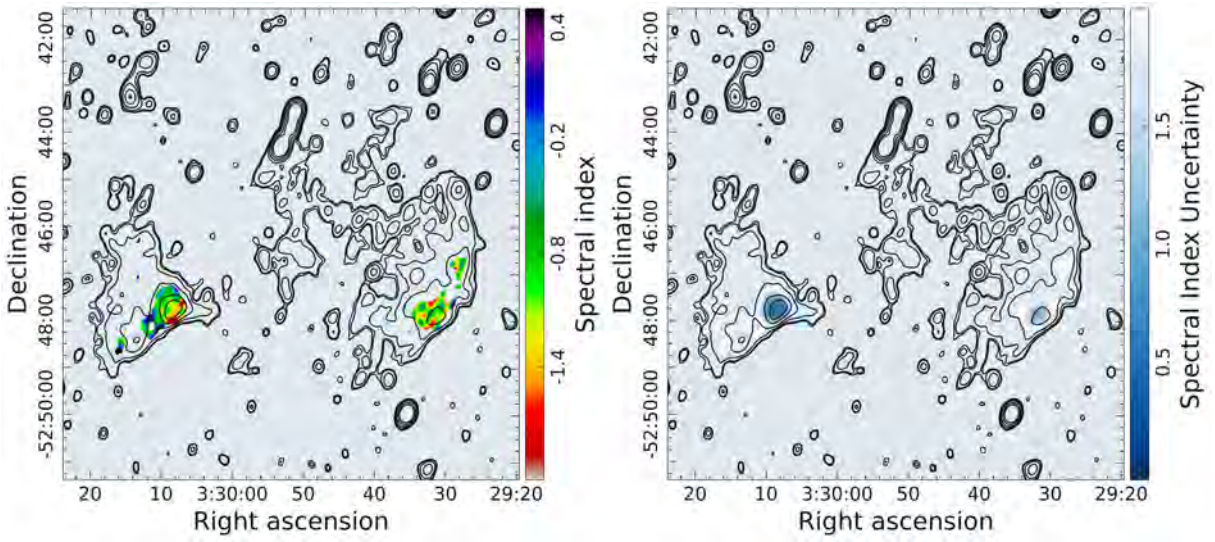


**Figure 4.3:** In-band spectral index (*left*) and associated uncertainty (*right*) maps of the wedge and arc sources, with 2.5, 3, 5, 10, 25 and 50$\sigma$ UHF radio contours overlaid.

the diffuse structure is undetectable due to their much lower sensitivity.

An integrated spectral index measurement, within a matched volume defined by the 3$\sigma$ contours of the MeerKAT UHF-band and EMU images, reveals a steeper spectral index of $\sim -1.4$ for the full wedge region. This suggests that the fainter, diffuse portion of the source may result from an older electron population, which would cause a steepening of the spectral index. The arc exhibits an integrated spectral index of $\sim -1.1$, consistent with the results of both radio relics and AGN-driven sources.

As reliable maps could not be made with the existing radio data, observation time with the MeerKAT was requested to enable the creation of wide-band spectral index maps (proposal ID: DDT-20240805-MW-01). The observation set-up and 2GC image properties are summarised in Table 4.2. The data is calibrated using the same procedure applied to the J0034 L-band data in Section 2.3.2.

We combine the UHF image at 802 MHz and the L-band image at 1.2 GHz, with both images smoothed to a circular beam size of 15″, to create the wide-band spectral index map presented in Figure 4.4. Despite this improvement, the uncertainties in the wide-band spectral indices remain relatively high for the 2.5$\sigma$ to 5$\sigma$ regions. To achieve constrained wide-band spectral index maps, the faintest emission must be detected at levels between

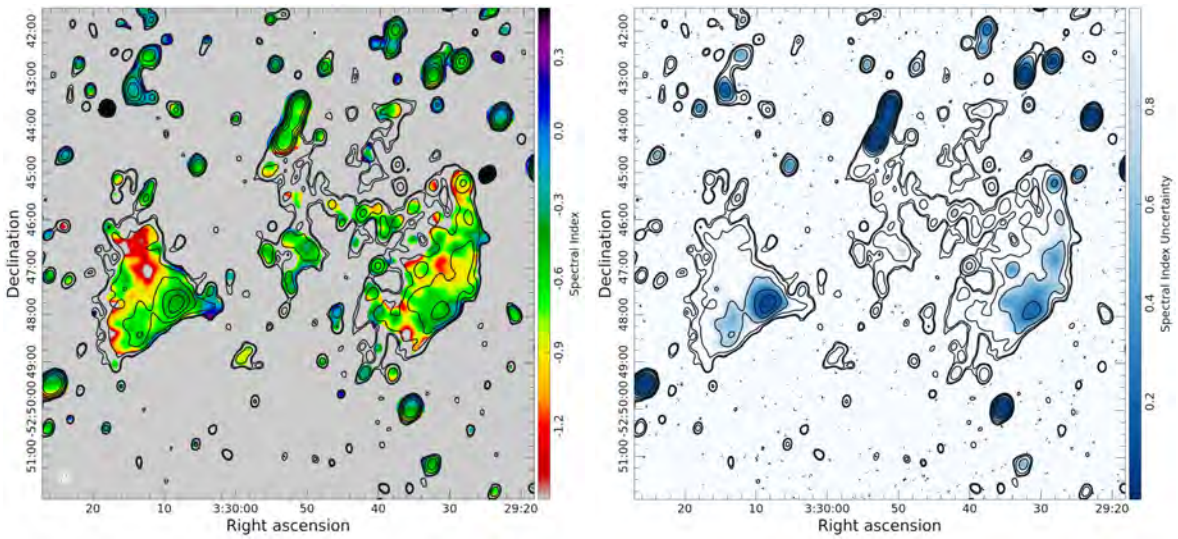


**Figure 4.4:** Spectral index map (*left*) and error map (*right*) for the wedge and arc. The UHF radio contours are overlaid at 2.5, 3, 5, 10, 25, 50$\sigma$.

| | | |
|---|---|---|
| Observation | Central frequency (GHz) | 1.284 |
| | Bandwidth (MHz) | 856 |
| | Channels | 4096 |
| | Channel width (kHz) | 209 |
| | Integration time (s) | 8 |
| | Total time (hrs) | 4 |
| 2GC Image | $B_{\rm Maj}$ ($''$) | 9.2 |
| | $B_{\rm Min}$ ($''$) | 6.9 |
| | PA (deg) | -74.7 |
| | $\sigma_{rms}$ ($\mu$ Jy/beam) | 5.8 |

**Table 4.2:** Observation set-up and 2GC image properties for the new L-band observation. The FR 2GC image is presented in Appendix A.

5$\sigma$ and 10$\sigma$, based on the uncertainty constraints shown in Figure 4.4. Even with the larger beam sizes, the faint $2.5 - 3\sigma$ emission remains approximately 3 to 3.5 times the noise level in both images. To further enhance the sensitivity to this emission, source subtraction procedures, such as those outlined in the previous chapter, would need to be applied. Additionally, advanced calibration techniques could be employed to mitigate the artefacts observed in the L-band and UHF-band images, potentially improving the detection of the faintest emission. However, this is beyond the scope of this thesis.

## 4.2 Redshift determination

### 4.2.1 Optical galaxy counterparts

In order to determine the origin of the emission, we search for optical sources in the DES DR2 image tiles coinciding with the peaks in the radio images within the emission regions. The composite *gri*-band image is presented in Figure 4.5. For radio peaks with no visible optical counterpart, we search for the position of the peak using the NASA/IPAC Extragalactic Database (NED). The sources and their properties are presented in Table 4.3.

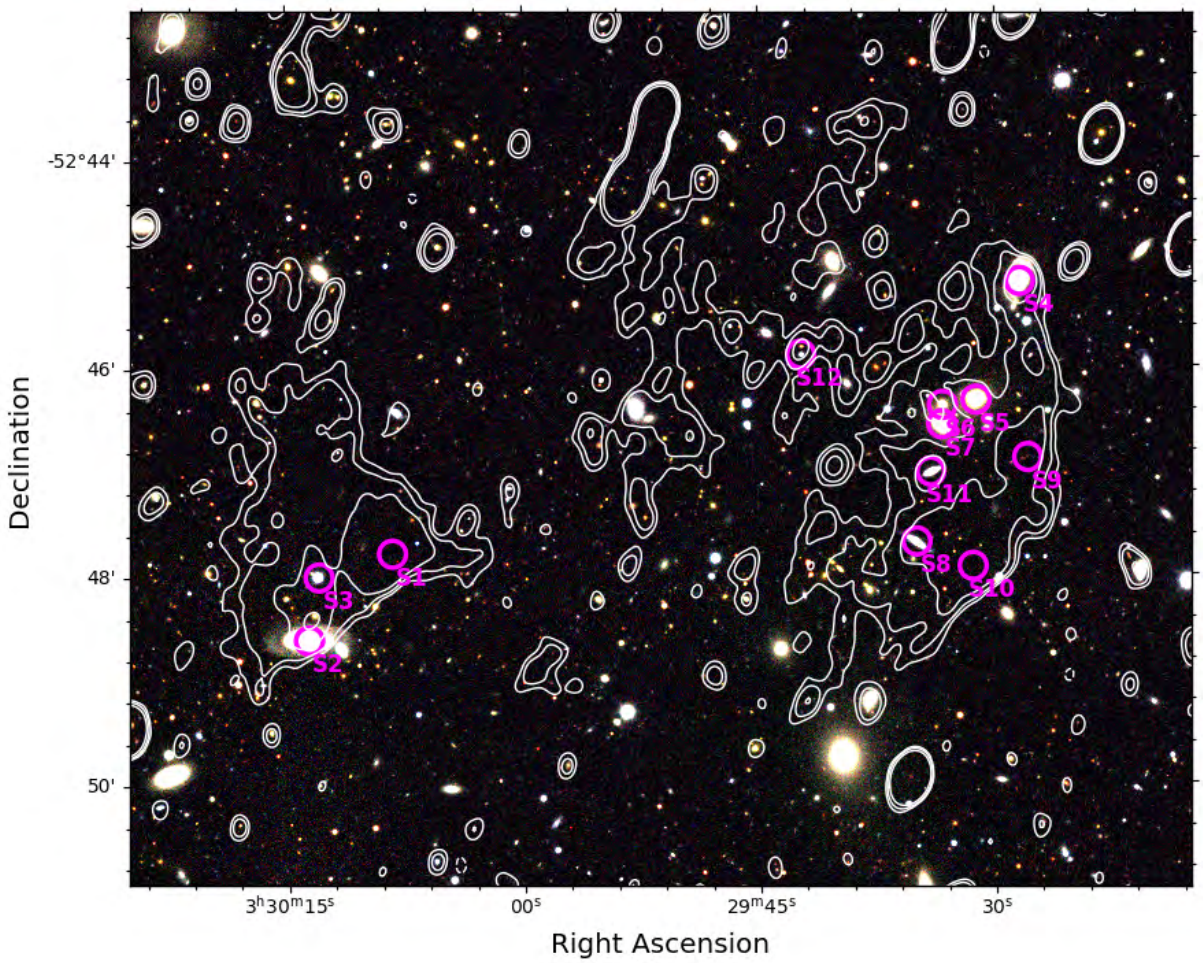


**Figure 4.5:** Optical *gri*-band DES image with UHF radio contours overlaid. The contour levels are 3, 5, and 10$\sigma$. Potential sources of the emission are numbered and circled in magenta.

| Emission | Number | RA | DEC | Name | Category | Redshift |
|---|---|---|---|---|---|---|
| Wedge | S1 | 52.535 | -52.796 | WISEA J033008.02-524742.9 | IrS | – |
| | S2 | 52.556 | -52.810 | WISEA J033013.63-524836.5 | G | 0.055572 ± 3.34e-4 |
| | S3 | 52.554 | -52.800 | WISEA J033013.05-524800.2 | UvS | – |
| Arc | S4 | 52.368 | -52.753 | WISEA J032928.44-524511.1 | IrS | – |
| | | | | 2MASX J03292834-5245099 | G | 0.059368 ± 8.70e-5 |
| | S7 | 52.380 | -52.772 | WISEA J032931.18-524619.5 | G | 0.115503 ± 1.17e-4 |
| | S6 | 52.389 | -52.773 | WISEA J032933.36-524621.6 | G | – |
| | S7 | 52.389 | -52.776 | WISEA J032933.39-524634.0 | G | 0.056459 ± 9.00e-5 |
| | S8 | 52.396 | -52.795 | WISEA J032934.96-524742.0 | G | 0.071960 ± 6.30e-5 |
| | S9 | 52.366 | -52.781 | WISEA J032927.92-524652.7 | IrS | – |
| | S10 | 52.381 | -52.799 | WISEA J032929.79-524802.7 | IrS | – |
| | S11 | 52.392 | -52.784 | WISEA J032934.05-524701.5 | G | 0.104842 ± 1.50e-4 |
| | S12 | 52.426 | -52.765 | GALEXASC J032942.20-524553.1 | UvS | – |
| | | | | WISEA J032942.27-524549.5 | VisS | – |

**Table 4.3:** Sources coincident with the radio contours in Figure 4.5. The source categories are galaxy (G), infrared source (IrS), ultraviolet source (UvS), and visual source (VisS). The fourth and twelfth radio peaks in the arc have two possible sources.

Only six of the eleven potential sources have redshifts, with the majority residing at redshifts $\sim 0.06$, which places them much closer than the J0330 cluster. A nearby cluster, Abell 3128, is close in projection to the objects' position and resides at a redshift of $z \sim 0.06$ (see Figure 4.1; Smith, 2003). At this redshift, the sources would have physical sizes of approximately 200 kpc (wedge) and 310 kpc (arc), significantly smaller than most cluster radio relics.

### 4.2.2 Galaxy density mapping

Abell 3128 has been identified as undergoing a line-of-sight merger with a galaxy group (Werner *et al.*, 2007). Evidence of strong environmental influence on the X-ray properties of cluster galaxies, also indicative of merger activity, is reported by Smith (2003). The disturbed nature of the cluster can be attributed to its location in the high-density environment of the Horologium-Reticulum supercluster (Werner *et al.*, 2007). If the wedge and arc are at a similar redshift to Abell 3128, they would reside in a high-density environment conducive to the formation of unusual radio galaxy morphologies.

Due to the lack of spectroscopic redshifts for the sources in the emission regions, we make use of photometric data to search for optical over-densities at the position of the wedge and arc. We generate multiple redshift density maps at redshift 'slices' using zFIELD,

selecting the DECaLS DR9 photometric database. The central redshifts of the maps are chosen as 0.08, 0.2, 0.4, 0.6, 0.8, 1.0, 1.2, 1.4. We set the integration bounds of $dz = 0.02$ for the $z = 0.08$ map and $dz = 0.1$ for the remaining maps. The lowest redshift is chosen to ensure overlap with the redshift of the optical sources and Abell 3128. The complete set of redshift density maps and their corresponding error maps are presented in Appendix C. In Figure 4.6, we present the redshift map at $z = 0.08$, which overlaps with the redshift of Abell 3128, and at $z = 0.4$ which corresponds to the redshift of J0330. No overdensities visibly overlap with the emission in the $z = 0.4$ map. Two faint density peaks are visible in the $z = 0.08$ map, with one overlapping with the arc and the other offset by approximately 4 arcminutes (∼390 kpc at $z = 0.08$.) from the wedge. The uncertainties on the maps at redshift extremes are significant. However, the detection of faint density peaks at low redshift suggests the possibility that these structures are associated with a subcluster component of Abell 3128.

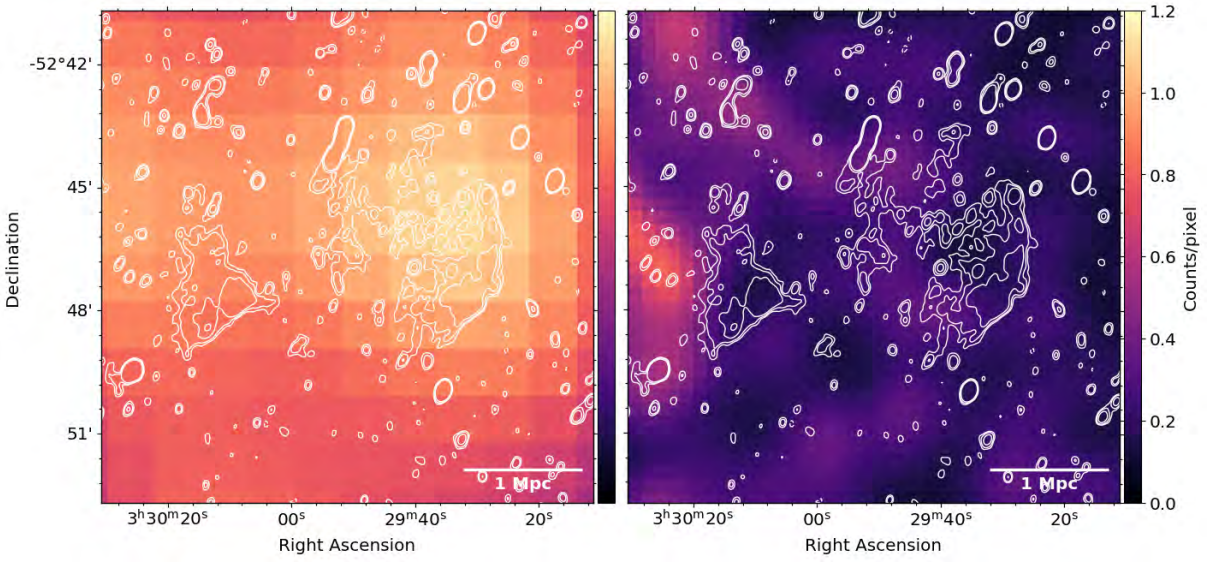


**Figure 4.6:** Comparison of the redshift slices at $z = 0.08$ and $z = 0.4$. The error maps are presented in Appendix C.

## 4.3 Origin

### 4.3.1 Cluster-scale emission

On first inspection, these objects appeared to be cluster radio relics. Both objects display a sharp, shock-like edge and trailing emission on the opposite side. The objects appeared similar to those studied by Stuardi *et al.* (2019) who investigate double radio relics discovered in the galaxy cluster RXC J1314.4 − 2515. Stuardi *et al.* (2019) make use of spectral and polarimetric studies to uncover the complex interactions between one of the radio relics and a cluster member. If one or both of our objects are radio relics, we would expect to see the characteristic spectral steepening in Figure 4.4. The wedge shows a spectral steepening along the top edge of the structure with a flatter spectral index ($\sim -0.4$) at the corner radio peak which steepens to $\sim -1.2$ in the $5\sigma$ region. The map uncertainties are high in this portion of the map however. The arc does not display an obvious spectral gradient along its width or length as would be expected for a radio relic.

As with radio halos, radio relics typically have X-ray counterparts that can aid in their identification. We search for X-ray emission in the archival *eROSITA*, *Chandra*, and *XMM-Newton* images. The *eROSITA* and *XMM-Newton* images are presented in Figure 4.7. We present the *XMM-Newton* and *eROSITA* images as the *Chandra* observation was shorter than the *XMM-Newton* one and observed the same region of sky. The *eROSITA* image is much shallower than the other observations but covers a wider area. If either of the structures are radio relics, we would expect to see X-ray shocks coinciding with the radio contours in Figure 4.7. In the *XMM-Newton* observation, the wedge and arc lie at the edge of the X-ray pointing, with no visible shocks. Similarly, the *eROSITA* image shows no evidence of shocks.

If the wedge and arc are both radio relics, it is highly improbable that they were generated in the same direction, as radio relics typically form on opposite sides of a cluster during a binary merger and travel away from each other. Both structures, however, appear to be

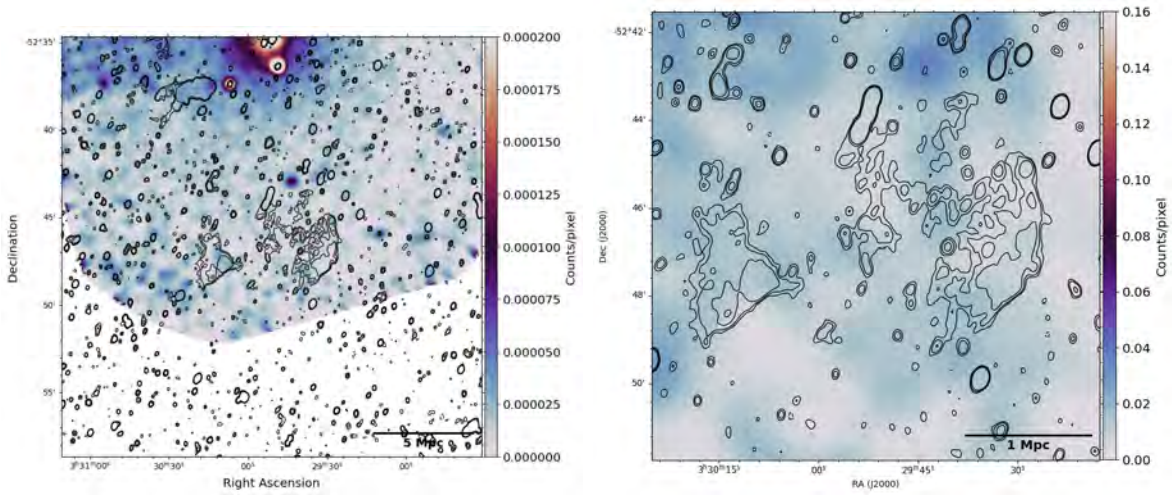


**Figure 4.7:** *Left: XMM-Newton* image with an exposure time of 71.91 ks Smith (2003). *Right: eROSITA* archival image with an exposure time of $\sim 150 - 200$ s. In the *XMM-Newton* image, part of Abell 3128 is visible at the top of the image.

moving westward, characterized by their sharp western fronts. This is inconsistent with the typical behaviour of binary merger shocks, as illustrated in Figure 1.7 in Chapter 1, where relics are related to opposing, outward-moving shocks. There have been cases where "wrong-way" relics have been discovered (e.g. Botteon *et al.*, 2021) where the relic appears bent in the opposite direction to conventional radio relics and shows an atypical spectral index distribution (Böss *et al.*, 2023). One theory is that the "wrong-way" relics form when a shock wave travelling outward from a cluster is bent inwards by an in-falling galaxy cluster or group (Böss *et al.*, 2023). One possibility is that one structure is a relic and the other a "wrong-way" relic but there is no documented cluster close to the structures that could be their point of origin and no obvious infalling clusters or groups that could cause the "wrong-way" relic behaviour.

Although the wedge and arc are close together in projection, this proximity diminishes the likelihood of them being a pair of radio relics. Projection effects could make them appear closer than they are in physical space. The morphology of the arc strongly resembles that of a radio relic: a distinct arc shape with a sharp western edge and diffuse emission trailing westward, consistent with shock fronts propagating through the ICM.

In contrast, if the wedge is a radio relic, it would need to be viewed edge-on, with its length projected onto the plane of the sky. Such an orientation would compress its elongated

structure into a smaller, central region, potentially giving the illusion of a localized source. In the DES optical image, there are no visible sources coincident with this peak. Our NED search of the peak position revealed an infrared source which could be the origin of the emission, or just viewed in projection. This source may lie at a redshift beyond $z = 1$, given the DES DR2 $i$-band magnitude limit. We also detect no over-densities at this position in the $z$ =1.0, 1.2 and 1.4 redshift density slices.

When considered together, the relative orientations of the wedge and arc make it unlikely that the two structures are physically related as part of the same event or process. Of the two structures, the wedge is more likely to be cluster-related emission. It is the only structure that shows a spectral gradient and has no obvious optical counterpart at its peak.

### 4.3.2 Galaxy-scale emission

Another possibility is that the structures are associated with individual galaxies. The wedge morphology bears some resemblance to that of a poorly resolved wide-angle tail (WAT) galaxy. WATs are formed when a jetted radio galaxy moves through a dense medium, such as during infall into a cluster, causing the jets to undergo ram-pressure stripping (see O Dea and Baum, 2023 for a review). These interactions often result in complex jet morphologies. The L-band MeerKAT image does not resolve any jets emanating from the western radio peak that would fit this scenario (see Figure 4.8). The sources on the eastern corner of the wedge are better resolved in the L-band image; three distinct radio peaks are visible in that area which likely correspond to S2, S3, and a fainter optical source visible to the east as seen in Figure 4.5. These sources might just be visible in projection, forming one side of the wedge's triangular shape, and not physically related to the western radio peak.

An alternative possibility is that the wedge's radio peak corresponds to a hotspot in a radio galaxy jet. Fanaroff-Riley type II (FR II) galaxies often exhibit radio jets terminating in bright hotspots (Fanaroff and Riley, 1974). The absence of a second visible jet could be attributed to projection effects, where the second jet is folded behind the one in direct

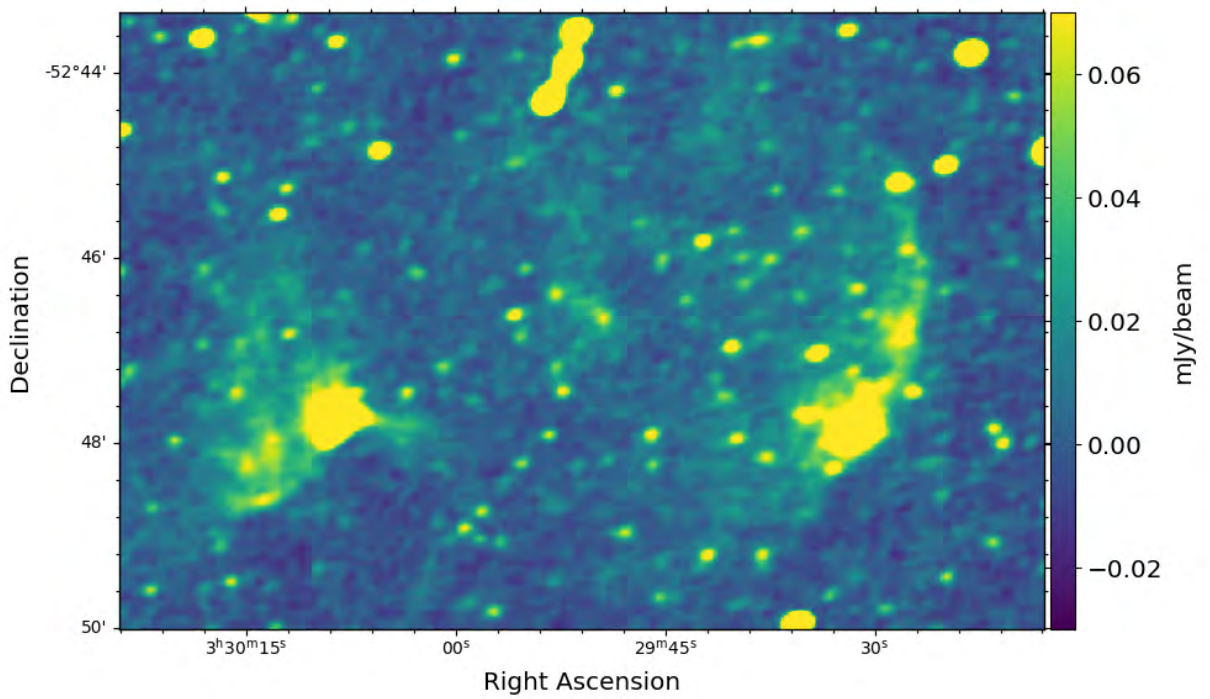


**Figure 4.8:** Close-up of the wedge and arc in the L-band MeerKAT image.

line-of-sight. The host galaxy in this scenario could be the elliptical galaxy in the eastern corner of the wedge (S2 in Figure 4.5). If this is the case, the flat edge observed along the bottom of the wedge might result from the jet interacting with a significantly denser medium. In the L-band image, there are no clearly resolved jets emanating from S2, however, high levels of turbulence could obscure the faint jets connecting the host galaxy to the bright spots. This would explain why the western peak has no visible counterpart in the DES image.

The large, diffuse extent of the arc results in several galaxies appearing spatially coincident with various parts of the structure. Galaxies with a wide variety of colours (and therefore redshifts) are visible; with those of interest labelled in Figure 4.5. Due to two-dimensional projection effects, it is challenging to determine whether these galaxies are physically embedded in the diffuse structure or merely superimposed along the line of sight. Majority of the candidate sources labelled in Figure 4.5 that have spectroscopic redshifts, reside at around $z = 0.06$, close to Abell 3128.

The radio contours in Figure 4.5 reveal faint emission connecting the arc and sources to

the east. A possibility is that the arc is a bent radio jet emanating from one of those sources. S12 in Figure 4.5 sits at the perfect distance between the arc and the fainter diffuse structure to the east and could be a host for this scenario. Two sources are detected in this region, neither of which have spectroscopic redshifts. The optical density slice at $z = 0.8$ (see Figure C.3 in Appendix C) shows an over-density at this position. At this redshift, the arc would have a physical size of $\sim 1.9$ Mpc and the fainter jet $\sim 1.0$ Mpc. If the arc does reside at this redshift, there are no documented clusters that could be the source of the turbulence needed to form the bent-jet morphology.

The arc could potentially be related to S4, en elliptical galaxy at the northernmost part of the arc, which coincides with the optical density peak at $z = 0.08$ (see Figure 4.6. The fainter emission extending eastward between S4 and S12 could be the second jet. The difference in size could be attributed to interactions with the ICM of Abell 3128. Turbulence from interactions within the Abell 3128 cluster could cause the jets of a radio galaxy to be swept back at odd angles, while also providing the energy necessary to re-energise the jet electrons. A possible explanation for the arc's shape and brightness could be that turbulence from this interaction may have re-accelerated particles from one of the jets causing it to appear larger and brighter than its counterpart.

Another mechanism that could possibly be contributing to both structures is the jellyfish scenario whereby strong ram pressure stripping causes trailing tails of stripped gas from the outer disks of spiral galaxies (Fumagalli *et al.*, 2014, Bellhouse *et al.*, 2017, Poggianti *et al.*, 2017, Ignesti *et al.*, 2023). These galaxies typically have debris, visible in the optical or UV bands, trailing beyond the stellar disk and kpc-long tails of ionised gas (Ignesti *et al.*, 2023). In some cases, these galaxies show radio emission extending tens of kpc from the stellar disk (e.g. Gavazzi and Jaffe, 1987, Ignesti *et al.*, 2022a, Roberts *et al.*, 2022). The radio tails have been found to be steep spectrum ($\alpha < -0.9$) at GHz frequencies close to the galaxy disk (Ignesti *et al.*, 2022b, Venturi *et al.*, 2022).

In Figure 4.3, there are three spiral galaxies which could fit into this scenario. Source S2 (coincident with the wedge; see Figure 4.5) appears to be a spiral galaxy, however, this position in the spectral index map (Figure 4.4) shows a flatter spectrum than what is

expected for jellyfish galaxies ($\alpha < -0.9$). The radio emission also does not form a clear trail emanating from the source like the sources presented by Ignesti *et al.* (2023). The lack of trailing radio emission could however be an indication of strong turbulence which might disrupt the trailing emission, creating unusual morphologies.

Sources S8 and S11 (coincident with the arc; see Figure 4.5) could be spiral galaxies. The radio contours in Figure 4.5 show a slight elongation in the northwestern direction, potentially extending out from S11. For S8, however, the radio contours do not show an obvious elongation in any direction. Due to the large extent of the wedge and arc, other sources coincident with the structures could be contributing to the emission seen in Figure 4.2. Some of this emission may stem from jellyfish galaxies but both structures are too large (based on the redshifts listed in Table 4.3) to result from the jellyfish scenario alone.

## 4.4 Conclusions

Based on the analyses presented in this chapter, the wedge and arc exhibit many characteristics consistent with AGN-driven emission. The wedge structure displays a spectral gradient along its northern edge, typical of a cluster radio relic, but has no visible X-ray counterpart. No significant over-densities are observed for the wedge at redshifts that would correspond to the large physical sizes expected for radio relics. The arc displays no obvious spectral index gradient across its width or length and also lacks an X-ray counterpart. We detect an over-density at $z = 0.8$ at the position of S12 but find no clusters at this redshift which could be responsible for the disturbed radio morphology of the arc. We propose that the arc was shaped by interactions between AGN jets and the disturbed ICM of Abell 3128. Turbulence from the on-going cluster-group merger in Abell 3128 has likely bent the radio jets into their unusual morphologies and re-accelerated portions of the emission, producing a structure that superficially mimics that of cluster radio relics. For the wedge, we propose two very different formation scenarios, one where the structure is cluster-related and another where the structure is AGN-related. These findings underscore the complex interplay between AGN emission and environmental conditions

in dynamically disturbed clusters, highlighting the need for multiwavelength observations and further modelling to fully understand these enigmatic structures.

# Chapter 5

# Conclusion and Future Work

In this thesis, the dynamic environments of three Sunyaev-Zel'dovich detected galaxy clusters were investigated with particular focus on diffuse radio emission. We made use of observations from the MeerKAT (1.2 GHz and 0.8 GHz) and JVLA (1.5 GHz) telescopes, calibrated using the CARACal and VLA Calibration and Imaging pipelines respectively. The astrometry and fluxscale of the final self calibrated images were verified, and based on these results, the MeerKAT images were used to test four methods of compact source subtraction. Our findings revealed that the image-plane subtraction methods yield satisfactory results when compared to the widely used visibility-plane subtraction procedures. This finding is especially valuable given that original visibility data is not always readily available. For short observations, both the image-plane and 2GC-subtraction methods performed well, introducing minimal uncertainty into the subtracted image, offering practical solutions for effective image processing when uv-cuts cannot be applied to the data.

Using our source subtracted images, we confirmed the presence of previously detected radio halos in two of the clusters: ACT-CL J0034+0225 and ACT-CL J0137-0827. The third cluster, ACT-CL J0330-5228, was identified as a candidate to host a radio halo. Integrated flux densities for the emission in each cluster were measured in the source subtracted images, along with integrated spectral indices for the clusters hosting radio halos, using complementary GMRT images. Morphological comparisons between the radio emission and archival X-ray images were performed to investigate whether the radio

emission arises from merger activity or galaxy-scale processes. For ACT-CL J0034+0225 and ACT-CL J0137-0827, the radio and X-ray emissions exhibited similar morphologies, consistent with merger-induced emission. In contrast, the X-ray emission in ACT-CL J0330-5228 did not match the elongated radio emission at the cluster centre. To further explore the origin of this emission, we searched for nearby radio galaxies contributing electrons to the central regions and investigated the spectral index distribution of cluster members visible in the MeerKAT and GMRT images. The predominance of flat-spectrum sources near the cluster centres suggests on-going activity in the cluster environments, indicating that merger activity in these clusters is recent or in an early stage. This result was confirmed by the dynamical state analyses performed using optical density maps.

Additionally, we investigated serendipitous diffuse radio emission discovered in the ACT-CL J0330-5228 field using archival multiwavelength data along with newly observed MeerKAT data. In-band and wide-band spectral index maps produced using the UHF- and L-band MeerKAT data revealed a spectral gradient along the edge of one of the structures, a typical feature of cluster radio relics. The integrated spectral indices for both structures were consistent with those of documented radio relics and AGN-driven emission. Optical density maps were generated at multiple redshifts to identify optical over-densities and determine the redshift of the structures. Over-densities are found at two different redshifts, leading to two possible explanations for the origin of each structure. Archival X-ray data was examined to search for corresponding shocks, and optical images were examined to identify potential sources or counterparts. Based on these analyses, one structure was proposed to have been shaped by interactions between a jetted radio galaxy and the disturbed ICM of Abell 3128, while the other may be cluster-related or galaxy-related.

## 5.1 Future work

The results presented in this thesis highlight the importance of combining high-resolution radio observations with multiwavelength data to unravel the complexities of diffuse emission in galaxy clusters. Multiwavelength studies offer a holistic view of cluster dynamics,

linking large-scale processes, such as mergers, with smaller-scale interactions involving AGN and the ICM. Such integrated approaches are essential for advancing our understanding of the physics driving large-scale structure formation.

The galaxy clusters in this study were all observed as part of the MeerKAT Exploration of Relics, Giant Halos, and Extragalactic Radio Sources (MERGHERS) survey (Knowles *et al.*, 2016). While the methodologies developed and applied in this study focus on a small sample, they can be extended to the larger MERGHERS pilot survey, which includes short observations (0.2–2.1 hours) of 13 massive SZ-detected galaxy clusters (Knowles *et al.*, 2021), and the upcoming tier 1 and 2 surveys (Knowles, 2024). Investigating the viability of image-plane subtraction methods, such as inpainting and filtering, and visibility-plane 2GC-subtraction across this broader sample could enhance the effectiveness of short survey observations and provide insights into the limitations of these procedures. This is particularly important for maximizing the science yield of time-limited surveys conducted with the MeerKAT telescope.

Applying the dynamical state analyses to the full MERGHERS sample could aid in classifying and comparing relaxed versus disturbed clusters when considering targets for follow-up observations. Broader spectral data of these galaxy clusters would enable spectral index mapping and spectral ageing analyses of the radio halos in ACT-CL J0034+0225, ACT-CL J0137-0827, and the elongated emission in ACT-CL J0330-5228. This would also allow the identification of more cluster members and a deeper analysis of the spectral properties of these members.

Applying the visibility- and image-plane source subtraction procedures to the new L-band MeerKAT data could enhance image sensitivity to diffuse emission. This, in turn, could improve the signal to noise ratio of the emission discovered south of ACT-CL J0330-5228 and reduce the spectral index uncertainties in the faintest parts of the emission in the wide-band spectral index map.

Future spectroscopic observations of sources embedded in the emission will help distinguish genuine contributors from those coincident due to projection effects. These observations would provide spectroscopic redshifts, enabling the identification of both the

origin of the emission and the turbulence driving the disturbed morphology of the structures. Additionally, gradient-filtering edge-detection methods, such as those applied by Botteon *et al.* (2023), could be employed to study the sharp edges along the western side of the structures, potentially uncovering any underlying substructure. Furthermore, radio observations spanning a broader range of frequencies could help characterize the spectral energy distribution of these structures, while a spectral ageing analysis might reveal whether they originated during the same epoch.

# References

**Abazajian, K., Adelman-McCarthy, J. K., Ageros, M. A.** *et al.* The First Data Release of the Sloan Digital Sky Survey. *The Astronomical Journal*, 126(4):2081–2086, October 2003. ISSN 1538-3881. doi:10.1086/378165.

**Ackermann, M., Ajello, M., Albert, A.** *et al.* Search for Gamma-Ray Emission from the Coma Cluster with Six Years of Fermi-LAT Data. *Astrophysical Journal*, 819(2):149, March 2016. doi:10.3847/0004-637X/819/2/149.

**Adam, R., Goksu, H., Brown, S.** *et al.* Gamma-ray detection toward the Coma cluster with Fermi-LAT: Implications for the cosmic ray content in the hadronic scenario. *Astronomy & Astrophysics*, 648:A60, April 2021. ISSN 1432-0746. doi:10.1051/0004-6361/202039660.

**Ade, P. A. R., Aghanim, N., Arnaud, M.** *et al.* Planck2015 results: XXVII. The second Planck catalogue of Sunyaev-Zeldovich sources. *Astronomy & Astrophysics*, 594:A27, September 2016. ISSN 1432-0746.

**Akamatsu, H., van Weeren, R. J., Ogrean, G. A.** *et al.* SuzakuX-ray study of the double radio relic galaxy cluster CIZA J2242.8+5301. *Astronomy & Astrophysics*, 582:A87, October 2015. ISSN 1432-0746. doi:10.1051/0004-6361/201425209.

**Andrade-Santos, F., Jones, C., Forman, W. R.** *et al.* The Fraction of Cool-core Clusters in X-Ray versus SZ Samples Using Chandra Observations. *Astrophysical Journal*, 843(1):76, July 2017. doi:10.3847/1538-4357/aa7461.

**Bean, B., Bhatnagar, S., Castro, S.** *et al.* CASA, Common Astronomy Software

Applications for Radio Astronomy. *Publications of the Astronomical Society of the Pacific*, 134(1041):114501, 2022.

**Becker, R. H., White, R. L., and Helfand, D. J.** The FIRST Survey: Faint Images of the Radio Sky at Twenty Centimeters. *Astrophysical Journal*, 450:559, September 1995. doi:10.1086/176166.

**Bellhouse, C., Jaffé, Y. L., Hau, G. K. T., and McGee**. GASP. II. A MUSE View of Extreme Ram-Pressure Stripping along the Line of Sight: Kinematics of the Jellyfish Galaxy JO201. *Astrophysical Journal*, 844(1):49, July 2017. doi:10.3847/1538-4357/aa7875.

**Benson, B., SPT, T., SPTpol** *et al.* The South Pole Telescope Cluster Survey. In *American Astronomical Society Meeting Abstracts #223*, volume 223 of *American Astronomical Society Meeting Abstracts*, page 135.02. January 2014.

**Bernardi, G., Venturi, T., Cassano, R.** *et al.* KAT-7 observations of an unbiased sample of mass-selected galaxy clusters. *Monthly Notices of the Royal Astronomical Society*, 456(2):1259–1268, December 2015. ISSN 0035-8711. doi:10.1093/mnras/stv2589.

**Birkinshaw, M., Gull, S. F., and Hardebeck, H.** The Sunyaev–Zeldovich effect towards three clusters of galaxies. *Nature*, 309(5963):34–35, May 1984. ISSN 1476-4687. doi:10.1038/309034a0. Number: 5963 Publisher: Nature Publishing Group.

**Blandford, R. and Eichler, D.** Particle acceleration at astrophysical shocks: A theory of cosmic ray origin. *Physics Reports*, 154(1):1–75, 1987. Publisher: Elsevier.

**Blumenthal, G. R., Faber, S., Primack, J. R.** *et al.* Formation of galaxies and large-scale structure with cold dark matter. *Nature*, 311(5986):517–525, 1984. Publisher: Nature Publishing Group UK London.

**Bonafede, A., Brüggen, M., van Weeren, R.** *et al.* Discovery of radio haloes and double relics in distant MACS galaxy clusters: clues to the efficiency of particle acceler-

ation. *Monthly Notices of the Royal Astronomical Society*, 426(1):40–56, October 2012. doi:10.1111/j.1365-2966.2012.21570.x.

**Bonafede, A., Brunetti, G., Rudnick, L.** *et al.* The Coma Cluster at LOFAR Frequencies. II. The Halo, Relic, and a New Accretion Relic. *The Astrophysical Journal*, 933(2):218, July 2022. doi:10.3847/1538-4357/ac721d.

**Bonafede, A., Feretti, L., Giovannini, G.** *et al.* Revealing the magnetic field in a distant galaxy cluster: discovery of the complex radio emission from MACS J0717.5 +3745. *Astronomy & Astrophysics*, 503(3):707–720, September 2009. doi:10.1051/0004-6361/200912520.

**Bonafede, A., Intema, H. T., Brüggen, M.** *et al.* A giant radio halo in the cool core cluster CL1821+643. *Monthly Notices of the Royal Astronomical Society: Letters*, 444(1):L44–L48, August 2014. ISSN 1745-3925. doi:10.1093/mnrasl/slu110.

**Bonafede, A., Vazza, F., Bruggen, M.** *et al.* Measurements and simulation of Faraday rotation across the Coma radio relic. *Monthly Notices of the Royal Astronomical Society*, 433(4):3208–3226, June 2013. ISSN 1365-2966. doi:10.1093/mnras/stt960.

**Bond, J. R., Szalay, A. S., and Turner, M. S.** Formation of Galaxies in a Gravitino-Dominated Universe. *Physical Review Letters*, 48:1636–1639, June 1982. doi:10.1103/PhysRevLett.48.1636.

**Botteon, A., Cassano, R., van Weeren, R. J.** *et al.* Discovery of a Radio Halo (and Relic) in a $M_{500} < 2 \times 10^{14}$ $M_{\odot}$ Cluster. *The Astrophysical Journal Letters*, 914(2):L29, June 2021. doi:10.3847/2041-8213/ac0636.

**Botteon, A., Markevitch, M., van Weeren, R. J.** *et al.* Surface brightness discontinuities in radio halos. Insights from the MeerKAT Galaxy Cluster Legacy Survey. *Astronomy & Astrophysics*, 674:A53, June 2023. doi:10.1051/0004-6361/202346150.

**Botteon, A., Shimwell, T. W., Cassano, R., Cuciti, V., and Zhang, X.** The Planck clusters in the LOFAR sky. I. LoTSS-DR2: New detections and sample overview. *Astronomy & Astrophysics*, 660:A78, April 2022. doi:10.1051/0004-6361/202143020.

**Bridle, A. H. and Greisen, E. W.** The NRAO AIPS project–a summary. *National Radio Astronomy Observatory, Charlottesville, Virginia, USA*, 1994.

**Briggs, D. S.** High Fidelity Interferometric Imaging: Robust Weighting and NNLS Deconvolution. In *American Astronomical Society Meeting Abstracts*, volume 187 of *American Astronomical Society Meeting Abstracts*, page 112.02. December 1995.

**Brown, S. and Rudnick, L.** Diffuse radio emission in/around the Coma cluster: beyond simple accretion. *Monthly Notices of the Royal Astronomical Society*, 412(1):2–12, March 2011. doi:10.1111/j.1365-2966.2010.17738.x.

**Brunetti, G. and Blasi, P.** Alfvénic reacceleration of relativistic particles in galaxy clusters in the presence of secondary electrons and positrons. *Monthly Notices of the Royal Astronomical Society*, 363(4):1173–1187, November 2005. ISSN 0035-8711. doi: 10.1111/j.1365-2966.2005.09511.x.

**Brunetti, G., Giacintucci, S., Cassano, R.** *et al.* A low-frequency radio halo associated with a cluster of galaxies. *Nature*, 455(7215):944–947, October 2008. doi: 10.1038/nature07379.

**Brunetti, G. and Jones, T. W.** Cosmic Rays in Galaxy Clusters and Their Nonthermal Emission. *International Journal of Modern Physics D*, 23(4):1430007-98, March 2014. doi:10.1142/S0218271814300079.

**Brunetti, G. and Lazarian, A.** Acceleration of primary and secondary particles in galaxy clusters by compressible MHD turbulence: from radio haloes to gamma-rays. *Monthly Notices of the Royal Astronomical Society*, 410(1):127–142, January 2011. doi: 10.1111/j.1365-2966.2010.17457.x.

**Brunetti, G., Setti, G., Feretti, L.** *et al.* Particle reacceleration in the Coma cluster: radio properties and hard X-ray emission. *Monthly Notices of the Royal Astronomical Society*, 320(3):365–378, 01 2001. ISSN 0035-8711. doi:10.1046/j.1365-8711.2001.03978.x.

**Brunetti, G., Venturi, T., Dallacasa, D.** *et al.* Cosmic Rays and Radio Halos in Galaxy Clusters: New Constraints from Radio Observations. *The Astrophysical Journal*, 670(1):L5–L8, October 2007. doi:10.1086/524037. Publisher: American Astronomical Society.

**Brunner, R. J. and Lubin, L. M.** A Probabilistic Quantification of Galaxy Cluster Membership. *The Astronomical Journal*, 120(6):2851, December 2000. doi:10.1086/316849.

**Buote, D. A.** On The Origin of Radio Halos in Galaxy Clusters. *The Astrophysical Journal*, 553(1):L15–L18, May 2001. ISSN 0004637X. doi:10.1086/320500. ArXiv:astro-ph/0104211.

**Böss, L. M., Steinwandel, U. P., and Dolag, K.** A Formation Mechanism for "Wrong Way" Radio Relics. *The Astrophysical Journal Letters*, 957(2):L16, November 2023. ISSN 2041-8213. doi:10.3847/2041-8213/ad03f7.

**Carilli, C. L. and Taylor, G. B.** Cluster Magnetic Fields. *Annual Review of Astronomy & Astrophysics*, 40(Volume 40, 2002):319–348, 2002. ISSN 1545-4282. doi:https://doi.org/10.1146/annurev.astro.40.060401.093852.

**Cassano, R. and Brunetti, G.** Cluster mergers and non-thermal phenomena: a statistical magneto-turbulent model. *Monthly Notices of the Royal Astronomical Society*, 357(4):1313–1329, 03 2005. ISSN 0035-8711. doi:10.1111/j.1365-2966.2005.08747.x.

**Cassano, R., Brunetti, G., Röttgering, H. J. A.** *et al.* Unveiling radio halos in galaxy clusters in the LOFAR era. *Astronomy & Astrophysics*, 509:A68, November 2009. ISSN 1432-0746. doi:10.1051/0004-6361/200913063.

**Cassano, R., Ettori, S., Brunetti, G.** *et al.* Revisiting Scaling Relations for Giant Radio Halos in Galaxy Clusters. *The Astrophysical Journal*, 777(2):141, October 2013. ISSN 1538-4357. doi:10.1088/0004-637x/777/2/141.

**Cassano, R., Ettori, S., Giacintucci, S.** *et al.* On the connection between giant radio

halos and cluster mergers. *Astrophysical Journal*, 721(2):L82–L85, October 2010. ISSN 2041-8205, 2041-8213. doi:10.1088/2041-8205/721/2/L82. ArXiv:1008.3624 [astro-ph].

**Cassano, R., Gitti, M., and Brunetti, G.** A morphological comparison between giant radio halos and radio mini–halos in galaxy clusters. *Astronomy & Astrophysics*, 486:L31, 2008. doi:10.1051/0004-6361:200810179.

**Chambers, K. C., Magnier, E. A., Metcalfe, N.** *et al.* The Pan-STARRS1 Surveys. *arXiv e-prints*, arXiv:1612.05560, December 2016. doi:10.48550/arXiv.1612.05560.

**Chu, A., Durret, F., and Márquez, I.** Physical properties of brightest cluster galaxies up to redshift 1.80 based on HST data. *Astronomy & Astrophysics*, 649:A42, May 2021. doi:10.1051/0004-6361/202040245.

**Clarke, B. G.** "Coherence in Radio Astronomy". In *Synthesis Imaging in Radio Astronomy II*, volume 180 of *Astronomical Society of the Pacific Conference Series*, pages 1–9. January 1999.

**Clarke, T., Mroczkowski, T., Brown, S.** *et al.* White Paper: Radio Emission and Polarization Properties of Galaxy Clusters with VLASS. *arXiv e-prints*, arXiv:1401.0329, January 2014. doi:10.48550/arXiv.1401.0329.

**Clarke, T. E. and Ensslin, T. A.** Deep 1.4 GHz Very Large Array Observations of the Radio Halo and Relic in Abell 2256. *Astronomical Journal*, 131(6):2900–2912, June 2006. doi:10.1086/504076.

**Condon, J. J., Cotton, W. D., Greisen, E. W.** *et al.* The NRAO VLA Sky Survey. In *American Astronomical Society Meeting Abstracts*, volume 183 of *American Astronomical Society Meeting Abstracts*, page 64.02. December 1993.

**Condon, J. J., Cotton, W. D., Greisen, E. W.** *et al.* The NRAO VLA Sky Survey. *Astronomical Journal*, 115(5):1693–1716, May 1998. doi:10.1086/300337.

**Condon, J. J. and Ransom, S. M.** Essential Radio Astronomy, volume 2. Princeton University Press, 2016.

**Conselice, C. J., Bershady, M. A., and Jangren, A.** The Asymmetry of Galaxies: Physical Morphology for Nearby and High-Redshift Galaxies. *The Astrophysical Journal*, 529(2):886–910, February 2000. ISSN 1538-4357. doi:10.1086/308300.

**Cornwell, T. J. and Perley, R. A.** Radio-interferometric imaging of very large fields. The problem of non-coplanar arrays. *Astronomy & Astrophysics*, 261:353–364, July 1992.

**Cuciti, V., Cassano, R., Brunetti, G.** *et al.* Occurrence of radio halos in galaxy clusters. Insight from a mass-selected sample. *Astronomy & Astrophysics*, 580:A97, August 2015. doi:10.1051/0004-6361/201526420.

**Cuciti, V., Cassano, R., Brunetti, G.** *et al.* Radio halos in a mass-selected sample of 75 galaxy clusters: II. Statistical analysis. *Astronomy & Astrophysics*, 647:A51, March 2021. ISSN 1432-0746. doi:10.1051/0004-6361/202039208.

**Dark Energy Survey Collaboration, Abbott, T., Abdalla, F. B.** *et al.* The Dark Energy Survey: more than dark energy - an overview. *Monthly Notices of the Royal Astronomical Society*, 460(2):1270–1299, August 2016. doi:10.1093/mnras/stw641.

**Datta, R., Aiola, S., Choi, S. K.** *et al.* The Atacama Cosmology Telescope: two-season ACTPol extragalactic point sources and their polarization properties. *Monthly Notices of the Royal Astronomical Society*, 486(4):5239–5262, November 2018. doi:10.1093/mnras/sty2934.

**de Gasperin, F., Intema, H. T., Shimwell, T. W.** *et al.* Gentle reenergization of electrons in merging galaxy clusters. *Science Advances*, 3(10), October 2017. ISSN 2375-2548. doi:10.1126/sciadv.1701634.

**de Gasperin, F., van Weeren, R. J., Brüggen, M.** *et al.* A new double radio relic in PSZ1 G096.89+24.17 and a radio relic mass-luminosity relation. *Monthly Notices of the Royal Astronomical Society*, 444(4):3130–3138, November 2014. doi:10.1093/mnras/stu1658.

**de Gasperin, F.** *et al.* MeerKAT view of the diffuse radio sources in Abell 3667 and their interactions with the thermal plasma. *Astronomy Astrophysics*, 659:A146, 2022. doi:10.1051/0004-6361/202142658.

**Dey, A., Schlegel, D. J., Lang, D.** *et al.* Overview of the DESI Legacy Imaging Surveys. *Astronomical Journal*, 157(5):168, April 2019. ISSN 1538-3881. doi:10.3847/1538-3881/ab089d. ArXiv:1804.08657 [astro-ph].

**Di Gennaro, G., van Weeren, R. J., Cassano, R., and Brunetti, G.** A lofar-ugmrt spectral index study of distant radio halos. *Astronomy & Astrophysics*, 654:A166, October 2021. ISSN 1432-0746. doi:10.1051/0004-6361/202141510.
URL http://dx.doi.org/10.1051/0004-6361/202141510

**Di Gennaro, G., van Weeren, R. J., Hoeft, M.** *et al.* Deep Very Large Array Observations of the Merging Cluster CIZA J2242.8+5301: Continuum and Spectral Imaging. *Astrophysical Journal*, 865(1):24, September 2018. doi:10.3847/1538-4357/aad738.

**Di Mascolo, L., Mroczkowski, T., Churazov, E.** *et al.* An ALMA+ACA measurement of the shock in the Bullet Cluster. *Astronomy & Astrophysics*, 628:A100, August 2019.

**Di Mascolo, L., Mroczkowski, T., Perrott, Y.** *et al.* Multiwavelength view of SPT-CL J2106-5844: The radio galaxies and the thermal and relativistic plasmas in a massive galaxy cluster merger at $z \approx 1.13$. *Astronomy and Astrophysics*, 650:A153, June 2021. ISSN 0004-6361, 1432-0746. doi:10.1051/0004-6361/202040260.

**Doze, P., Hilton, M., Hughes, J. P.** *et al.* A Multiwavelength Approach to Constraining the Merger Properties of ACT-CL J0034.4+0225. *The Astrophysical Journal*, 974(1):49, October 2024. doi:10.3847/1538-4357/ad6442.

**D.S. Briggs, R. S., F.R. Schwab**. "Imaging". In *Synthesis Imaging in Radio Astronomy II*, volume 180 of *Astronomical Society of the Pacific Conference Series*, pages 127–148. January 1999.

**E.B. Formalont, R. P.** "Calibration and Editing". In *Synthesis Imaging in Radio Astronomy II*, volume 180 of *Astronomical Society of the Pacific Conference Series*, pages 79–109. January 1999.

**Enßlin, T., Pfrommer, C., Miniati, F.** *et al.* Cosmic ray transport in galaxy clusters: implications for radio halos, gamma-ray signatures, and cool core heating. *Astronomy & Astrophysics*, 527:A99, March 2011. doi:10.1051/0004-6361/201015652.

**Enßlin, T. A. and Gopal-Krishna**. Reviving fossil radio plasma in clusters of galaxies by adiabatic compression in environmental shock waves. *Astronomy & Astrophysics*, 366:26–34, January 2001. doi:10.1051/0004-6361:20000198.

**Fabian, A. C. and Nulsen, P. E. J.** Subsonic accretion of cooling gas in clusters of galaxies. *Monthly Notices of the Royal Astronomical Society*, 180:479–484, August 1977. doi:10.1093/mnras/180.3.479.

**Fanaroff, B. L. and Riley, J. M.** The morphology of extragalactic radio sources of high and low luminosity. *Monthly Notices of the Royal Astronomical Society*, 167:31P–36P, May 1974. doi:10.1093/mnras/167.1.31P.

**Feretti, L.** Observational Properties of Diffuse Halos in Clusters. 2000.

**Feretti, L., Giovannini, G., Govoni, F.** *et al.* Clusters of galaxies: observational properties of the diffuse radio emission. *Astron Astrophys Rev*, 20(1):54, May 2012. ISSN 1432-0754. doi:10.1007/s00159-012-0054-z.

**Ferramacho, L. D., Blanchard, A., and Zolnierowski, Y.** Constraints on CDM cosmology from galaxy power spectrum, CMB and SNIa evolution. *Astronomy & Astrophysics*, 499(1):21–29, May 2009. doi:10.1051/0004-6361/200810693.

**Ferrari, C., Govoni, F., Schindler, S.** *et al.* Observations of Extended Radio Emission in Clusters. *Space Science Reviews*, 134(1–4):93–118, February 2008. ISSN 1572-9672. doi:10.1007/s11214-008-9311-x.

**Finner, K., Jee, M. J., Golovich, N.** *et al.* MC$^2$: Subaru and Hubble Space Telescope Weak-lensing Analysis of the Double Radio Relic Galaxy Cluster PLCK G287.0+32.9. *Astrophysical Journal*, 851(1):46, December 2017. doi:10.3847/1538-4357/aa998c.

**Freedman, W. L. and Madore, B. F.** The Hubble Constant. *Annual Review of Astronomy & Astrophysics*, 48(Volume 48, 2010):673–710, 2010. ISSN 1545-4282. doi: https://doi.org/10.1146/annurev-astro-082708-101829.

**Fumagalli, M., Fossati, M., Hau, G. K. T., and Gavazzi, G.** Muse sneaks a peek at extreme ram-pressure stripping events – i. a kinematic study of the archetypal galaxy eso137001. *Monthly Notices of the Royal Astronomical Society*, 445(4):4335–4344, 11 2014. ISSN 0035-8711. doi:10.1093/mnras/stu2092.

**Gasperin, F., Intema, H., Weeren, R. V.** *et al.* A powerful double radio relic system discovered in PSZ1 G108.18-11.53: Evidence for a shock with non-uniform Mach number? *Monthly Notices of the Royal Astronomical Society*, 453:3483–3498, 2015. doi: 10.1093/mnras/stv1873.

**Gavazzi, G. and Jaffe, W.** 50 KPC radio trails behind irregular galaxies in A 1367. *Astronomy & Astrophysics*, 186:L1–L2, November 1987.

**Gendron-Marsolais, M., Hlavacek-Larrondo, J., van Weeren, R. J.** *et al.* Deep 230–470 MHz VLA observations of the mini-halo in the Perseus cluster. *Monthly Notices of the Royal Astronomical Society*, 469(4):3872–3880, August 2017. ISSN 0035-8711, 1365-2966. doi:10.1093/mnras/stx1042.

**Giacconi, R., Murray, S., Gursky, H.** *et al.* The Uhuru catalog of X-ray sources. *Astrophysical Journal*, 178:281–308, December 1972. doi:10.1086/151790.

**Giovannini, G., Cau, M., Bonafede, A.** *et al.* Diffuse radio sources in a statistically complete sample of high-redshift galaxy clusters. *Astronomy & Astrophysics*, 640:A108, August 2020. doi:10.1051/0004-6361/202038263.

**Giovannini, G., Feretti, L., and Stanghellini, C.** The Coma cluster radio source 1253+275, revisited. *Astrophysical Journal*, 252:528–537, December 1991.

**Giovannini, G., Feretti, L., Venturi, T.** *et al.* The Halo Radio Source Coma C and the Origin of Halo Sources. *Astrophysical Journal*, 406:399, April 1993. doi:10.1086/172451.

**Gitti, M., Ferrari, C., Domainko, W.** *et al.* Discovery of diffuse radio emission at the center of the most X-ray-luminous cluster RX J1347.5-1145. *Astronomy & Astrophysics*, 470(3):L25–L28, August 2007. doi:10.1051/0004-6361:20077658.

**Gitti, M., Tozzi, P., Brunetti, G.** *et al.* The SKA view of cool-core clusters: evolution of radio mini-halos and AGN feedback. In *Advancing Astrophysics with the Square Kilometre Array (AASKA14)*, page 76. April 2015. doi:10.22323/1.215.0076.

**Golovich, N., Dawson, W. A., Wittman, D. M.** *et al.* Merging Cluster Collaboration: A Panchromatic Atlas of Radio Relic Mergers. *Astrophysical Journal*, 882(1):69, September 2019. doi:10.3847/1538-4357/ab2f90.

**Golovich, N., van Weeren, R. J., Dawson, W. A.** *et al.* MC$^2$: Multiwavelength and Dynamical Analysis of the Merging Galaxy Cluster ZwCl 0008.8+5215: An Older and Less Massive Bullet Cluster. *Astrophysical Journal*, 838(2):110, April 2017. doi:10.3847/1538-4357/aa667f.

**Hale, C. L., Heywood, I., Jarvis, M. J.** *et al.* Mightee: the continuum survey data release 1. *Monthly Notices of the Royal Astronomical Society*, 536(3):2187–2211, November 2024. ISSN 0035-8711. doi:10.1093/mnras/stae2528.

**Hale, C. L.** *et al.* The Rapid ASKAP Continuum Survey Paper II: First Stokes I Source Catalogue Data Release. *Publications of the Astronomical Society of Australia*, 38:e058, 2021. doi:10.1017/pasa.2021.47.

**Harwood, J. J., Hardcastle, M. J., Croston, J. H.** *et al.* BRATS: Broadband Radio Astronomy ToolS. *Astrophysics Source Code Library*, record ascl:1806.025, June 2018.

**Henning, P. A.** 30.9 MHz Observations of the Radio Halo in the Coma Cluster of Galaxies. *Astronomical Journal*, 97:1561, June 1989. doi:10.1086/115097.

**Henriksen, M. J. and Mushotzky, R. F.** The X-Ray Spectrum of the Coma Cluster of Galaxies. *Astrophysical Journal*, 302:287, March 1986. doi:10.1086/163990.

**Heywood, I.** oxkat: Semi-automated imaging of MeerKAT observations. September 2020. Available at https://ui.adsabs.harvard.edu/abs/2020ascl.soft09003H.

**Hildebrandt, H., Wolf, C., and Benítez, N.** A blind test of photometric redshifts on ground-based data. *Astronomy & Astrophysics*, 480(3):703–714, March 2008.

**Hilton, M., Sifón, C., Naess, S.** *et al.* The Atacama Cosmology Telescope: A Catalog of >4000 Sunyaev–Zel'dovich Galaxy Clusters. *The Astrophysical Journal Supplement Series*, 253(1):3, February 2021. ISSN 1538-4365. doi:10.3847/1538-4365/abd023.

**Hoang, D. N., Shimwell, T. W., Osinga, E.** *et al.* LOFAR detection of a low-power radio halo in the galaxy cluster Abell 990. *Monthly Notices of the Royal Astronomical Society*, 501(1):576–586, November 2020. ISSN 0035-8711. doi:10.1093/mnras/staa3581.

**Högbom, J. A.** Aperture Synthesis with a Non-Regular Distribution of Interferometer Baselines. *Astronomy & Astrophysics Supplement*, 15:417, June 1974.

**Hogg, D. W., Cohen, J. G., Blandford, R.** *et al.* A Blind Test of Photometric Redshift Prediction. *The Astronomical Journal*, 115(4):1418–1422, April 1998. ISSN 0004-6256.

**Hugo, B. V., Perkins, S., Merry, B.** *et al.* Tricolour: An Optimized SumThreshold Flagger for MeerKAT. In **Ruiz, J. E., Pierfedereci, F., and Teuben, P.**, editors, *Astronomical Data Analysis Software and Systems XXX*, volume 532 of *Astronomical Society of the Pacific Conference Series*, page 541. July 2022. doi:10.48550/arXiv.2206.09179.

**Hurley-Walker, N., Callingham, J. R., Hancock, P. J.** *et al.* GaLactic and Extragalactic All-sky Murchison Widefield Array (GLEAM) survey - I. A low-frequency extragalactic catalogue. *Monthly Notices of the Royal Astronomical Society*, 464(1):1146–1167, January 2017a. doi:10.1093/mnras/stw2337.

**Hurley-Walker, N., Callingham, J. R., Hancock, P. J.** *et al.* GaLactic and Extragalactic All-sky Murchison Widefield Array (GLEAM) survey - I. A low-frequency extragalactic catalogue. *Monthly Notices of the RAS*, 464(1):1146–1167, January 2017b. doi:10.1093/mnras/stw2337.

**Ignesti, A., Vulcani, B., Botteon, A., and Poggianti, B.** Radio continuum tails in ram pressure-stripped spiral galaxies: Experimenting with a semi-empirical model in Abell 2255. *Astronomy & Astrophysics*, 675:A118, July 2023. doi:10.1051/0004-6361/202346517.

**Ignesti, A., Vulcani, B., and Poggianti, B. M.** Walk on the low side: Lofar explores the low-frequency radio emission of gasp jellyfish galaxies. *The Astrophysical Journal*, 937(2):58, sep 2022a. doi:10.3847/1538-4357/ac8cf6.
URL https://dx.doi.org/10.3847/1538-4357/ac8cf6

**Ignesti, A., Vulcani, B., Poggianti, B. M., Paladino, R., and Shimwell, T.** Gasp xxxviii: The lofar-meerkat-vla view on the nonthermal side of a jellyfish galaxy. *The Astrophysical Journal*, 924(2):64, jan 2022b. doi:10.3847/1538-4357/ac32ce.
URL https://dx.doi.org/10.3847/1538-4357/ac32ce

**Ilbert, O., Capak, P., Salvato, M.** *et al.* Cosmos Photometric Redshifts with 30-Bands for 2-deg$^2$. *Astrophysical Journal*, 690(2):1236–1249, January 2009.

**Intema, H. T., van der Tol, S., Cotton, W. D.** *et al.* Ionospheric calibration of low frequency radio interferometric observations using the peeling scheme. I. Method description and first results. *Astronomy & Astrophysics*, 501(3):1185–1205, July 2009. doi:10.1051/0004-6361/200811094.

**Isella, A.** Interferometry Basics: Caltech CASA Radio Analysis Workshop. URL: https://science.nrao.edu/opportunities/courses/casa-caltech-winter2012/Isella_Radio_Interferometry_Basics_Caltech2012.pdf, January 2011. [Online; accessed 09/2024].

**Jaffe, W. J. and Rudnick, L.** Observations at 610 MHz of radio halos in clusters of galaxies. *Astrophysical Journal*, 233:453–462, October 1979. doi:10.1086/157406.

**Jonas, J. and MeerKAT Team**. The MeerKAT Radio Telescope. In *MeerKAT Science: On the Pathway to the SKA*, page 1. January 2016. doi:10.22323/1.277.0001.

**Jones, R. C.** New calculus for the treatment of optical systems. I. Description and discussion of the calculus. *Journal of the Optical Society of America (1917-1983)*, 31(7):488, July 1941. doi:10.1364/JOSA.31.000488.

**Józsa, G. I. G., White, S. V., Thorat, K.** *et al.* MeerKATHI – an end-to-end data reduction pipeline for MeerKAT and other radio telescopes. 2020.

**Kale, R., Wik, D. R., Giacintucci, S.** *et al.* Discovery of a radio relic in the low mass, merging galaxy cluster PLCK G200.9-28.2. *Monthly Notices of the Royal Astronomical Society*, 472(1):940–948, August 2017. ISSN 1365-2966. doi:10.1093/mnras/stx2031.

**Kempner, J. C., Blanton, E. L., Clarke, T. E.** *et al.* Conference Note: A Taxonomy of Extended Radio Sources in Clusters of Galaxies. In **Reiprich, T., Kempner, J., and Soker, N.**, editors, *The Riddle of Cooling Flows in Galaxies and Clusters of galaxies*, page 335. January 2004. doi:10.48550/arXiv.astro-ph/0310263.

**Kenyon, J. S., Perkins, S., and Smirnov, O.** QuartiCal: Fast radio interferometric calibration. *Astrophysics Source Code Library*, record ascl:2305.006, May 2023.

**Kenyon, J. S., Smirnov, O. M., Grobler, T. L.** *et al.* cubical – fast radio interferometric calibration suite exploiting complex optimization. *Monthly Notices of the Royal Astronomical Society*, 478(2):2399–2415, May 2018. ISSN 1365-2966. doi:10.1093/mnras/sty1221.

**Kesebonye, K. C., Hilton, M., Knowles, K.** *et al.* The MeerKAT Galaxy Clusters Legacy Survey: star formation in massive clusters at $0.15 < z < 0.35$. *Monthly Notices of the Royal Astronomical Society*, 518(2):3004–3016, November 2022. ISSN 1365-2966. doi:10.1093/mnras/stac3293.

**Keshet, U.** Radio haloes and relics from extended cosmic-ray ion distributions with strong diffusion in galaxy clusters. *Monthly Notices of the Royal Astronomical Society*, 527(1):1194–1215, October 2023. ISSN 1365-2966. doi:10.1093/mnras/stad3154.

**Kierdorf, M., Beck, R., Hoeft, M.** *et al.* Relics in galaxy clusters at high radio frequencies. *Astronomy & Astrophysics*, 600, 2016. doi:10.1051/0004-6361/201629570.

**Knowles, K.** MERGHERS Tier 1 Data Release, 2024. In preparation.

**Knowles, K., Baker, A. J., Basu, K.** *et al.* MERGHERS: An SZ-selected cluster survey with MeerKAT. In *MeerKAT Science: On the Pathway to the SKA*, page 30. January 2016. doi:10.22323/1.277.0030.

**Knowles, K., Cotton, W. D., Rudnick, L.** *et al.* The MeerKAT Galaxy Cluster Legacy Survey: I. Survey Overview and Highlights. *Astronomy & Astrophysics*, 657:A56, January 2022. ISSN 1432-0746. doi:10.1051/0004-6361/202141488.

**Knowles, K., Intema, H. T., Baker, A. J.** *et al.* A giant radio halo in a low-mass SZ-selected galaxy cluster: ACT-CL J0256.5+0006. *Monthly Notices of the Royal Astronomical Society*, 459(4):4240–4258, April 2016. ISSN 1365-2966. doi:10.1093/mnras/stw795.

**Knowles, K., Pillay, D. S., Amodeo, S.** *et al.* MERGHERS pilot: MeerKAT discovery of diffuse emission in nine massive Sunyaev–Zel'dovich-selected galaxy clusters from ACT. *Monthly Notices of the Royal Astronomical Society*, 504(2):1749–1758, April 2021. ISSN 0035-8711, 1365-2966. doi:10.1093/mnras/stab939. Publisher: Oxford University Press.

**Kravtsov, A. V. and Borgani, S.** Formation of Galaxy Clusters. *Annual Review of Astronomy & Astrophysics*, 50(Volume 50, 2012):353–409, 2012. ISSN 1545-4282. doi:https://doi.org/10.1146/annurev-astro-081811-125502.

**Labidi, A.** What Is the Mach number? *Journal of Aviation/Aerospace Education & Research (JAAER)*, November 2019.

**Lindner, R. R., Baker, A. J., Hughes, J. P.** *et al.* The Radio Relics and Halo of El Gordo, a Massive z = 0.870 Cluster Merger. *Astrophysical Journal*, 786(1):49, May 2014. doi:10.1088/0004-637X/786/1/49.

**Loubser, S. I., Hoekstra, H., Babul, A.** *et al.* Diversity in the stellar velocity dispersion profiles of a large sample of brightest cluster galaxies z $\leq$ 0.3. *Monthly Notices of the Royal Astronomical Society*, 477:335–358, 2018. doi:10.1093/mnras/sty498.

**Lusetti, G., de Gasperin, F., Cuciti, V.** *et al.* Re-energization of AGN head–tail radio galaxies in the galaxy cluster ZwCl 0634.1+47474. *Monthly Notices of the Royal Astronomical Society*, 528(1):141–159, December 2023. ISSN 0035-8711. doi:10.1093/mnras/stad3962.

**Mandal, S., Intema, H. T., van Weeren, R. J.** *et al.* Revived fossil plasma sources in galaxy clusters. *Astronomy & Astrophysics*, 634:A4, February 2020. doi:10.1051/0004-6361/201936560.

**Martin, P., Riti, J.-B., and de Chambure, D.** Planck Telescope: optical design and verification. In **Warmbein, B.**, editor, *5th International Conference on Space Optics*, volume 554 of *ESA Special Publication*, pages 323–331. June 2004.

**Mathews, W. G. and Bregman, J. N.** Radiative accretion flow onto giant galaxies in clusters. *Astrophysical Journal*, 224:308–319, September 1978. doi:10.1086/156379.

**McConnell, D.** *et al.* The Rapid ASKAP Continuum Survey I: Design and first results. *Publications of the Astronomical Society of Australia*, 37:e048, 2020. doi:10.1017/pasa.2020.41.

**McNamara, B. R. and Nulsen, P. E. J.** Mechanical feedback from active galactic nuclei in galaxies, groups and clusters. *New Journal of Physics*, 14(5):055023, May 2012. doi:10.1088/1367-2630/14/5/055023.

**Mohan, N. and Rafferty, D.** PyBDSF: Python Blob Detection and Source Finder. *Astrophysics Source Code Library*, record ascl:1502.007, February 2015.

**Molnar, S. M. and Broadhurst, T.** Shocks and Tides Quantified in the "Sausage" Cluster, CIZA J2242.8+5301 Using N-body/Hydrodynamical Simulations. *Astrophysics Journal*, 841(1):46, May 2017. doi:10.3847/1538-4357/aa70a3.

**Monebhurrun, V.** Standard Definitions of Terms for Antennas and Radio Wave Propagation. In *2019 Antenna Measurement Techniques Association Symposium (AMTA)*, pages 1–2. IEEE, IEEE, 2019.

**Napier, P. J.** The Primary Antenna Elements. In *Synthesis Imaging in Radio Astronomy II*, volume 180 of *Astronomical Society of the Pacific Conference Series*, page 171. January 1999.

**Nascimento, R. S., Lopes, P. A. A., Ribeiro, A. L. B.** *et al.* The influence of the dynamic state of galaxy clusters on segregation phenomena and velocity dispersion profiles. *Monthly Notices of the Royal Astronomical Society: Letters*, 483(1):L121–L126, December 2018. ISSN 1745-3925. doi:10.1093/mnrasl/sly229.

**Newman, J. A. and Gruen, D.** Photometric Redshifts for Next-Generation Surveys. *Annual Review of Astronomy & Astrophysics*, 60(Volume 60, 2022):363–414, 2022. ISSN 1545-4282. doi:https://doi.org/10.1146/annurev-astro-032122-014611.

**Noordam, J. E.** LOFAR calibration challenges. In **Oschmann, J. M., Jr.**, editor, *Ground-based Telescopes*, volume 5489 of *Society of Photo-Optical Instrumentation Engineers (SPIE) Conference Series*, pages 817–825. October 2004. doi:10.1117/12.544262.

**Norris, R. P., Hopkins, A. M., Afonso, J.** *et al.* EMU: Evolutionary Map of the Universe. *Publications of the Astronomical Society of Australia*, 28(3):215–248, 2011. ISSN 1448-6083. doi:10.1071/as11021.

**NRAO**. Sensitivity — science.nrao.edu. URL: https://science.nrao.edu/facilities/vla/docs/manuals/oss/performance/sensitivity, 2024. [Accessed 17-01-2025].

**O Dea, C. P. and Baum, S. A.** Wide-Angle-Tail (WAT) Radio Sources. *Galaxies*, 11(3):67, May 2023. doi:10.3390/galaxies11030067.

**Offringa, A. R., de Bruyn, A. G., Zaroubi, S.** *et al.* A LOFAR RFI detection pipeline and its first results. *arXiv e-prints*, arXiv:1007.2089, July 2010. doi:10.48550/arXiv.1007.2089.

**Offringa, A. R., McKinley, B., Hurley-Walker, N.** *et al.* WSClean: an implementation of a fast, generic wide-field imager for radio astronomy. *Monthly Notices of the Royal Astronomical Society*, 444(1):606–619, October 2014. ISSN 0035-8711, 1365-2966. doi:10.1093/mnras/stu1368.

**Okabe, N., Akamatsu, H., Kakuwa, J.** *et al.* Radio relics tracing the projected mass distribution in CIZA J2242.8+5301. *Publications of the Astronomical Society of Japan*, 67(6), September 2015. ISSN 0004-6264. doi:10.1093/pasj/psv085.

**Oozeer, N., Rudnick, L., Bietenholz, M. F.** *et al.* Discovery of Rare Dying Radio Galaxies Using MeerKAT. *Galaxies*, 9(4):102, November 2021. ISSN 2075-4434. doi:10.3390/galaxies9040102.

**Orlowski-Scherer, J., Haridas, S. K., Di Mascolo, L.** *et al.* GBT/MUSTANG-2 9″ resolution imaging of the SZ effect in MS0735.6+7421. Confirmation of the SZ cavities through direct imaging. *Astronomy & Astrophysics*, 667:L6, November 2022.

**Pandge, M. B., Monteiro-Oliveira, R., Bagchi, J.** *et al.* A combined X-ray, optical, and radio view of the merging galaxy cluster MACS J0417.5–1154. *Monthly Notices of the Royal Astronomical Society*, 482(4):5093–5105, October 2018. ISSN 0035-8711. doi:10.1093/mnras/sty2937.

**Pearce, C. J. J., van Weeren, R. J., Andrade-Santos, F.** *et al.* VLA Radio Observations of the HST Frontier Fields Cluster Abell 2744: The Discovery of New Radio Relics. *The Astrophysical Journal*, 845(1):81, August 2017. doi:10.3847/1538-4357/aa7e2f.

**Pelló, R., Rudnick, G., De Lucia, G.** *et al.* Photometric redshifts and cluster tomography in the ESO Distant Cluster Survey. *Astronomy & Astrophysics*, 508(3):1173–1191, October 2009. ISSN 1432-0746. doi:10.1051/0004-6361/200810644.

**Perley, R. A., Chandler, C. J., Butler, B. J.** *et al.* The Expanded Very Large Array: A New Telescope for New Science. *Astrophysical Journal, Letters*, 739(1):L1, September 2011. doi:10.1088/2041-8205/739/1/L1.

**Persic, M. and Salucci, P.** The baryon content of the Universe. *Monthly Notices of the Royal Astronomical Society*, 258(1):14P–18P, September 1992. ISSN 1365-2966. doi:10.1093/mnras/258.1.14p.

**Peterson, J. R., Kahn, S. M., Paerels, F. B. S.** *et al.* High Resolution X-ray Spectroscopic Constraints on Cooling-Flow Models. 2003.

**Pillay, D. S., Turner, D. J., Hilton, M.** *et al.* A Multiwavelength Dynamical State Analysis of ACT-CL J0019. 6+ 0336. *Galaxies*, 9(4):97, 2021. Publisher: MDPI.

**Pizzo, R. F., de Bruyn, A. G., Bernardi, G.** *et al.* Deep multi-frequency rotation measure tomography of the galaxy cluster A2255. *Astronomy & Astrophysics*, 525:A104, December 2010. ISSN 1432-0746. doi:10.1051/0004-6361/201014158.

**Poggianti, B. M., Moretti, A., and Gullieuszik, M.** GASP. I. Gas Stripping Phenomena in Galaxies with MUSE. *Astrophysical Journal*, 844(1):48, July 2017. doi: 10.3847/1538-4357/aa78ed.

**Postman, M., Coe, D., Benítez, N.** *et al.* The Cluster Lensing And Supernova Survey with Hubble: An overview. *The Astrophysical Journal Supplement Series*, 199(2):25, March 2012. ISSN 1538-4365. doi:10.1088/0067-0049/199/2/25.

**Rajpurohit, K., Brunetti, G., Bonafede, A.** *et al.* Physical insights from the spectrum of the radio halo in MACS J0717.5+3745. *Astronomy & Astrophysics*, 646:A135, February 2021. doi:10.1051/0004-6361/202039591.

**Rajpurohit, K., Hoeft, M., van Weeren, R. J.** *et al.* Deep VLA Observations of the Cluster 1RXS J0603.3+4214 in the Frequency Range of 1–2 GHz. *The Astrophysical Journal*, 852(2):65, January 2018. doi:10.3847/1538-4357/aa9f13.

**Rajpurohit, K., Hoeft, M., Vazza, F.** *et al.* New mysteries and challenges from the Toothbrush relic: wideband observations from 550 MHz to 8 GHz. *Astronomy & Astrophysics*, 636:A30, April 2020a. ISSN 1432-0746. doi:10.1051/0004-6361/201937139.

**Rajpurohit, K., Osinga, E., Brienza, M.** *et al.* Deep low-frequency radio observations of Abell 2256: II. The ultra-steep spectrum radio halo. *Astronomy & Astrophysics*, 669:A1, December 2022a. ISSN 1432-0746. doi:10.1051/0004-6361/202244925.

**Rajpurohit, K., van Weeren, R. J., Hoeft, M.** *et al.* Deep Low-frequency Radio Observations of A2256. I. The Filamentary Radio Relic. *The Astrophysical Journal*, 927(1):80, March 2022b. ISSN 1538-4357. doi:10.3847/1538-4357/ac4708.

**Rajpurohit, K., Vazza, F., van Weeren, R. J.** *et al.* Dissecting nonthermal emission in the complex multiple-merger galaxy cluster Abell 2744: Radio and X-ray analysis. *Astronomy & Astrophysics*, 654:A41, October 2021. ISSN 1432-0746. doi:10.1051/0004-6361/202141060.

**Rajpurohit, K., Wittor, D., Weeren, R.** *et al.* Understanding the radio relic emission in the galaxy cluster MACS J0717.5+3745: Spectral analysis. *Astronomy & Astrophysics*, 2020b. doi:10.1051/0004-6361/202039428.

**Reimer, O. and Sreekumar, P.** Clusters of galaxies in high-energy $\gamma$-ray astronomy. *New Astronomy Review*, 48(5-6):481–483, April 2004. doi:10.1016/j.newar.2003.12.024.

**Riseley, C. J., Bonnassieux, E., Vernstrom, T.** *et al.* Radio fossils, relics, and haloes in Abell 3266: cluster archaeology with ASKAP-EMU and the ATCA. *Monthly Notices of the Royal Astronomical Society*, 515(2):1871–1896, 08 2022. ISSN 0035-8711. doi:10.1093/mnras/stac1771.

**Roberts, I. D., Lang , M. Trotsenko, D., Bemis, A. R., Ellison, S. L., Lin, L., Pan, H.-A., Ignesti, A., Leslie, S., and van Weeren, R. J.** Lotss jellyfish galaxies. iv. enhanced star formation on the leading half of cluster galaxies and gas compression in ic3949. *The Astrophysical Journal*, 941(1):77, December 2022. ISSN 1538-4357. doi:10.3847/1538-4357/ac9e9f.
URL http://dx.doi.org/10.3847/1538-4357/ac9e9f

**Rott, N.** Jakob Ackeret and the History of the Mach Number. *Annual Review of Fluid Mechanics*, 17(Volume 17, 1985):1–10, 1985. ISSN 1545-4479. doi:https://doi.org/10.1146/annurev.fl.17.010185.000245.

**Rottgering, H. J. A., Wieringa, M. H., Hunstead, R. W.** *et al.* The extended radio emission in the luminous X-ray cluster A3667. *Monthly Notices of the Royal Astronomical Society*, 290(4):577–584, September 1997. doi:10.1093/mnras/290.4.577.

**Rudnick, L.** Simple Multiresolution Filtering and the Spectra of Radio Galaxies and Supernova Remnants. *Publications of the Astronomical Society of the Pacific*, 114(794):427–449, April 2002. doi:10.1086/342499.

**Ruhl, J., Ade, P. A. R., Carlstrom, J. E.** *et al.* The South Pole Telescope. In **Zmuidzinas, J., Holland, W. S., and Withington, S.**, editors, *Millimeter and Submillimeter Detectors for Astronomy II*, volume 5498, page 11. SPIE, October 2004. ISSN 0277-786X. doi:10.1117/12.552473.

**Rybicki, G. and Lightman, A.** Radiative Processes in Astrophysics. Physics textbook. John Wiley  Sons, 1991, 1991. ISBN 9780471048152.

**Santra, R., Kale, R., Giacintucci** *et al.* A Deep uGMRT View of the Ultra-steep Spectrum Radio Halo in A521. *Astrophysical Journal*, 962(1):40, February 2024. doi: 10.3847/1538-4357/ad1190.

**Sarazin, C. L.** X-ray emission from clusters of galaxies. *Rev. Mod. Phys.*, 58:1–115, January 1986. doi:10.1103/RevModPhys.58.1.

**Sarazin, C. L.** The Physics of Cluster Mergers. In *Merging Processes in Galaxy Clusters*, pages 1–38. Springer Netherlands, 2002. doi:10.1007/0-306-48096-4_1.

**Sault, R. J. and Cornwell, T. J.** The Hamaker-Bregman-Sault Measurement Equation. In **Taylor, G. B., Carilli, C. L., and Perley, R. A.**, editors, *Synthesis Imaging in Radio Astronomy II*, volume 180 of *Astronomical Society of the Pacific Conference Series*, page 657. January 1999.

**Schwab, F. R.** Relaxing the isoplanatism assumption in self-calibration; applications to low-frequency radio interferometry. *The Astronomical Journal*, 89:1076–1081, July 1984. doi:10.1086/113605.

**Shimwell, T. W., Luckin, J., Brüggen, M.** *et al.* A plethora of diffuse steep spectrum radio sources in Abell 2034 revealed by LOFAR. *Monthly Notices of the Royal Astronomical Society*, 459(1):277–290, March 2016. ISSN 1365-2966. doi: 10.1093/mnras/stw661.

**Shimwell, T. W., Markevitch, M., Brown, S.** *et al.* Another shock for the Bullet cluster, and the source of seed electrons for radio relics. *Monthly Notices of the Royal Astronomical Society*, 449(2):1486–1494, May 2015. doi:10.1093/mnras/stv334.

**Sikhosana, S.** Giant radio halos and relics in ACTPol clusters. Master's thesis, University of KwaZulu-Natal, 2017.

**Sikhosana, S. P., Knowles, K., Hilton, M.** *et al.* MeerKAT's view of the bullet cluster 1E 0657-55.8. *Monthly Notices of the Royal Astronomical Society*, 518(3):4595–4605, November 2022. ISSN 1365-2966. doi:10.1093/mnras/stac3370.

**Sikhosana, S. P., Knowles, K., Ishwara-Chandra, C.** *et al.* A GMRT Narrowband vs. Wideband Analysis of the ACT- CL J0034. 4+ 0225 Field Selected from the ACTPol Cluster Sample. *Galaxies*, 9(4):117, 2021. Publisher: MDPI.

**Skillman, S. W., Xu, H., Hallman, E. J.** *et al.* Cosmological Magnetohydrodynamic Simulkations of Galaxy Cluster Radio Relics: Insights and Warnings for Observations. *The Astrophysical Journal*, 765(1):21, February 2013. ISSN 1538-4357. doi:10.1088/0004-637x/765/1/21.

**Skrutskie, M. F., Cutri, R. M., Stiening, R.** *et al.* The Two Micron All Sky Survey (2MASS). *Astronomical Journal*, 131(2):1163–1183, February 2006. doi:10.1086/498708.

**Smirnov, O. M.** Revisiting the radio interferometer measurement equation. I. A full-sky Jones formalism. *Astronomy Astrophysics*, 527:A106, March 2011a. ISSN 0004-6361, 1432-0746. doi:10.1051/0004-6361/201016082. ArXiv:1101.1764 [astro-ph].

**Smirnov, O. M.** Revisiting the radio interferometer measurement equation: II. Calibra-

tion and direction-dependent effects. *Astronomy &; Astrophysics*, 527:A107, February 2011b. ISSN 1432-0746. doi:10.1051/0004-6361/201116434.

**Smith, R. J.** X-ray emission properties of galaxies in Abell 3128. *Monthly Notices of the Royal Astronomical Society*, 344(2):L17–L21, 09 2003. ISSN 0035-8711. doi: 10.1046/j.1365-8711.2003.06963.x.

**Smithsonian Astrophysical Observatory**. SAOImage DS9: A utility for displaying astronomical images in the X11 window environment. *Astrophysics Source Code Library*, record ascl:0003.002, March 2000.

**Smolčić, V., Novak, M., Bondi, M.** *et al.* The VLA-COSMOS 3 GHz Large Project: Continuum data and source catalog release. *Astronomy & Astrophysics*, 602:A1, June 2017. doi:10.1051/0004-6361/201628704.

**Stuardi, C., Bonafede, A., Wittor, D., Vazza, F., Botteon, A., and Locatelli, N.** Particle re-acceleration and faraday-complex structures in the rxc j1314.4-2515 galaxy cluster. *Monthly Notices of the Royal Astronomical Society*, August 2019. ISSN 1365-2966. doi:10.1093/mnras/stz2408.
URL http://dx.doi.org/10.1093/mnras/stz2408

**Sunyaev, R., Arefiev, V., Babyshkin, V.** *et al.* SRG X-ray orbital observatory. Its telescopes and first scientific results. *Astronomy & Astrophysics*, 656:A132, December 2021. doi:10.1051/0004-6361/202141179.

**Sunyaev, R. A. and Zeldovich, Y. B.** The Observations of Relic Radiation as a Test of the Nature of X-Ray Radiation from the Clusters of Galaxies. *Comments on Astrophysics and Space Physics*, 4:173, November 1972.

**Swarup, G.** Giant metrewave radio telescope (GMRT) - Scientific objectives and design aspects. *Indian Journal of Radio and Space Physics*, 19:493–505, December 1990.

**Swetz, D. S., Ade, P. A. R., Amiri, M.** *et al.* Overview of the Atacama Cosmology Telescope: Receiver, Instrumentation, and Telescope Systems. *Astrophysical Journal, Supplement*, 194(2):41, June 2011. doi:10.1088/0067-0049/194/2/41.

**T. Cornwell, D. B., R. Braun**. "Deconvolution". In *Synthesis Imaging in Radio Astronomy II*, volume 180 of *Astronomical Society of the Pacific Conference Series*, pages 127–148. January 1999.

**Tasse, C.** killMS: Direction-dependent radio interferometric calibration package. *Astrophysics Source Code Library*, record ascl:2305.005, May 2023.

**Tasse, C., Hugo, B., Mirmont, M.** *et al.* DDFacet: Facet-based radio imaging package. *Astrophysics Source Code Library*, record ascl:2305.008, May 2023.

**Taylor, M.** TOPCAT: Tool for OPerations on Catalogues And Tables. *Astrophysics Source Code Library*, record ascl:1101.010, January 2011.

**Thompson, A., Moran, J., and Swenson, G.** Interferometry and Synthesis in Radio Astronomy. Astronomy and Astrophysics Library. Springer International Publishing, 2017. ISBN 9783319444314.
URL https://books.google.co.za/books?id=tNlCDwAAQBAJ

**Thompson, A. R., Clark, B. G., Wade, C. M.** *et al.* The Very Large Array. *Astrophysical Journal, Supplement*, 44:151–167, October 1980. doi:10.1086/190688.

**T.J. Cornwell, E. F.** "Self-Calibration". In *Synthesis Imaging in Radio Astronomy II*, volume 180 of *Astronomical Society of the Pacific Conference Series*, pages 187–199. January 1999.

**Torsten A. Enßlin and Peter L. Biermann and Ulrich Klein and others**. Cluster radio relics as a tracer of shock waves of the large-scale structure formation. *Astronomy & Astrophysics*, 332:395–409, April 1998. doi:10.48550/arXiv.astro-ph/9712293.

**Trehaeven, K.** M3: Mining Mini-Halos with MeerKAT. Master's thesis, Rhodes University, 2022.

**Trehaeven, K. S., Parekh, V., Oozeer, N.** *et al.* Mining mini-halos with MeerKAT I. Calibration and imaging. *Monthly Notices of the Royal Astronomical Society*, 520(3):4410–4426, February 2023. ISSN 1365-2966. doi:10.1093/mnras/stad391.

**Turner, M. S.** The Road to Precision Cosmology. *Annual Review of Nuclear and Particle Science*, 72(Volume 72, 2022):1–35, 2022. ISSN 1545-4134. doi:https://doi.org/10.1146/annurev-nucl-111119-041046.

**UC Berkeley**. October 2012. [Accessed 17-01-2025].
URL https://casper.astro.berkeley.edu/astrobaki/index.php/Radiometer_Equation_Applied_to_Telescopes

**van Weeren, R., de Gasperin, F., Akamatsu, H.** *et al.* Diffuse radio emission from galaxy clusters. *Space Science Reviews*, 215:1–75, 2019. Publisher: Springer.

**van Weeren, R., Hoeft, M., Röttgering, H.** *et al.* A double radio relic in the merging galaxy cluster ZwCl 0008.8+ 5215. *Astronomy & Astrophysics*, 528:A38, 2011.

**van Weeren, R. J., Intema, H. T., Oonk, J. B. R.** *et al.* The discovery of diffuse steep spectrum sources in Abell 2256. *Astronomy & Astrophysics*, 508(3):1269–1273, December 2009. doi:10.1051/0004-6361/200912934.

**van Weeren, R. J., Ogrean, G. A., Jones, C.** *et al.* Chandra and JVLA Observations of HST Frontier Fields Cluster MACS J0717.5+3745. *Astrophysics Journal*, 835(2):197, February 2017. doi:10.3847/1538-4357/835/2/197.

**van Weeren, R. J., Röttgering, H. J. A., Brüggen, M.** *et al.* Particle Acceleration on Megaparsec Scales in a Merging Galaxy Cluster. *Science*, 330(6002):347, October 2010. doi:10.1126/science.1194293.

**Vazza, F., Brüggen, M., van Weeren, R.** *et al.* Why are central radio relics so rare? *Monthly Notices of the Royal Astronomical Society*, 421(3):1868–1873, 04 2012. doi:10.1111/j.1365-2966.2011.20160.x.

**Vazza, F., Wittor, D., Brüggen, M.** *et al.* Simulating the Enrichment of Fossil Radio Electrons by Multiple Radio Galaxies. *Galaxies*, 11(2), 2023. ISSN 2075-4434. doi:10.3390/galaxies11020045.

**Venturi, T., Giacintucci, S., Brunetti, G.** *et al.* GMRT radio halo survey in galaxy clusters at z = 0.2-0.4. I. The REFLEX sub-sample. *Astronomy & Astrophysics*, 463(3):937–947, March 2007. doi:10.1051/0004-6361:20065961.

**Venturi, T., Giacintucci, S., Merluzzi, P., Bardelli, S., Busarello, G., Dallacasa, D., and Sikhosana, S. P.** Radio footprints of a minor merger in the Shapley Supercluster: From supercluster down to galactic scales. *Astronomy & Astrophysics*, 660:A81, April 2022. doi:10.1051/0004-6361/202142048.

**Wen, Z. L. and Han, J. L.** Substructure and dynamical state of 2092 rich clusters of galaxies derived from photometric data. *Monthly Notices of the Royal Astronomical Society*, 436(1):275–293, 09 2013. ISSN 0035-8711. doi:10.1093/mnras/stt1581.

**Wenger, M., Ochsenbein, F., Egret, D.** *et al.* The SIMBAD astronomical database: The CDS reference database for astronomical objects. *Astronomy & Astrophysics Supplement Series*, 143(1):9–22, April 2000. ISSN 1286-4846. doi:10.1051/aas:2000332.

**Werner, N., Churazov, E., Finoguenov, A.** *et al.* Complex X-ray morphology of Abell 3128: A distant cluster behind a disturbed cluster. *Astronomy Astrophysics*, 474(3):707–716, November 2007. ISSN 0004-6361, 1432-0746. doi:10.1051/0004-6361:20077990. ArXiv:0708.3253 [astro-ph].

**Wiedemann, H.** Synchrotron radiation. Springer, 2003, 647–686 pages.

**Wilber, A., Brüggen, M., Bonafede, A.** *et al.* LOFAR discovery of an ultra-steep radio halo and giant head-tail radio galaxy in Abell 1132. *Monthly Notices of the Royal Astronomical Society*, 473(3):3536–3546, January 2018. doi:10.1093/mnras/stx2568.

**Wilber, A., Brüggen, M., Bonafede, A.** *et al.* Search for low-frequency diffuse radio emission around a shock in the massive galaxy cluster MACS J0744.9+3927. *Monthly Notices of the Royal Astronomical Society*, 476(3):3415–3424, 02 2018. ISSN 0035-8711. doi:10.1093/mnras/sty414.

**Wrobel, J. M. and Walker, R. C.** Sensitivity. In *Synthesis Imaging in Radio Astron-*

*omy II*, volume 180 of *Astronomical Society of the Pacific Conference Series*, page 171. January 1999.

**Xie, C., van Weeren, R. J., Lovisari, L.** *et al.* The discovery of radio halos in the frontier fields clusters Abell S1063 and Abell 370. *Astronomy & Astrophysics*, 636:A3, April 2020. ISSN 1432-0746. doi:10.1051/0004-6361/201936953.

**Yuan, Z. S. and Han, J. L.** Dynamical state for 964 galaxy clusters from chandra x-ray images. *Monthly Notices of the Royal Astronomical Society*, 497(4):5485–5497, 08 2020.

**Yuan, Z. S., Han, J. L., and Wen, Z. L.** Dynamical state of galaxy clusters evaluated from X-ray images. *Monthly Notices of the Royal Astronomical Society*, 513(2):3013–3021, June 2022. doi:10.1093/mnras/stac1037.

**Zandanel, F., Pfrommer, C., and Prada, F.** On the physics of radio haloes in galaxy clusters: scaling relations and luminosity functions. *Monthly Notices of the Royal Astronomical Society*, 438(1):124–144, December 2013. ISSN 1365-2966. doi:10.1093/mnras/stt2250.

**ZuHone, J. A., Brunetti, G., Giacintucci, S., and Markevitch, M.** Testing secondary models for the origin of radio mini-halos in galaxy clusters. *The Astrophysical Journal*, 801(2):146, mar 2015. doi:10.1088/0004-637X/801/2/146.
URL https://dx.doi.org/10.1088/0004-637X/801/2/146

**ZuHone, J. A., Markevitch, M., Brunetti, G.** *et al.* Turbulence and radio mini-halos in the sloshing cores of galaxy clusters. *The Astrophysical Journal*, 762(2):78, December 2012. doi:10.1088/0004-637X/762/2/78.

# Appendix A

# Full-resolution images

We present the full-resolution primary beam corrected JVLA and MeerKAT images for each field. In each image, the cluster is circled in white and scale bar indicated in black.

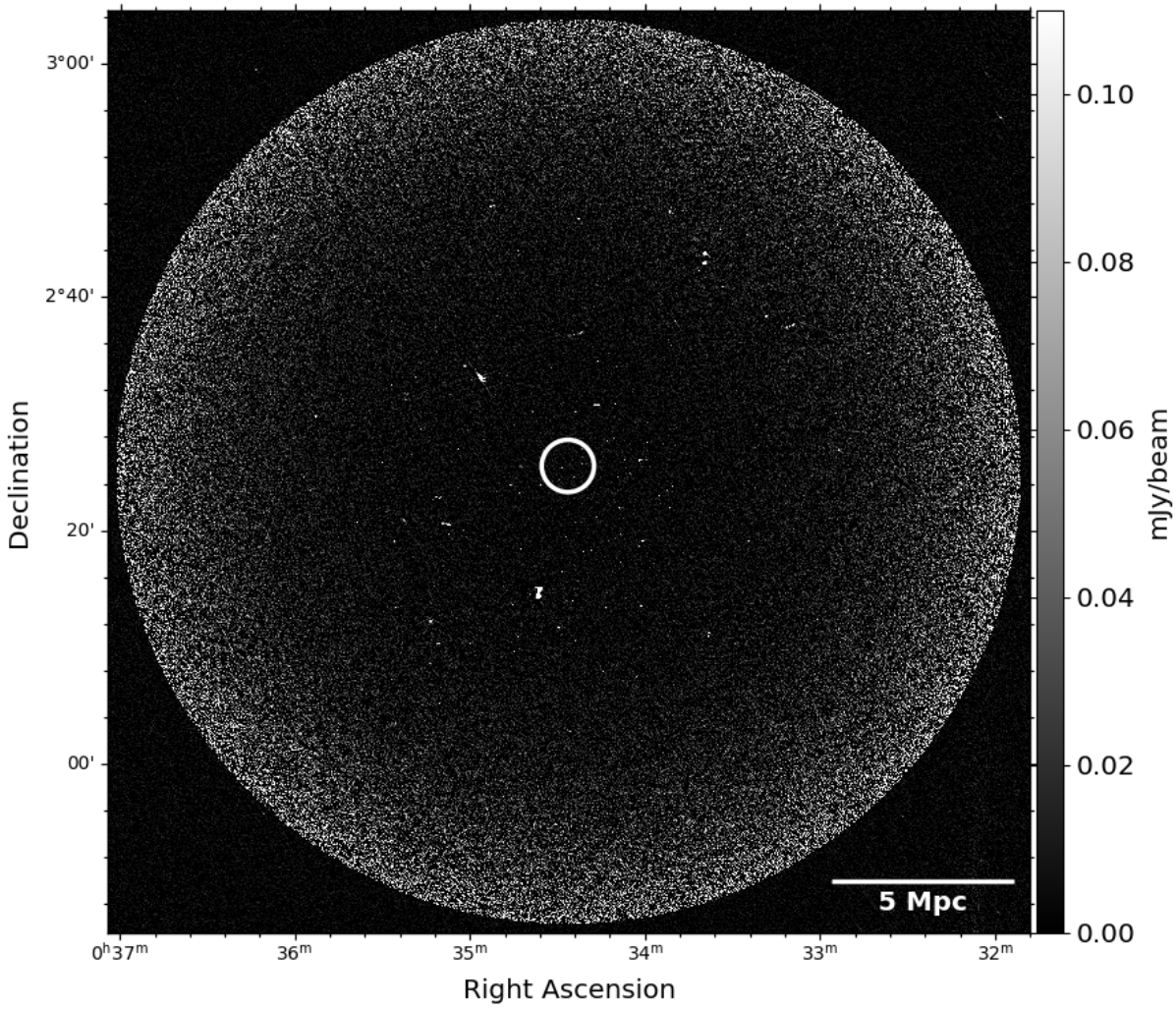


**Figure A.1:** Full-resolution JVLA image for ACT-CL J0034+0225 which resides at a redshift of $z = 0.388$. The central noise in the image is 10.3 μJy/beam for a beamsize of $3.8'' \times 2.8''$ with a PA of $-69.7$ deg.

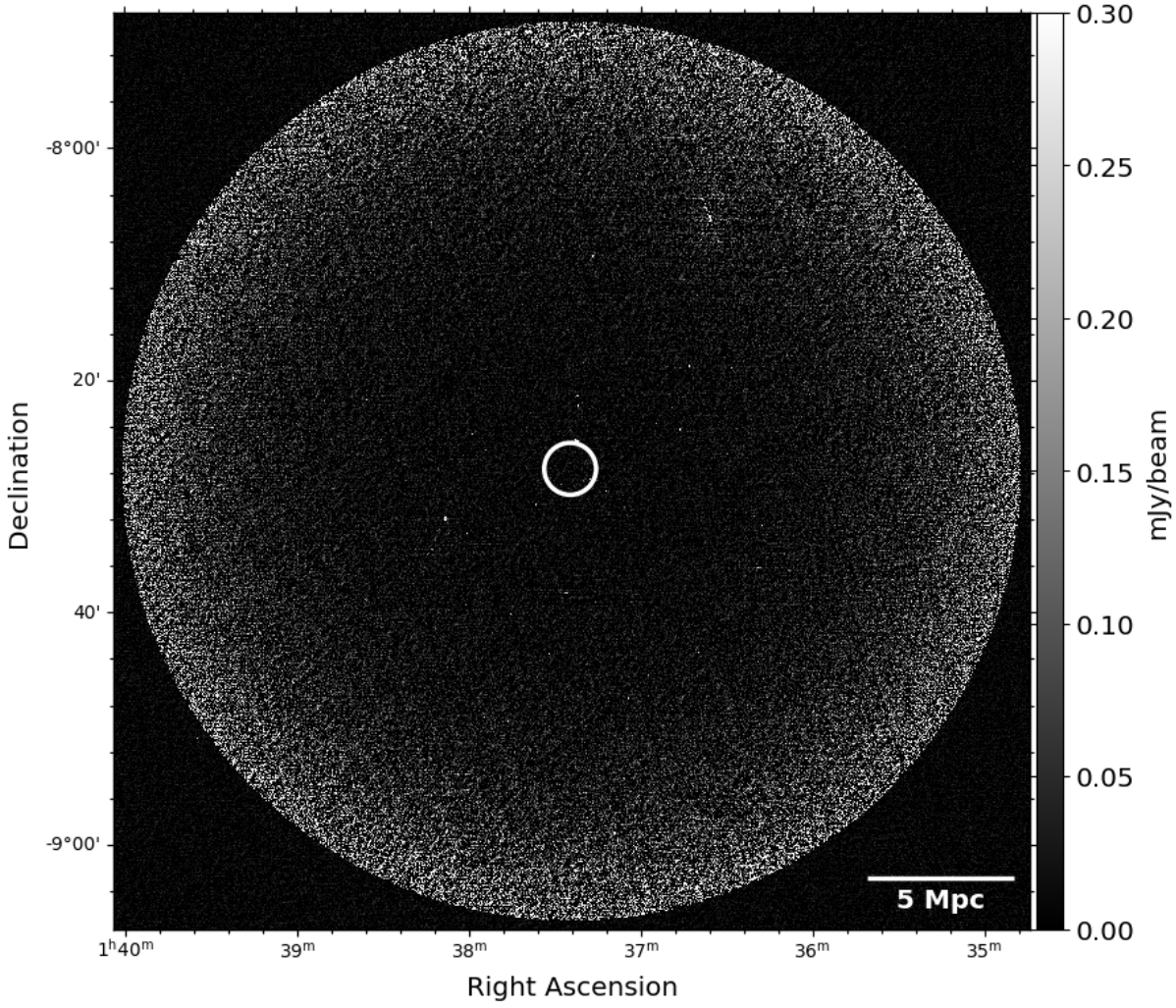


**Figure A.2:** Full-resolution JVLA image for ACT-CL J0137-0827 at a redshift of $z = 0.569$. The central noise in the image is 29.9 μJy/beam for a beamsize of $3.8'' \times 2.9''$ with a PA of $-13.9$ deg.

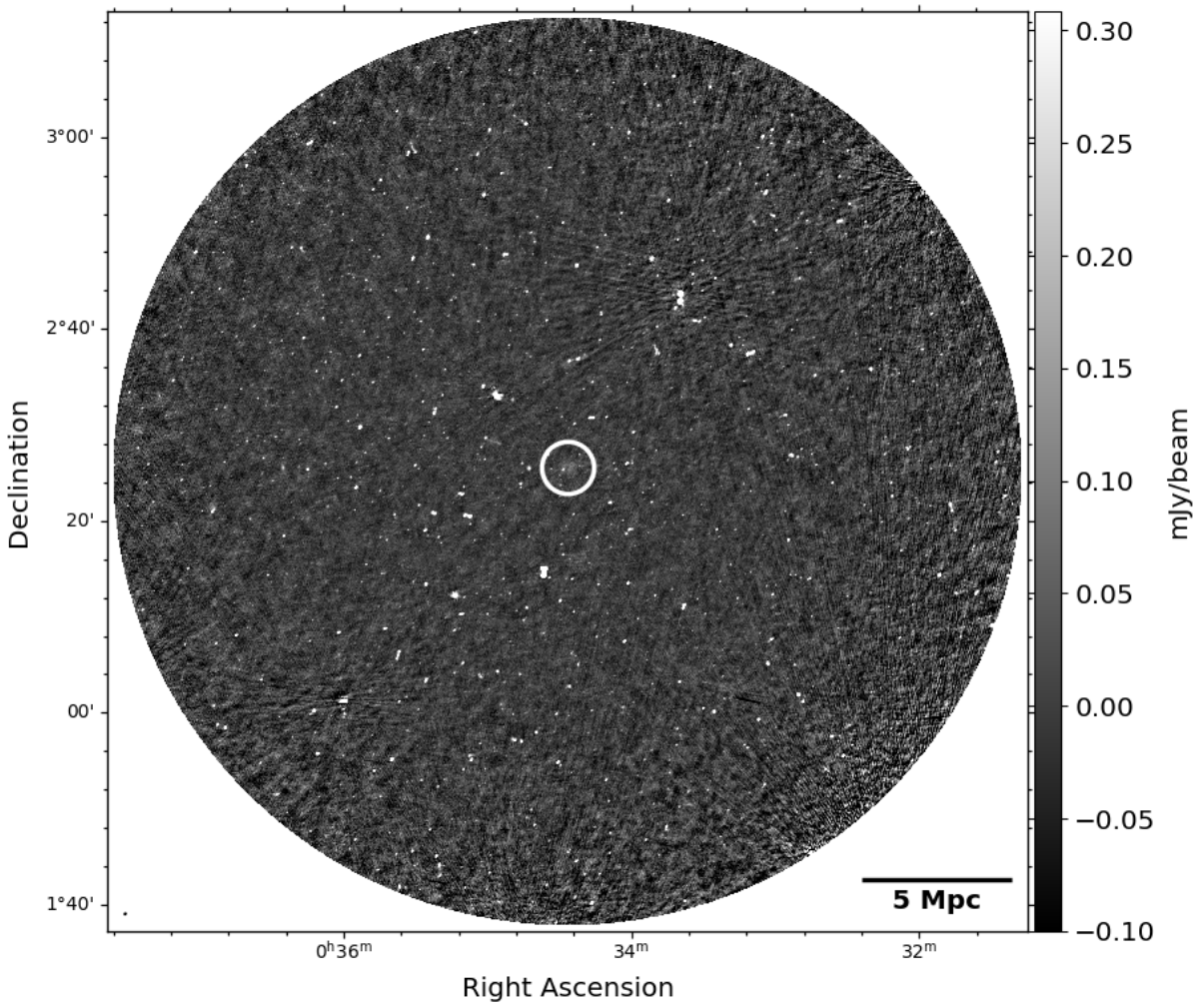


**Figure A.3:** Full-resolution MeerKAT image for ACT-CL J0034+0225. The central noise in the image is 24.4 μJy/beam for a beamsize of $10.4'' \times 7.6''$ with a PA of $-44.9$ deg.

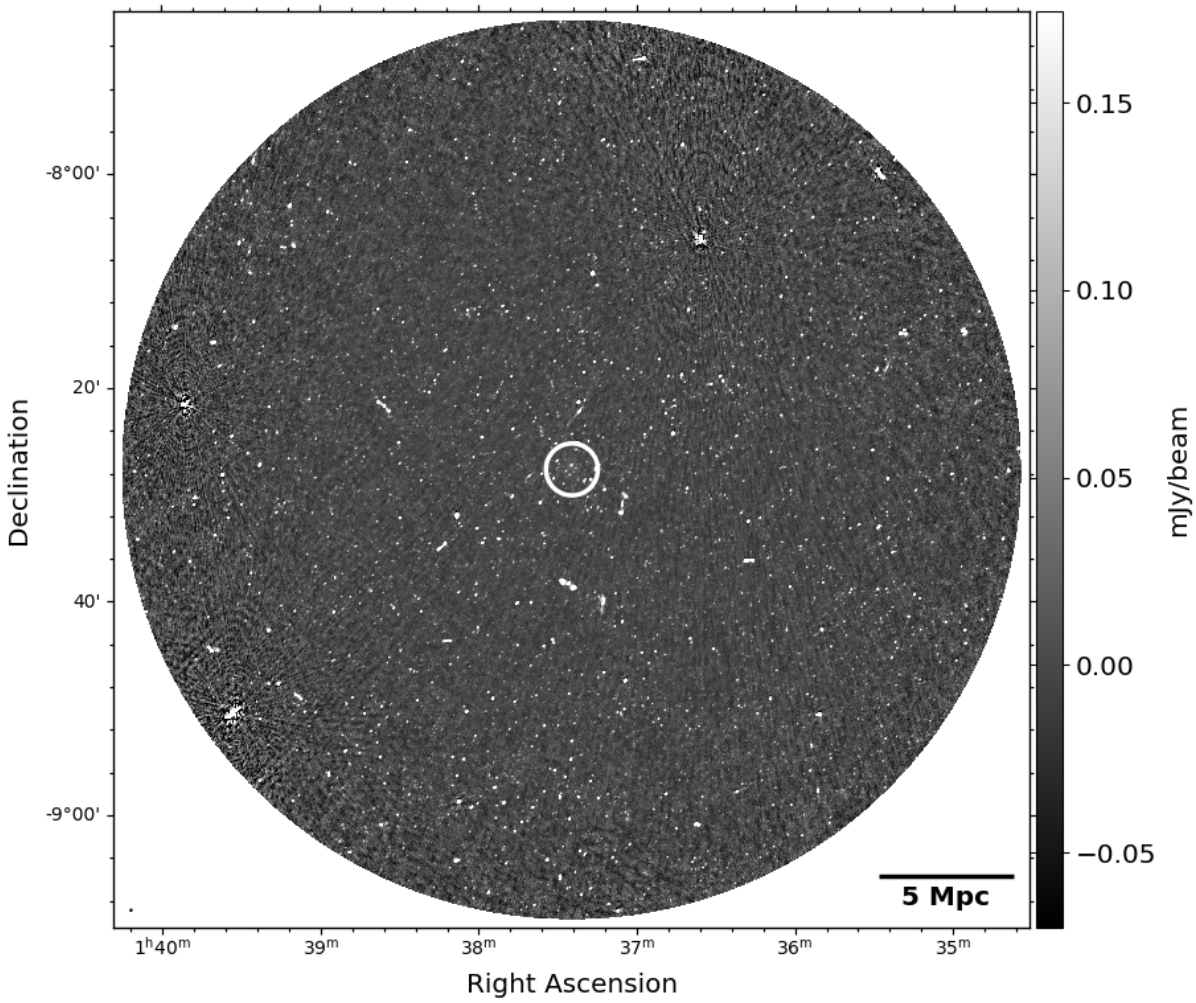


**Figure A.4:** Full-resolution MeerKAT image for ACT-CL J0137-0827. The central noise in the image is 7.9 μJy/beam for a beamsize of $9.4'' \times 7.5''$ with a PA of $-37.8$ deg.

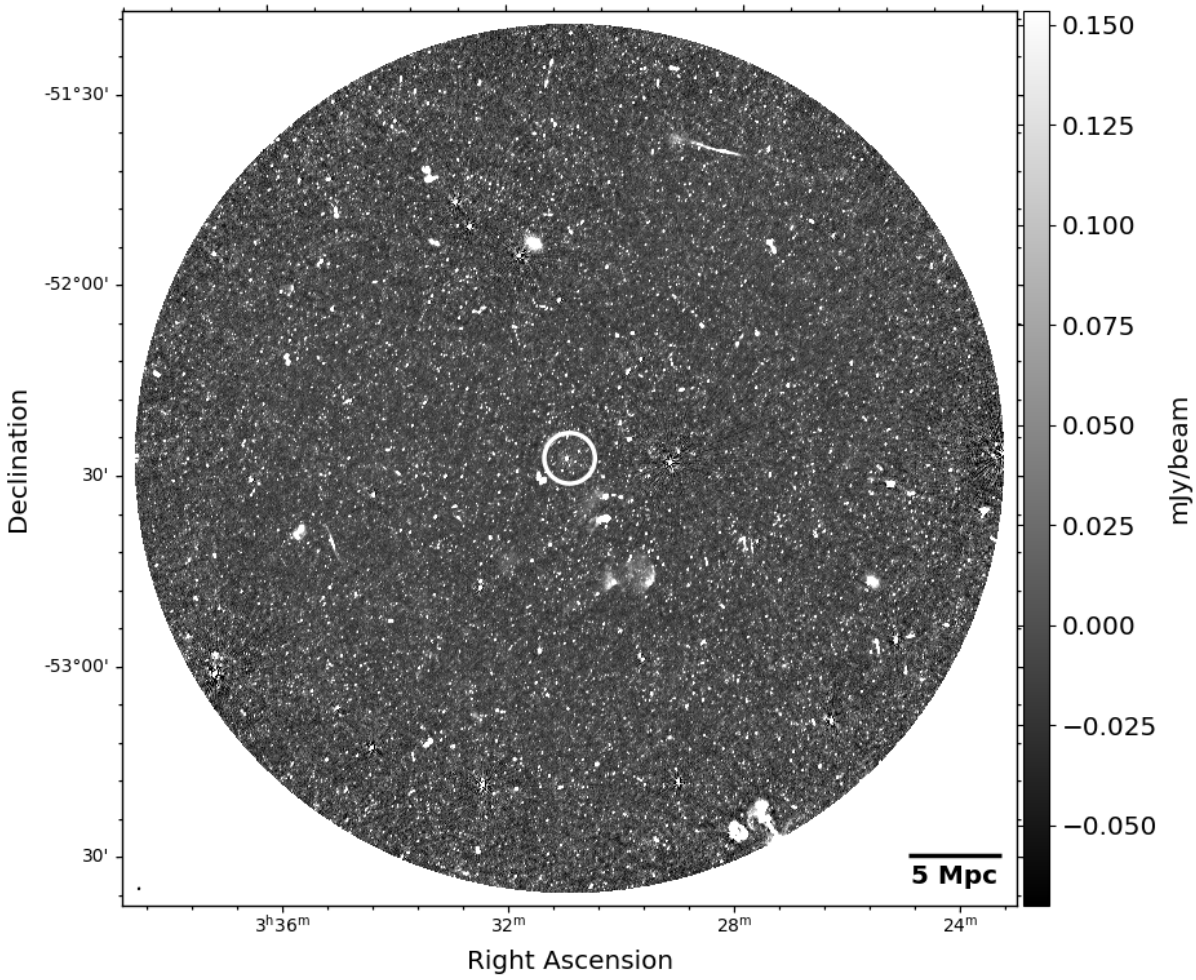


**Figure A.5:** Full-resolution UHF-band MeerKAT image for ACT-CL J0330-5228 at a redshift of $z = 0.442$. The central noise in the image is 14.3 μJy/beam for a beamsize of $14.5'' \times 10.2''$ with a PA of $-19.4$ deg.

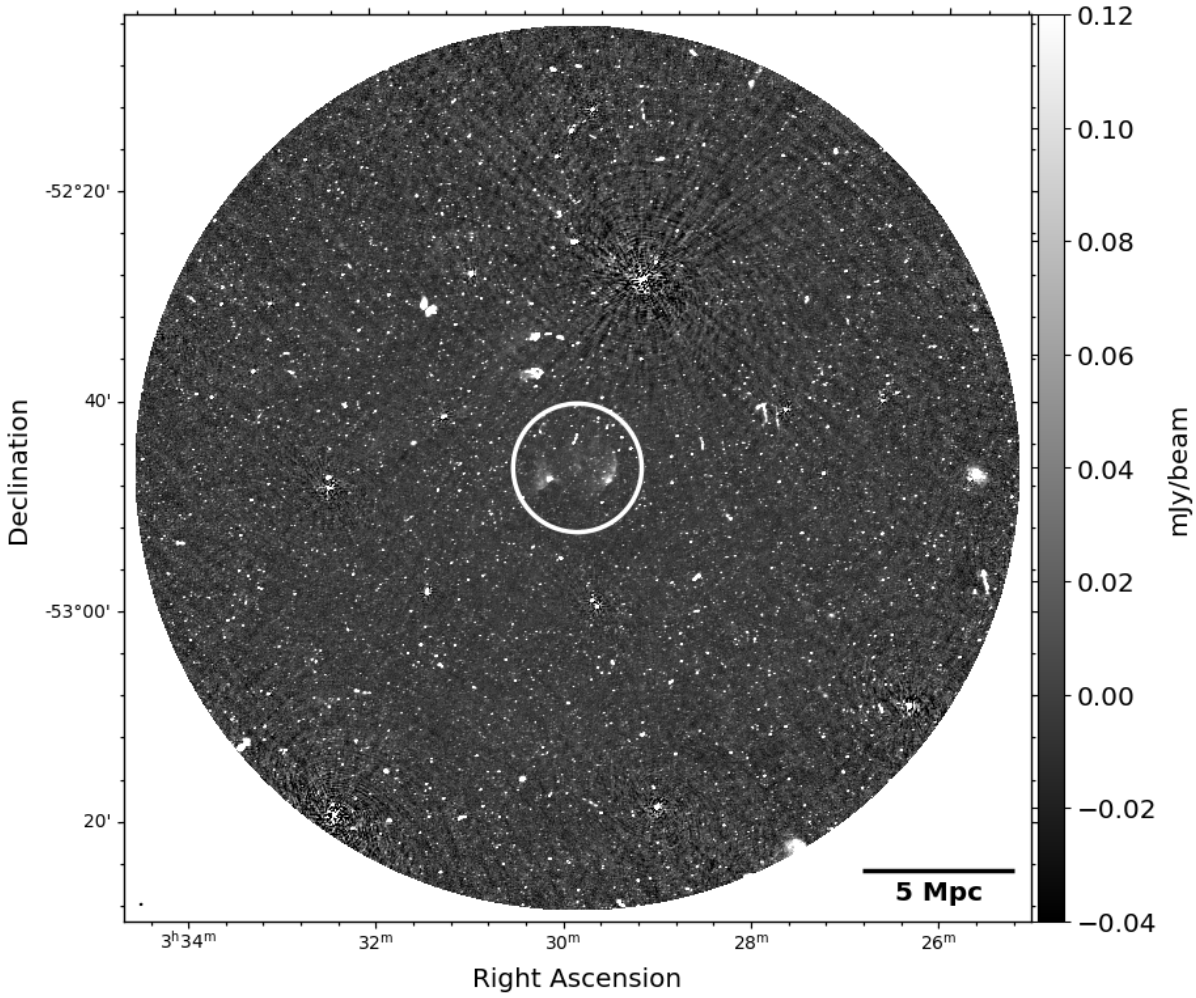


**Figure A.6:** Full-resolution L-band MeerKAT image for ACT-CL J0330-5228. The central noise in the image is 5.78 μJy/beam where the beam is $9.2'' \times 6.9''$ with a PA of $-74.7$ deg.

# Appendix B

# Flux checks

The following plots were generated for the flux density checks against the RACS low survey. We make use of the published RACS images to implement a stricter flux density cut than the published RACS catalogue. We use the same source finding algorithm as Hale *et al.* (2021) but with stricter island and pixel thresholds (5 and 8$\sigma$ respectively) to ensure that only bright sources were used for the test.

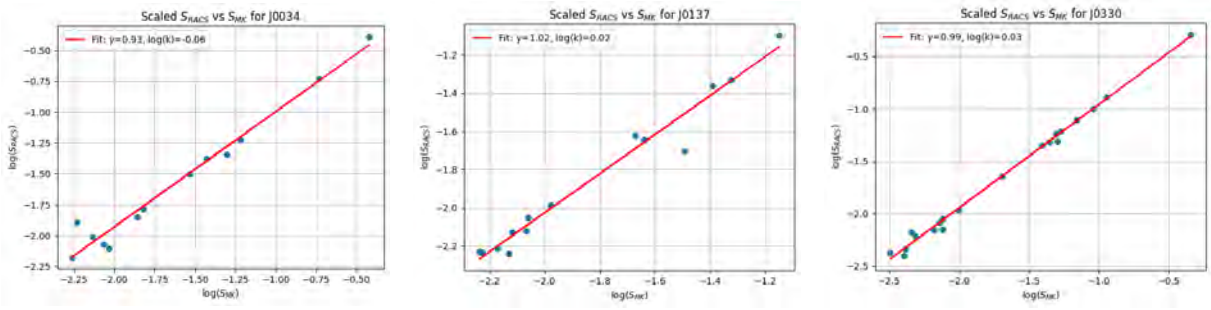


**Figure B.1:** Flux density check against RACS low images for MeerKAT images.

| Field | Images | $\kappa$ | $\Delta\kappa$ | $\gamma$ | $\Delta\gamma$ |
|---|---|---|---|---|---|
| J0034 | MK vs RACS low | 0.85 | 0.17 | 0.93 | 0.05 |
| | JVLA vs RACS low | 0.87 | 0.526 | 0.77 | 0.13 |
| J0137 | MK vs RACS low | 1.05 | 0.24 | 1.02 | 0.05 |
| | JVLA vs RACS low | 0.37 | 0.53 | 0.66 | 0.16 |
| J0330 | MK vs RACS low | 1.07 | 0.07 | 0.98 | 0.02 |
| | MK vs RACS mid | 0.69 | 0.27 | 0.86 | 0.07 |

**Table B.1:** Fit parameters from the flux density checks against RACS low.

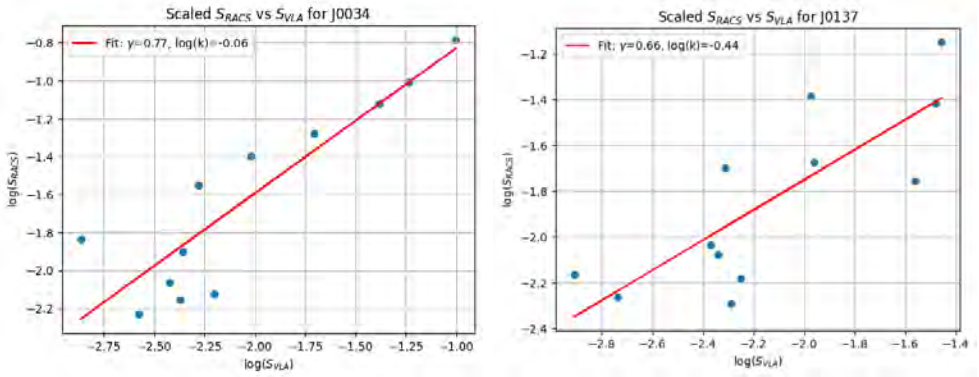


**Figure B.2:** Flux density check against RACS low images for JVLA images.

The deviations in flux density in the MeerKAT images are relatively small, however, we observe a greater degree of scatter when comparing the JVLA images with the RACS low image. We follow the same procedure as with the MeerKAT images. The severe artifacts present in the J0034 and J0137 JVLA images affect multiple sources across the fields, resulting in high uncertainties in $\kappa$. The points that deviate from the regression line correspond to measurements taken from sources either near the bright, problematic sources or those located along the artifact streaks. The scatter observed is likely influenced by a combination of factors, including the presence of residual RFI in the RACS low image.

# Appendix C

# Redshift Density Maps

The following maps were generated using zCluster and DECaLS DR8 and DR9 photometry. The density map is presented on the left and associated error map on the right of each figure.

To determine the redshift of the emission in the J0330 field, we generate multiple redshift density maps at redshift 'slices'. The central redshifts of the maps are chosen as 0.08, 0.2, 0.4, 0.6, 0.8, 1.0, 1.2, 1.4. We set the integration bounds of $dz = 0.02$ for the $z = 0.08$ map and $dz = 0.1$ for the remaining maps. The full-resolution UHF-band contours at 3, 5, 10 and 25$\sigma$ are overlaid to mark the position of sources and the diffuse structures.

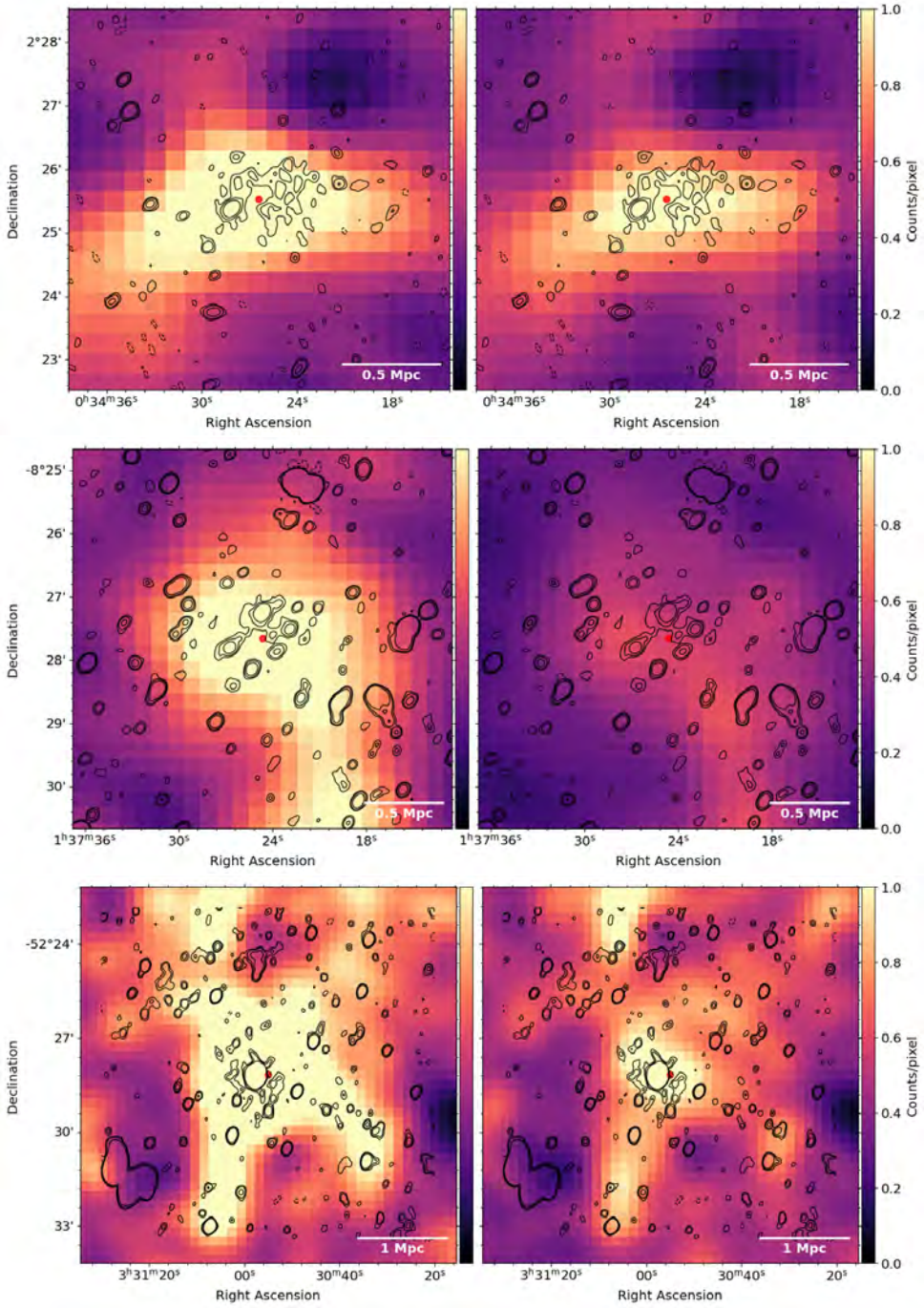


**Figure C.1:** Optical density maps (*left*) and error maps (*right*) for all three clusters with 3, 5, and 10$\sigma$ radio contours (black; where $\sigma$ is the RMS noise in each 2GC image). The SZ peak (red) is overlaid on each map.

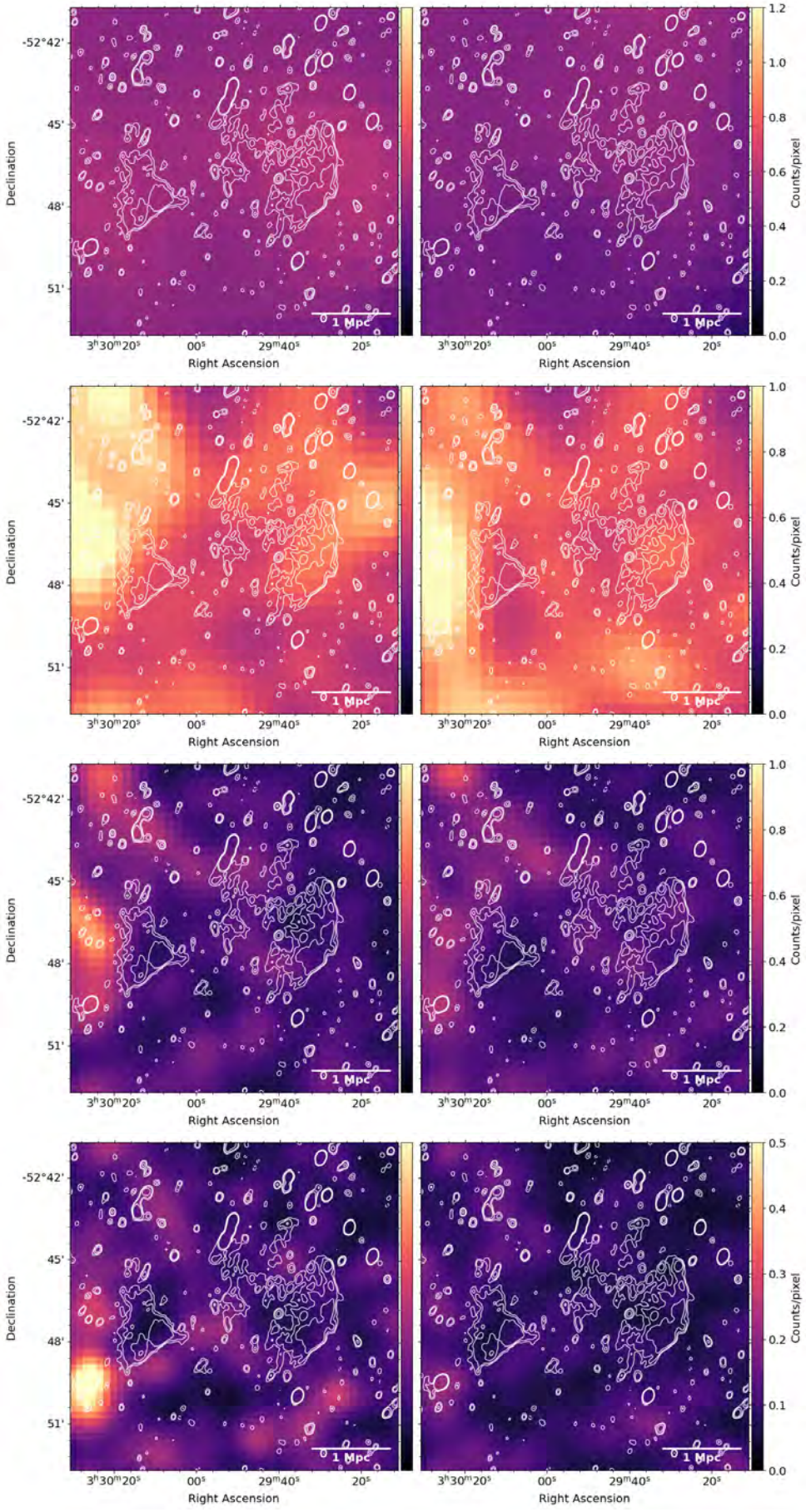


**Figure C.2:** Redshift slices at a central redshift of $z = 0.08,\ 0.2,\ 0.4,\ 0.6$.

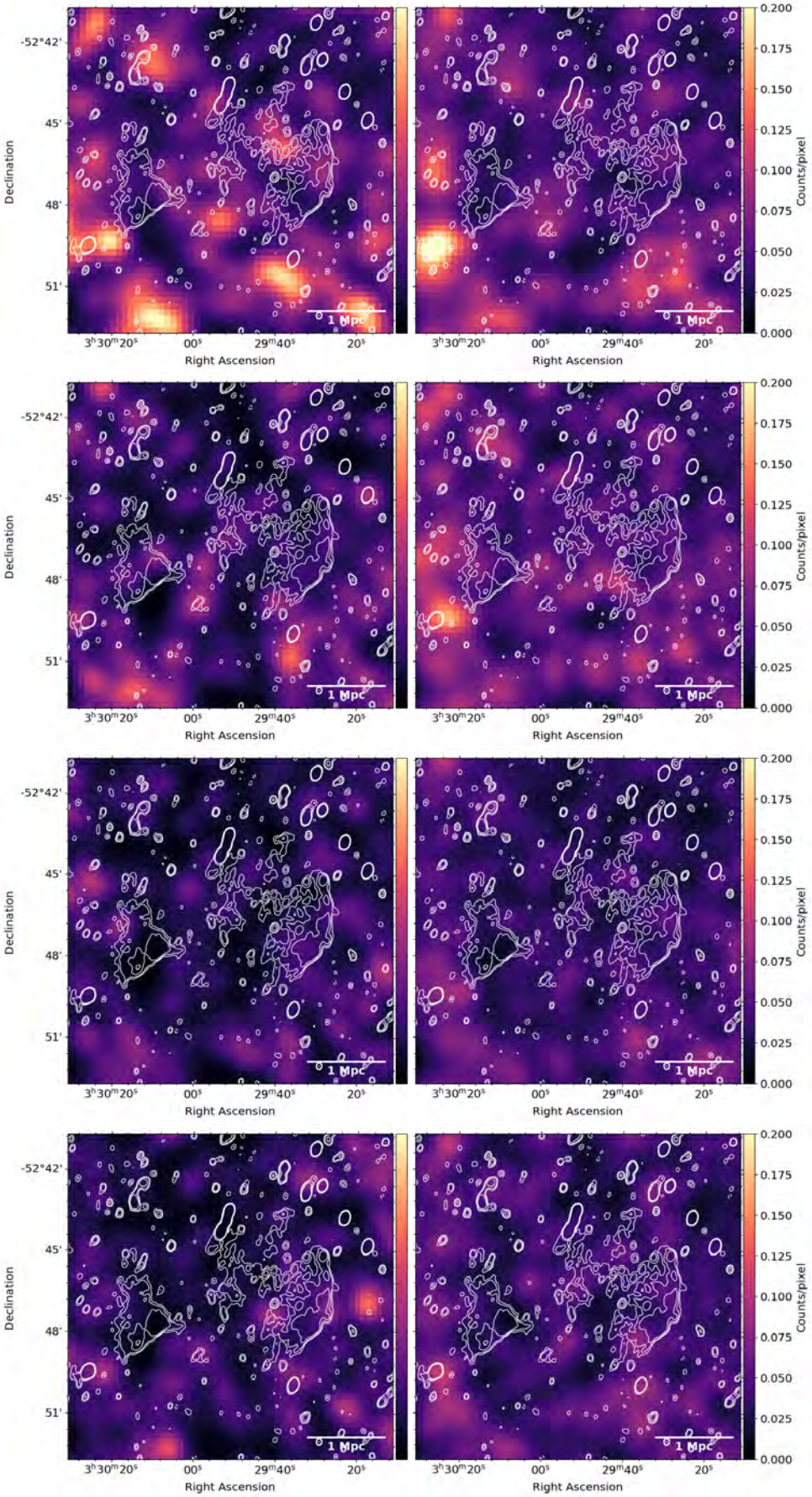


**Figure C.3:** Redshift slices at a central redshift of $z = 0.8,\ 1.0,\ 1.2,\ 1.4$.